



Hierarchical Silk Fibroin/Poly(L-lactic acid) Porous Fibrous Membrane and its Applications

A thesis submitted to The University of Manchester for the degree of
Doctor of Philosophy
in the Faculty of Science and Engineering

2021

Jun Song

Department of Materials, School of Natural Sciences

List of contents

Abstract.....	1
Declaration.....	2
Copyright Notice.....	3
Acknowledgement	4
Abbreviations.....	5
Chapter 1: Thesis Introduction & Research Objectives	6
1.1 Research Motivation	6
1.2 Research Gaps.....	8
1.3 Research Objectives.....	9
1.3.1 Objective 1: Confirm fabrication method for hierarchical PLLA fibrous membrane	9
1.3.2 Objective 2: Apply hierarchical porous PLLA fibrous membrane as a ultrafine particulate aerosol filter.....	9
1.3.3 Objective 3: Modify PLLA fibrous membrane by SF as a tubular scaffolds for muscular artery regeneration.....	9
1.4 Project Significance & Originality	9
Chapter 2: Background Theory & Literature Review	11
2.1 Electrospinning: A Facile Nano/Micro Fibre Producing Technique	11
2.1.1 Current development of electrospinning porous fibres	11
2.1.2 Hierarchical porous electrospinning fibrous membrane: fabrication strategies	12
2.2 Poly(L-lactic acid) (PLLA)	22
2.2.1 Materials properties.....	22
2.2.2 Spinning towards fibres and electrospinning	24
2.2.3 Properties of PLLA	25
2.2.4 Applications of PLLA	26
2.3 Silk Fibroin (SF)	27
2.3.1 Material background	27
2.3.2 Processing and modification	30
2.3.3 Properties of silk fibroin molecular.....	34

2.3.4 Applications of silk fibroin.....	37
2.4 Theory and Mechanism Development of Electrospun Porous Fibres	38
2.4.1 Hildebrand and Hansen solubility parameters.....	38
2.4.2 Flory-Huggins theory	41
2.4.3 Breath figure mechanism	43
2.4.4 Phase separation mechanism.....	45
2.4.5 Solvent induced crystallization	47
2.5 Applications of Electrospun Porous Fibres	49
2.5.1 Environmental protection and sustainable development goals.....	49
2.5.2 From electrospun fibre-based biomaterials to wearable sensors	52
Chapter 3: Materials & Experimental Methods	53
3.1 Materials	53
3.2 Experimental instruments and methods	53
3.2.1 Preparation of PLLA/DCM/DMF spinning solution.....	53
3.2.2 Electrospinning method and post treatment	54
3.2.3 Preparation of silk fibroin aqueous solution.....	55
3.3 Characterizations.....	56
3.3.1 Thickness of fibrous membrane	56
3.3.2 Surface morphology	56
3.3.3 Thermophysical Properties.....	56
3.3.4 Mechanical performance	56
3.3.5 XRD	57
Chapter 4: Hierarchical Porous PLLA Fibrous Membrane for Aerosol Filtration	58
4.1 Chapter Synopsis.....	59
4.2 Literature Review: Fibrous Membrane Filter for Ultrafine Aerosol Particles.....	60
4.3 Materials and Methods.....	62
4.3.1 Materials.....	62
4.3.2 Preparation of PLLA solution, electrospinning and post-treatment	62
4.3.3 Characterizations.....	65
4.3.4 Air filtration and pressure drop tests	66
5.3.5 Statistics	68
4.4 Results and Discussions	68
4.4.1 Morphology and induced phase separation mechanism.....	68

4.4.2 Mechanical property and crystallization mechanism.	74
4.4.3 Thermal properties analysis	76
4.4.4 N ₂ sorption isotherm and BET surface area analysis	78
4.4.5 Hierarchical porous structures.....	80
4.4.6 Air filtration performance	82
4.4.7 Air filtration quality factor (QF).....	85
4.5 Conclusions.....	89
Chapter 5: Electrospun SF/PLLA Fibrous Membrane Composites towards Vascular Scaffolds	90
5.1 Chapter Synopsis.....	91
5.2 Literature Review: Electrospun Vascular Scaffolds	92
5.3 Materials and Methods.....	94
5.3.1 Materials.....	94
5.3.2 Preparation of SF solution.....	95
5.3.3 SF coating on PLLA fibrous membrane.....	95
5.3.4 Material characterizations	97
5.3.5 Vascular grafts fabrication.....	98
5.3.6 SMCs in vitro study	98
5.3.7 Statistics	99
5.4 Results and Discussions	100
5.4.1 Surface morphology	100
5.4.2 Characterization and material properties of membrane samples.....	107
5.4.3 Multi-layer tunica media scaffolds.....	116
5.4.4 Mechanical evaluation of membrane samples.....	117
5.4.4 Cell viability on fibrous membranes	119
5.4.5 SMCs proliferation and morphology on membrane scaffolds.....	121
5.5 Conclusions.....	126
Chapter 6: Conclusion and Outlook.....	127
6.1 General Conclusion.....	127
6.2 Outlook	128
References.....	130
List of Publications	145

List of Figures

Fig. 1.1 Total publications in Web of Science database search by: “electrospinning” or “electrospun”.	6
Fig. 1.2 The total publications in Web of Science database search by keywords: “electrospinning porous fiber” or “electrospun porous fiber” or “electrospinning porous fibre” or “electrospinning porous fibre”.	7
Fig. 1.3 Schematic illustration to show the overall structure of whole project and thesis visually.	10
Fig. 2.1 The schematic of TL-Pro Electrospinning Unit.	20
Fig. 2.2 Repeat Unit of PLLA.	24
Fig. 2.3 Structure of natural silk fibre.	28
Fig. 2.4 Structure of hydrophobic Crystalline Region of SF.	29
Fig. 2.5 Preparing protocols of silk fibroin solution.	31
Fig. 2.6 The geometric expression of the Hansen and Hildebrand solubility parameters in the Hansen space [49].	41
Fig. 2.7 The isothermal diagram for phase separation scenarios in a polymer/solvent binary phase system [52].	42
Fig. 2.8 The isothermal diagram for phase separation scenarios in a polymer, solvent and non-solvent ternary phase system which illustrates four hypothetical formations and morphologies [53].	43
Fig. 2.9 (a) The porous structure on the casting film formed by breath figure mechanism [54]. (b, c) The porous structure on the electrospun PLA fibre formed by breath figure mechanism and the diagram of the pores forming process [16].	45
Fig. 2.10 The diagram of the pores forming process due to the vapour-induced phase separation mechanism [16].	46
Fig. 3. 1 Schematic diagram with size of paper fixing frame for mechanical test samples.	57
Fig. 4. 1 Schematics of the pristine electrospun PLLA fibre and hierarchical porous PLLA fibre after acetone post-treatment.	60
Fig. 4. 2 The schematic of an electrospinning process.	63
Fig. 4. 3 The photos of a piece of treated PLLA membrane and round air filter samples.	64
Fig. 4. 4 Schematic diagrams of air filtration testing instrument setup.	67
Fig. 4. 5 The air filtration instatement setup.	67
Fig. 4. 6 SEM image of 1.6 wt% (S1-B) electrospun PLLA fibrous membrane before treatment.	70

Fig. 4. 7 SEM image of 1.8 wt% (S2-B) electrospun PLLA fibrous membrane before treatment.	70
Fig. 4. 8 SEM image of 2.0 wt% (S3-B) electrospun PLLA fibrous membrane before treatment.	71
Fig. 4. 9 SEM image of 2.2 wt% (S4-B) electrospun PLLA fibrous membrane before treatment.	71
Fig. 4. 10 SEM image of post-treatment 1.6 wt% (S1-B) electrospun PLLA fibrous membrane.....	72
Fig. 4. 11 SEM image of post-treatment 1.8 wt% (S2-B) electrospun PLLA fibrous membrane.....	72
Fig. 4. 12 SEM image of post-treatment 2.0 wt% (S3-B) electrospun PLLA fibrous membrane.....	73
Fig. 4. 13 SEM image of post-treatment 2.2 wt% (S4-B) electrospun PLLA fibrous membrane.....	73
Fig. 4. 14 Fibre diameter of B group samples, before treatment and post treatment.	74
Fig. 4. 15 XRD patterns of PLLA fibrous membranes.	75
Fig. 4. 16 Stress-strain curves of PLLA fibrous membranes.	76
Fig. 4. 17 DSC traces of samples. Post-treatment sample is shown by solid line and before treatment sample is shown in dotted line.....	77
Fig. 4. 18 TGA curves of samples. Post-treatment sample is shown by solid line and before treatment sample is shown in dotted line.	78
Fig. 4. 19 N ₂ adsorption-desorption isotherms graphs of corresponding PLLA fibrous membranes.....	79
Fig. 4. 20 DFT pore size distribution curves of corresponding PLLA fibrous membranes. N ₂ adsorption-desorption isotherms graphs of PLLA fibrous membranes under different concentrations from 1.6 to 2.2 w/w, identified as the typical Type IV isotherm materials.	79
Fig. 4. 21 Structures of each stage of the electrospinning and the posttreatment process.....	82
Fig. 4. 22 30 nm particles filtration efficiency of membrane samples set in Table. 3.2, with different PLLA wt%.....	83
Fig. 4. 23 50 nm particles filtration efficiency of membrane samples set in Table. 3.2, with different PLLA wt%.....	83
Fig. 4. 24 100 nm particles filtration efficiency of membrane samples set in Table. 3.2, with different PLLA wt%.....	84
Fig. 4. 25 Filtration efficiency of membrane samples with 1-hour continuous filtering test of group B.....	84
Fig. 4. 26 Pressure drop of membrane groups B and C.	85
Fig. 4. 27 Quality factor (QF) of membrane samples for 30, 50 and 100 nm particle sizes.....	85
Fig. 4. 28 Energy-dispersive X-ray element mapping of the front side of the membrane after filtration testing (Carbon, C).....	86
Fig. 4. 29 Energy-dispersive X-ray element mapping of the front side of the	

membrane after filtration testing (Oxygen, O).	86
Fig. 4. 30 Energy-dispersive X-ray element mapping of the front side of the membrane after filtration testing (Sodium, Na).	87
Fig. 4. 31 Energy-dispersive X-ray element mapping of the front side of the membrane after filtration testing (Chlorine, Cl).	87
Fig. 4. 32 EDX elements distribution of front side of filtered sample.	88
Fig. 5. 1 Schematics of the electrospun PLLA fibrous membrane, porous PLLA fibres after post-treatment and silk fibroin coating on PLLA fibres.	92
Fig. 5. 2 Schematics of the materials fabrication methods. (A) electrospinning PLLA fibrous membrane; (B) SF solution preparation; (C) coating; and (D) spraying processing methods.	96
Fig. 5. 3 SEM image of 0.3% SF coated porous PLLA fibre diameter.	101
Fig. 5. 4 The counts of 0.3% SF coated porous PLLA fibre diameter.	101
Fig. 5. 5 SEM image of 1% SF coated porous PLLA fibre diameter.	102
Fig. 5. 6 The counts of 1% SF coated porous PLLA fibre diameter.	102
Fig. 5. 7 SEM image of 3% SF coated porous PLLA fibre diameter.	103
Fig. 5. 8 The counts of 3% SF coated porous PLLA fibre diameter.	103
Fig. 5. 9 SEM image of pristine PLLA membrane.	104
Fig. 5. 10 SEM image of porous PLLA membrane.	105
Fig. 5. 11 SEM image of porous membrane coating SF.	105
Fig. 5. 12 SEM image of porous membrane spraying SF.	106
Fig. 5. 13 XPS survey of pristine and porous PLLA fibres, SF coating/spraying specimens.	107
Fig. 5. 14 XPS fine peak spectral lines of carbon atoms for pristine PLLA fibres.	108
Fig. 5. 15 XPS fine peak spectral lines of carbon atoms for porous PLLA fibres.	108
Fig. 5. 16 XPS fine peak spectral lines of carbon atoms for porous PLLA fibres with SF coating.	109
Fig. 5. 17 XPS fine peak spectral lines of carbon atoms for porous PLLA fibres with SF spraying.	109
Fig. 5. 18 XPS fine peak spectral lines of nitrogen (N) atoms for porous PLLA fibres with SF coating and spraying specimens.	110
Fig. 5. 19 XRD spectra of pristine PLLA fibres, porous PLLA fibres, SF coating and spraying specimens.	112
Fig. 5. 20 Tensile stress–strain curves of pristine PLLA fibres, porous PLLA fibres, SF coating and spraying samples.	112
Fig. 5. 21 Water contact angle of pristine PLLA fibres, porous PLLA fibres, SF coating and spraying samples.	113
Fig. 5. 22 Raman spectra of pristine PLLA fibres, porous PLLA fibres, SF coating and spraying samples.	114
Fig. 5. 23 FT-IR spectra of pristine PLLA fibres, porous PLLA fibres, SF coating and spraying samples.	115

Fig. 5. 24 SEM images of rolled-up SF/PLLA tubular scaffold sample.....	116
Fig. 5. 25 SEM images of cross-section of the multi-layer tube wall.....	117
Fig. 5. 26 The 3D-printed holder for loading tubular scaffolds in mechanical evaluation.....	118
Fig. 5. 27 The schematic of 3D-printed holder to load tubular scaffold for tensile tests.	118
Fig. 5. 28 Cell cultural protocol for fibrous membrane in 12-well plates.	119
Fig. 5. 29 A7r5 cell number count for pristine PLLA fibres, porous PLLA fibres, SF coating and spraying samples on day 1 post seeding.	120
Fig. 5. 30 Alamar blue assay results during cell culture up to day 14 post seeding.	121
Fig. 5. 31 Laser confocal images for the morphology of A7r5 cells growing on the surface of four groups membrane samples at three time points post seeding.	123
Fig. 5. 32 Laser confocal 3D images of pristine membrane after seeding.....	124
Fig. 5. 33 Laser confocal 3D images of porous membrane after seeding.....	124
Fig. 5. 34 Laser confocal 3D images of porous membrane with SF coating after seeding.	125
Fig. 5. 35 Laser confocal 3D images of porous membrane with SF spraying after seeding.	125

List of Tables

Table 2.1 Details of previous studies of fabricating electrospinning porous PLLA fibres.	15
Table 2.2 Infrared spectroscopy (FT-IR) characteristic peaks of PLLA.	26
Table 2.3 The diffraction peak of Silk I [43].	34
Table 2.4 The diffraction peak of Silk II [43].	35
Table 2.5 Infrared spectroscopy characteristic absorption peaks of proteins.	36
Table 2.6 The comparison of current mainstream air filtration devices fabrication strategies.	51
 Table 3. 1 General experimental parameters of electrospinning method in this project.	 54
 Table 4. 1 Properties of solvents used in this project (boiling point; viscosity (η); dielectric constant (ϵ); Hansen solubility parameter (δ) [47]; vapour pressure).	 62
Table 4. 2 Electrospinning parameters. ,.....	64
Table 4. 3 Specific surface area (BET) for before and after acetone treatment samples.....	79
Table 4. 4 Filtration efficiency of membrane samples.	88
 Table 5. 1 The Strain and ultimate tensile strength of three groups of tubular scaffolds.	 119

Abstract

Fibres are of great importance to various applications in human's work and lifetime. Electrospinning is a facile and versatile technique to produce ultrafine fibres that range from macro to nano scales. Hierarchical porous structures could increase interactive interfaces between ultrafine fibres and their environments. However, the gaps between by controlling fibre morphology and elevating surface area have not been filled yet.

In this project, a poly(L-lactic acid) (PLLA) hierarchical porous fibrous membrane was designed and developed via an electrospinning and post-treatment strategy. The vapour induced phase separation and solvent induced re-crystallization mechanisms were proposed to explain the generation of porous nano fibres with ultra-high surface area and good interconnectivity based the comprehensive characterizations.

Ultrafine particulate aerosols less than 100 nm diffuse randomly in the air and are hazardous to the environment and human health. However, these small particulate matters are difficult to remove from the air. Due to the elevated specific surface area and highly porous surface morphology, hierarchical porous PLLA fibrous membrane is more possible to capture and intercept fine aerosol particles. Thus, hierarchical porous fibrous membrane was applied as an ultrafine particulate aerosols filter. The filtration performance and pressure drop of the membrane were characterized and its quality factor was calculated.

Pure PLLA porous fibres still face the disadvantages including relatively brittle mechanical and hydrophobic properties. Silk fibroin was used to coating on the surface of porous PLLA fibres successfully. Good cell morphology was observed via a multiphoton laser confocal microscope on electrospun PLLA/SF fibrous membranes. The membrane then rolled up towards vascular scaffolds.

Declaration

The material contained within this thesis has not previously been submitted for a degree at The University of Manchester or any other university. The research reported within this thesis has been conducted by the author unless indicated otherwise.

Copyright Notice

The following four notes on copyright and the ownership of intellectual property rights must be included as written below:

- 1) The author of this thesis (including any appendices and/or schedules to this thesis) owns certain copyright or related rights in it (the “Copyright”) and s/he has given The University of Manchester certain rights to use such Copyright, including for administrative purposes.
- 2) Copies of this thesis, either in full or in extracts and whether in hard or electronic copy, may be made only in accordance with the Copyright, Designs and Patents Act 1988 (as amended) and regulations issued under it or, where appropriate, in accordance with licensing agreements which the University has from time to time. This page must form part of any such copies made.
- 3) The ownership of certain Copyright, patents, designs, trademarks and other intellectual property and any reproductions of copyright works in the thesis, for example graphs and tables, which may be described in this thesis, may not be owned by the author and may be owned by third parties. Such Intellectual Property and Reproductions cannot and must not be made available for use without the prior written permission of the owner(s) of the relevant Intellectual Property and/or Reproductions.
- 4) Further information on the conditions under which disclosure, publication and commercialisation of this thesis, the Copyright and any Intellectual Property and/or Reproductions described in it may take place is available in the University IP Policy (<http://documents.manchester.ac.uk/DocuInfo.aspx?DocID=24420>), in any relevant Thesis restriction declarations deposited in the University Library, under regulations (<http://www.library.manchester.ac.uk/about/regulations/>) and in The University’s policy on Presentation of Theses.

Acknowledgement

First, I would like to acknowledge my PhD project supervisor Dr. Jiashen Li. It would be one of the luckiest things that I was supervised by him to pursue my doctoral degree in my lifetime. I cannot accomplish my research project and this thesis without his unselfish assistance. Your motto, self-restraint, will always inspire me in my future career.

Then, I acknowledge my friends, Dr. Xi Yang, Dr. Kewen Pan, Mr. Zhongda Chen, Mr. Luis Larrea, and Mr. Tianlei Ma for their help about my study and life in England. I am also grateful to the other research students in our group, including Dr. Zhiying Xin, Mr. Ting Liu, Mr. Qasim Zia, Miss. Jinmin Meng, Miss. Zihan Lu, Mr. Wenyuan Wei, Mr. Chen Meng, Mr. Zekun Liu, and Miss Yilu Chen for their suggestions or assistance of my theoretical and experimental study.

In addition, I am eternally grateful to my co-supervisor, Dr. Hugh R Gong, for his enlightening guidance and valuable helps.

The University of Manchester is an institute highly prestigious globally. I acquired a lot of knowledge not only in my research subject but also in other science, engineering, and even social science subjects. I appreciate the support from researchers and staff including Ms. Damindi Jones, Dr. Teruo Hashimoto, Dr. John Warren, Dr. Richard Fields, Dr. Paul I Williams, Dr. Michael Flynn, from Mez lab, Electron Microscope Centre, XRD suite, National Graphene Institute, and National Centre for Atmospheric Science in The University of Manchester.

The most important, I want to express my gratitude for my parents' endless support. My parents, Yuanlong Han & Qian Song, fully funded me to pursue this degree. They also kept encouraging me when I was down or depressed.

To mourn my maternal great-grandfather Jian Tang (1920.04-2020.11)

Abbreviations

PLLA	Poly(L-lactic acid)
PLA	Poly lactic acid
SF	Silk fibroin
RSF	Regenerated silk fibroin
LiBr	Lithium bromide
DCM	Dichloromethane
DMF	N, N-dimethylformamide
SEM	Scanning electron microscopy
FTIR	Fourier transform infrared spectrometer
XPS	X-ray photoelectron spectroscopy
XRD	X-ray diffraction
FWHM	Full width half maximum
TGA	Thermogravimetric analysis
DSC	Differential scanning calorimeter
WCA	Water contact angle
BET	Brunauer-Emmett-Teller
μm	micrometre
nm	nanometre
Da	Dalton
IUPAC	International Union of Pure and Applied Chemistry
PRC	Peoples' Republic of China
UK	United Kingdom of Great Britain and Northern Ireland
USA/US	United States of America

Chapter 1: Thesis Introduction & Research Objectives

1.1 Research Motivation

How long the history of human civilization has been, how long fibres have been applied by the human beings. With thousand-years development, fibres have extended their applications from conventional textiles to biomedicine, electronics, defence, and sustainable development industries. Nanofibres, as a typical nanomaterial with the characteristics of both the micro (molecule) and macro (substance), have been attracting the attention of researchers worldwide during the first two decades of this century [1]. Electrospinning technology is the major fabrication method to produce nanofibres. As the Fig. 1.1 presented, electrospinning technology has raised wide interesting among the researchers worldwide since the end of last century. Most researchers have investigated and reported the fabrication methods, theories, and material properties of electrospun fibres. However, the applications of electrospun fibres have not been confirmed yet.

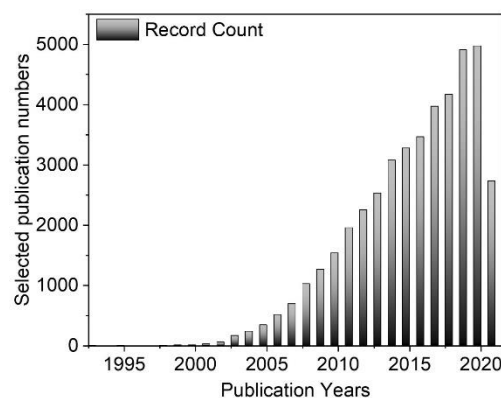


Fig. 1.1 Total publications in Web of Science database search by: “electrospinning” or

“electrospun”.

Meanwhile, researchers and the whole society are seeking a substitute for petroleum-based chemical fibres due to the sustainable development goals including carbon neutral [2]. As an alternative, poly (L-lactic acid) (PLLA) is an eco-friendly and naturally degradable polymer which suits for environmental protections and tissue engineering applications. It is neither harmful to humans nor to the environment and has been widely used in the biomedical field and for environmental protection. Hence, PLLA has become one of most popular material for electrospinning fabrication. Electrospun PLLA fibre has the advantages in high porosity and interconnectivity, which show the prospects for improving interactive efficiency or sensitivity among interfaces. Thus, to further elevating the specific surface area of electrospun PLLA fibres received continuous attention since 2001 [3], as Fig 1.2 shown. Applying extra method to treat electrospun PLLA fibres more porous or rougher is worthy to be investigated. This research project focused on the fabrication of electrospun porous nanofibres to significantly elevate their specific surface area and exploring application of electrospun porous fibrous materials.

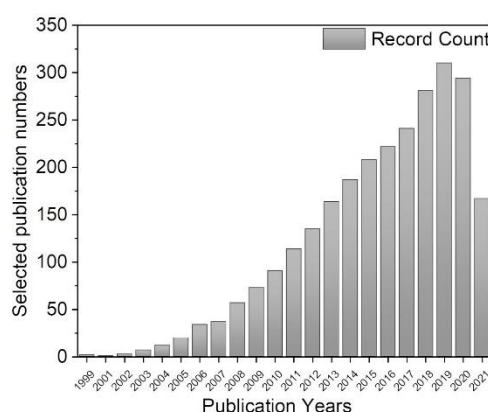


Fig. 1.2 The total publications in Web of Science database search by keywords: “electrospinning porous fiber” or “electrospun porous fiber” or “electrospinning porous fibre” or “electrospinning porous fibre”.

Nowadays, the nanofibre fabrics from silk fibroin have been applied in some areas

including environmental protecting adsorption membrane, biocompatibility tissue engineering scaffold and so on. Quickly and efficiently prepared with high specific surface area of porous fibres will greatly promote its application in the field of the above. The two raw materials used in this project, poly(L-lactic acid) (PLLA) and silk fibroin (SF), are both biodegrade and biocompatible which means they are consistent with sustainable development goals. Silk Fibroin, as a natural protein, was taken into consideration for tissue engineering. This kind of bioactive material outperforms than the synthetic polymers in cells adhered growth. Easy preparation and low toxicity are the other superiority for natural material whilst its mechanical properties usually under instability when the degradation starts.

1.2 Research Gaps

Beginning with the investigation of electrospinning fabrication method, the preparing parameters should be taken into consideration. So, the research gaps of this projects are followed:

- 1) How to fill the gap between controlling morphology and elevating surface area?
The mechanism of pores forming on the electrospun fibres during spinning and post-treating process.
- 2) Current devices and standard only focused on the air particles more than 300 nm.
How to investigate the PLLA fibrous membrane filtration performance for the aerosols under 100 nm?
- 3) PLLA is hydrophobic. The SF aqueous solution coating method should be optimized. And the coating parameter should be investigated to make sure the PLLA/SF turned to hydrophilic while the high roughness hierarchical porous structure is maintained. Electrospun materials has demonstrated its potential application in vascular scaffold. However, how the conventional electrospun mat could be further fabircated towards tube while the cell lines could be seeded?

1.3 Research Objectives

Despite of the fabrication work, the possibility the materials for applications also need to be demonstrated. To filling the research gaps listed, the research objectives of this projects are followed:

1.3.1 Objective 1: Confirm fabrication method for hierarchical PLLA fibrous membrane

- 1) Based on a comprehensive review about approaches for electrospun porous fibres.
- 2) Review current theory of the mechanism about PLLA fibres and expand theory to cover this project.
- 3) Confirm the general research materials and methods for hierarchical PLLA fibrous membrane.

1.3.2 Objective 2: Apply hierarchical porous PLLA fibrous membrane as a ultrafine particulate aerosol filter

- 1) Fabrication of PLLA electrospun porous fibres and collecting as the hierarchical porous fibrous membrane.
- 2) Investigating the aerosol filtration application of hierarchical porous PLLA fibrous membrane.

1.3.3 Objective 3: Modify PLLA fibrous membrane by SF as a tubular scaffold for muscular artery regeneration

- 1) Coating SF on the surface of PLLA porous fibre to modify its properties.
- 2) Evaluating the potential application of PLLA/SF porous fibres as a matrix towards tissue engineered vascular scaffold.

1.4 Project Significance & Originality

Fig. 1.3 presents the technology roadmap of whole project and thesis visually. In order to further increase the surface area of polymer nanofibres, a two-step strategy has been developed to produce a hierarchical porous structure in this study. After PLLA

nano/micro fibres were electrospun and collected, they were treated by acetone to recrystallize polymer chains and generate a blossoming porous structure.

The PLLA or PLLA/SF fibres are macro scale materials whereas the pores of their surface are nanoscale. Thus, the proposed mechanism introduced in this thesis are related to complex multi-scale systems.

The filtration efficiency of porous PLLA fibrous membranes was examined against aerosol particles from 30 to 100 nm. The current studies only focused on the polluted particles are larger than 300 nm.

Good smooth muscle cell attachment and proliferation on the SF/PLLA fibrous membrane demonstrated the prepared materials are potential to be the vascular scaffolds. The porous membrane could mimic a multi-layer tunica media from the electrospun fibrous membrane.

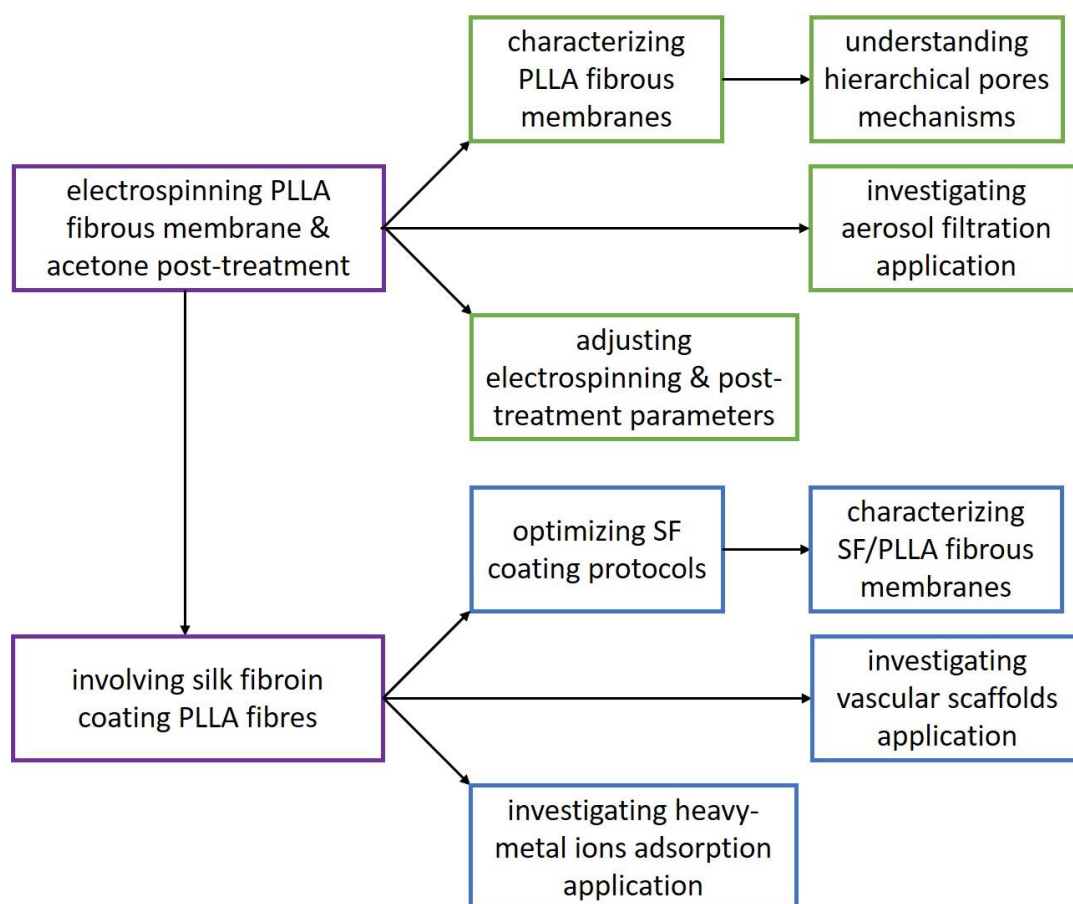


Fig. 1.3 Schematic illustration to show the overall structure of whole project and thesis visually.

Chapter 2: Background Theory & Literature

Review

2.1 Electrospinning: A Facile Nano/Micro Fibre Producing Technique

2.1.1 Definition of electrospun porous fibres

Electrospinning is a method for producing sub-micron or nano-fibres by ejecting a polymer solution or melt in a high voltage electric field to form fibres, and the fibres are usually collected as a membrane. Compared with other polymer processing methods (e.g., casting, drawing, template synthesis and self-assembly), electrospinning method is the only one to prepare continuous sub-micron or nanofibres of various polymers or inorganics with low cost and large productivity. The ability to prepare porous fibrous fibres with high specific surface area to volume ratio is the most important advantage of the electrospinning technology.

Regarding the scale of the electrospinning fibres, and the requirements of their applications, the mainstream shape of collected electrospinning fibres are fibrous membranes. Fibrous membranes are always highly porosity and interconnectivity. Moreover, electrospun membrane usually has a smaller fibre diameter and a higher specific surface area if it is compared with traditional non-woven fabric. Due to the above two advantages, electrospun fibrous membrane have been or potential to be used as filtration and separation membranes, composites, high performance technical textiles, wearable smart textiles, wound dressings, and implantable drug delivers or scaffolds.

Electrospinning is a complex process influenced by many factors, including polymer solution properties, instrumental settings, and environmental parameters. It has been a mature research area for investigating of electrospun a range of polymers or

inorganics under different working conditions, whereupon the morphology of electrospinning fibres could be controlled via adjusting these parameters. Not only ordinary solid or bead nanofibres, but also band, spiral, core-shell, hollow and porous nanofibres have been prepared and studied systematically. Among them, the fibres with porous surface morphology can significantly elevate the specific surface area, which is one of the most critical advantages of electrospinning technology. Hence porous structured nanofibres received more attention than other morphologies by reason of its relatively high specific surface area.

It should be clarified that most of early studies have defined the voids among electrospun nanofibres are stacked into a film as a porous structure. Conventional electrospun fibre membranes can indeed be considered as porous membrane materials. However, the porosity discussed in this study mainly refers to the porous morphology features visible on each single fibre. Therefore, this dissertation acknowledges both the early studies and the positions of the researchers in the past decade, and defines the porous fibrous membrane discussed in this article as a hierarchical porous fibrous membranous material. Specifically, the size of the voids between fibres is generally on the micron level. The holes on the surface of electrospun fibres are more of the nanoscale level. Nano-porous materials are classified into three types of pores according to International Union of Pure and Applied Chemistry (IUPAC) classification. These are microspores with a size of less than 2 nm; macrospores with a size larger than 50 nm; and mesoporous between 2 nm and 50 nm. According to the research articles published by our research group and other academic peers in recent years, the surface pores of electrospun nanofibres are mainly mesoporous and macroporous structures.

2.1.2 Hierarchical porous electrospinning fibrous membrane: fabrication strategies

As the above section mentioned, electrospinning is a technology could produce either polymer or inorganic porous fibres. However, the fabrication strategies for porous inorganic fibres are far different from porous polymer fibres. This review mainly focused on hierarchical porous polymer fibres.

Electrospinning is a complex process which is influenced by many factors, including polymer solution properties, instrumental settings, and environmental parameters. Thus, the morphology of electrospun fibres can be controlled via adjusting these parameters. In addition to ordinary solid or bead nanofibres, some band, spiral, core-shell, hollow, and porous nanofibres have been prepared and studied [4–7]. Porous materials are classified into three types of pores according to the IUPAC [8]. They are microspores with a size of less than 2 nm; macrospores with a size larger than 50 nm; and mesoporous between 2 and 50 nm which are the focus of this research.

The molecular weight of the polymer is one of the most important parameters affecting electrospinning due to its direct influence on the rheological and electrical properties of the solution, such as the viscosity, surface tension, conductivity, and dielectric properties of the solution. The first factor should be noticed is that small molecule polymer solution cannot be electrospun. If fibres are going to be prepared by electrospinning, the polymer used must have a certain high molecular mass and a certain viscosity after dissolution. Otherwise, the preparing process can only be defined as an electrostatic atomization process. The final products will be the aerosol or polymer microspheres instead of electrospinning fibrous membrane.

The molecular weight of a polymer also directly reflects the length of its molecular chain. A large molecular mass means that the molecular chain length of this polymer is relatively long. And a polymer with a longer molecular chain could entangle easily in its solution, thereby increasing the viscosity of the solution. For the polymer solutions with the same molecular mass, the viscosity of the high molecular weight polymer solution is greater than the low molecular weight polymer solution.

Koski's research shows the relationship between molecular mass and the electrospun polymer solution has a certain concentration [9]. When the polymer's molecular mass is 9-10 kDa, the obtained electrospun fibres are bead-like fibres, which indicates that the polymer jet breaks during electrospinning and the molecular chain violates the full stretched orientation. The electrospun fibres obtained are beads with an average diameter of between 0.5-1.25 μm when the polymer relative molecular weight is 13-23 kDa, which means that with the relative molecular weight increasing, the

entanglement of the molecular chains in the solution also elevated, and the polymer jet stretching during electrospinning results in a good orientation of the molecular chains and resistance to external forces without fracture. The electrospun fibres are ribbon-like bead fibres with an average width of 1-2 μm , when the relative molecular mass is increased to 31-50 kDa. Furthermore, the degree of entanglement of the molecular chains in the solution directly affects the formation of beads in the fibre membrane. High molecular weight polymers can be electrospun at even lower concentrations and obtained uniform fibres. Low molecular weight polymers must be electrospun fibres at higher concentrations. Otherwise, only polymer microspheres will be obtained.

Upon the relative molecular weight of the polymer determined, the concentration of the solution is the most decisive factor which influences the entanglement of the molecular chain in the solution under certain other conditions. Polymer solutions can be simply divided into three types: dilute polymer solutions, semi-dilute solutions, and concentrated solutions, depending on the concentration and molecular chain morphology. The key difference between a dilute solution and a concentrated solution is whether the individual polymer chain clumps exist in isolation and overlap with each other. In dilute solutions, the molecular chains are separated from each other and have a uniform distribution. As the concentration of the solution increases, molecular chains interpenetrate each other, and tangles occur. The boundary concentration of the dilute solution and the semi-dilute solution is called the contact concentration (c^*), which refers to the concentration at that the molecular chains encounter each other and then overlap each other during the solution concentration increasing. The boundary concentration of the semi-dilute concentration and the concentrated solution is called the entanglement concentration (c_e), and it refers to the concentration at those molecular chains interpenetrate and entangles with each other during the solution concentration increasing.

As the concentration of the polymer solution increases, the viscosity of the solution changes significantly, and the viscosity of the solution is closely related to the molecular weight of the polymer. Based on the general laws of polymer molecular weight, solution concentration and viscosity on the morphology of electrospun fibres, the

electrospinning fibre morphology can be controlled by adjusting the nature of the solution. Research referring to fabricating electrospinning porous fibrous membrane have been done, especially choosing poly (lactic acid) (PLA) as the raw material [10–12]. Here Table 2.5 demonstrated some major works about the porous fibre structures.

Table 2.1 Details of previous studies of fabricating electrospinning porous PLLA fibres.

Solvent	Mechanism	Morphology	Time/reference
DCM	vapour induced phase separation	Pores or pits in the 100nm range	2001, [3]
BuOH	phase separation of nucleation and growth	micro-pores on the surface of fibres	2009, [13]
DCM/DMF	Breath figure and evaporation induced phase separation	Pits/pores on flat fibres	2014, [14]
DCM/DMF	Influenced by take-up velocity and crystallization ability of polymer	Porous nanofibres appeared in low take-up velocity	2015, [11]
DCM/DMAC	phase separation, breath figure, and solidification of fluid jet	nanopores densely distributed on the fibre surfaces and interior	2015, [6]
DCM/ Hexane	phase separation and spinodal decomposition	Porous fibres	2017, [15]
DMSO	Breath figures	surface porosity	2018, [16]

The fluid molecules are constantly making Brownian motions, and there are mutual gravitational forces between the molecules which make up the fluid. Within a certain range, the smaller the distance between molecules is, the greater the attraction

will be. The attraction between molecules of the same type is called cohesion. It causes the molecules on the liquid interface to move closer to each other and manifest itself as liquid surface shrinkage. This force acting on the liquid surface and trying to shrink the liquid surface to a minimum area is called surface tension. Electrospinning solution is generally composed of macromolecule polymer and solvent, belonging to the binary system. Its surface tension is different from that of one-component fluid. It is not only related to temperature and pressure but also related to the composition of the solution.

As a low concentration polymer solution, the solvent fraction is high, and the solvent molecules tend to aggregate to form a spherical shape due to surface tension. Increasing the concentration of the solution can reduce the surface tension of the solution to a certain extent, which is advantageous for the formation of continuous and uniform fibres. At higher concentrations, the viscosity of the solution increases, indicating that the interaction between the polymer molecular chain and the solvent is enhanced, and the solvent molecules tend to separate the entangled molecular chains, reducing their tendency to aggregate and contract. When the concentration of the polymer solution is confirmed, the surface tension of the solution can be adjusted by changing the composition of the solvent, and the morphology of the electrospun fibres can also be changed.

Electrospinning relies on the electrostatic repulsion of a polymer solution to produce a small jet of polymer that cures to form fibres. The conductivity of the polymer solution directly influences the morphology of fibres. It is related to the chargeability of the polymer solution. Increasing the charge of the polymer solution can increase the conductivity of the solution. The jet formed by the high-conductivity polymer solution is greatly affected by the electric field force. If the conductivity of the solution is low, the jet is subjected to weaker stretching action, and it is easy to obtain the bead fibres. Increasing the conductivity of the solution increases the charge density on the surface of the jet. At this time, the axial whip instability of the jet dominates the position, which can reduce the fibre diameter and widen the fibre diameter distribution. As the conductivity of the solution increases, not only the fibre morphology is affected, but also because the instability of the polymer jet in the high voltage electric field increases,

the fibre deposition area can also be increased. Via adding salt, polyelectrolyte and altering the solvent composition in the polymer solution, the conductivity of the spinning solution can be adjusted to achieve the purpose of regulating the morphology of the electrospun fibres.

The main role of the solvent is to dissociate the molecular chain of the polymer. During the electrospinning process, the solution forms a jet, which is highly stretched by the electric field force, and the polymer molecular chain is reoriented and aligned. Along with the volatilization of the solvent, the jet is cured as fibres. In this process, solvent properties such as dielectric constant, conductivity, volatility, and solvent solubility to polymer affect the electrospinning process, which in turn affects the morphology of the electrospun fibres. In general, the high dielectric constant of the solvent indicates that the solvent has a strong charge-carrying capacity, which makes the surface of the jet carry more charges. When the surface of the jet has a large number of electrostatic charges, the non-axisymmetric instability of the jet dominates. It can cause unstable jets to split into smaller jets, thus forming fibres of uneven thickness; the conductivity of the solvent is large, the conductivity of the corresponding solution is good, and the electric force acting on the solution jet is stronger, which is beneficial to reduction. The diameter of the small electrospinning fibre, the volatility of the solvent affects the stretching and curing of the jet, the solvent volatilizes too quickly, the solution is difficult to form a Taylor cone at the nozzle, the nozzle is blocked, the spinning process is difficult, and the solvent volatilizes too slowly that polymer jet is still not cured after it is deposited on the receiving device, which can easily cause fibre adhesion. In addition, the volatility of the solvent also influences the phase separation and solidification process of the solution during the jet stretching process, thereby affecting the morphological structure of the electrospun fibre, and forming some special structures such as a rough surface, a porous surface, and a flat cross-section. The solubility of a polymer is related to the entanglement state of the polymer molecular chain in the solvent. For a polymer, there is a good solvent and a non-good solvent, and the viscosity of the same mass fraction of the polymer in its good solvent. Unlike surface tension, blending solvents can be used to regulate the morphology of

electrospun fibres.

The temperature of the polymer solution affects not only the viscosity of the solution but also the volatilization of the solvent during electrospinning. When the temperature of the polymer solution increases, the viscosity of the solution can be greatly reduced. At the same time, the entanglement of the molecular chains in the solution is hardly affected. Therefore, the morphology of the electrospun fibre can be controlled by adjusting the temperature of the spinning solution.

The key difference between electrospinning technology and conventional spinning technology is that it relies on the electric charge forced on the surface of the polymer fluid to generate electrostatic repulsion to overcome its surface tension, resulting in a tiny jet of polymer solution that evaporates after solvent evaporation and curing into fibre finally.

Although voltage and rotating speed seem to be quite different, the effects of these two parameters on fibre morphology are similar and minor. Generally speaking, higher voltage will cause a small increase in fibre diameter due to the destruction of the continuous polymer jet. A smaller voltage can achieve a smaller fibre diameter under the condition that the polymer solution can be stretched. Rotating speed is more like the drafting or drawing process in the traditional fibre manufacturing technologies.

In the electrospinning process, increasing the voltage or increasing the electric field strength will increase the charge on the surface of the polymer solution jet, resulting in an increase of the electric field force to the jet's tensile effect. If the concentration and viscosity of the polymer solution are low, molecular chain entanglement is not enough, and the surface tension of the solution is large, and the molecular chain will break and contract to form polymer beads in the orientation process. As the voltage increases, the instability of the jet increases, and the probability of such a fracture also increases, resulting in an increase in the number of beads in the fibrous membrane. At the same time, due to the entanglements between the molecular chains, the fibres between the polymer beads are greatly reduced in diameter under severe tensile action. In the case of high concentration of polymer solution, the corresponding solution viscosity is also greater, the molecular chain entanglement in

the solution is larger, the viscosity of the solution is increased, there is a certain degree of inhibition of external electric field force, and the effect on voltage of fibre morphology is not obvious. According to the analysis of the jet motion, after the voltage is increased, the charge on the surface of the jet increases, and the whipping of the jet increases, which is advantageous for reducing the diameter of the fibre.

Another study found that the polarity of the voltage of the DC high-voltage power supply used has little effect on the spinning process, but the negative-electrode spinning of the DC high-voltage power supply can slightly increase the fibre diameter and narrow the fibre diameter distribution. This is mainly due to the use of DC high voltage power supply. Negative spinning, the jet movement speed is faster, the charge during the spinning process can be more evenly distributed in the jet surface, reducing the whipping instability of the jet.

The injection rate of the polymer fluid to a certain extent determines the amount of spinnable solution in the electrospinning process. For a given voltage, a relatively stable Taylor cone is formed at the showerhead. Under certain voltage conditions, the diameter of the jet will increase with the injection speed of the fluid within a certain range, resulting in an increase in fibre diameter, and a positive correlation between fibre diameter and injection speed. For a given voltage and fibre receiving distance, the shape of the Taylor cone changes with the injection speed. If the injection speed is too low, the Taylor cone will be unstable, and the instability of the jet will increase, affecting the fibre's topography. If the injection speed is too high, the Taylor cone will behave oscillating and affect the fibre's topography.



Fig. 2.1 The schematic of TL-Pro Electrospinning Unit.

Normally, electrospun nanofibres were collected as a fibrous stacking membrane [17]. Regarding electrospun membranes perform well in porosity and interconnectivity, biomaterials application including tissue engineering scaffold and drug delivery are the principal applications for electrospun membranes. In the electrospinning process, the receiving distance of the fibre (the distance from the tip of the nozzle to the fibre receiving device) directly affects the strength of the electric field, thereby affecting the degree of stretching and flight time of the jet in the electric field. In solution electrospinning, for a single electrospun fibre, the solvent in the jet must be volatilized to cure to form the polymer fibre. Under the same conditions, if the fibre receiving distance is shortened, the electric field intensity is increased, the jet velocity is increased, and the flight time is shortened, which may result in incomplete solvent evaporation and partial adhesion among fibres.

The fibre receiving distance has a double effect on the fibre diameter. Changing the fibre receiving distance directly affects the strength of the electric field and the flight time of the fibre in the electric field. A larger receiving distance can provide sufficient time for the jet to fully stretch and is also conducive to the volatilization of the solvent,

which can reduce the diameter of the fibre; on the other hand, increasing the fibre receiving distance reduces the electric field intensity, which is the decrease of the jet acceleration. The weakening of the stretching effect leads to an increase in the fibre diameter. Therefore, the competitive relationship between these two effects determines the size of the fibre diameter.

In the process of high-pressure electrospinning using polymer fluids, there must be a critical voltage value so that the charge repulsion on the surface of the droplet at the end of the nozzle is greater than the surface tension of the liquid to form a jet. This value is usually related to the size of the spinning fluid droplets, the smaller the droplets, the smaller the critical voltage, which is more conducive to electrospinning. Therefore, the role of the showerhead in the electrospinning process is to generate small droplets of fluid, providing a base point for jet formation.

In the electrospinning process, the charged jet flows from the jet head to the receiving device under the action of the high-voltage electric field. Dissipation of the residual charge on the polymer fibres can affect the deposition of the fibres, and the fibres exhibit different arrangements.

Solution electrospinning is generally performed at room temperature. During this process, the influence of ambient temperature is manifested in many ways. As discussed in the previous solution properties regarding the effect of solution temperature on the electrospinning process and the fibres obtained, increasing the ambient temperature of the electrospinning first accelerates the movement of molecular chains in the jet and increases the conductivity of the solution; Secondly, increasing the ambient temperature of the electrospinning reduces the viscosity and surface tension of the solution, so that some polymer solutions that cannot be electrospun at room temperature can be electrospun after raising the ambient temperature.

In the electrospinning process of the solution, the jet is formed on the surface of the Taylor cone and rapidly moves toward the receiving plate. The solvent quickly evaporates in a very short time, and the jet solidifies into the polymer fibre. In the general electrospinning environment, the medium around the jet is air, and the exchange of solvent and surrounding medium in the jet is a double diffusion process. The solvent

on the jet surface volatilizes. The internal solvent diffuses from the centre to the surface. The competition relationship between the evaporation rate of the solvent on the jet surface and the diffusion rate of the internal solvent can affect the fibre morphology. Under fixed spinning conditions, ambient humidity directly affects the properties of the media surrounding the jet, especially its compatibility with the solvent in the jet. If the humidity and solvent compatibility is good, increasing the ambient humidity will always remove the solvent in the jet, so that the jet curing speed slows down; otherwise, it can speed up the solvent evaporation, the jet curing speed.

Extensive research studies regarding electrospun porous fibrous membranes have been carried out by many groups, especially using polylactic acid (PLA) as the raw material. In early-stage research, Bognitzki selected dichloromethane (DCM) as a volatile solvent to electrospin PLLA fibres with pores on their surface [3]. However, using other volatile solvents, such as chloroform and acetone, could not guarantee a porous morphology on the surface of electrospun PLLA fibres [8]. Butanol or dimethyl sulfoxide was also reported as a single solvent to prepare micropores on the fibre surface [11,16]. Natarajan used a PLLA/DCM/dimethyl formamide (DMF) ternary solution system for electrospinning and observed a high surface porosity [14]. Some other dual-solvent systems for porous PLLA fibres were also reported, such as acetone/DMF, DCM/dimethylacetamide, and DCM/hexane [5,14,18].

2.2 Poly(L-lactic acid) (PLLA)

2.2.1 Materials properties

Poly(lactic acid) (PLA) is a light yellow or transparent substance with a molecular weight ranging from several thousand to hundred thousand. The density of the amorphous PLA pellets is 1.248 g/cm³, while the density of the crystallized PLA pellets is 1.290 g/cm³. Therefore, the density of common PLA samples should be between these two figures. The glass transition temperature (T_g) of PLA is 50-70°C, and the melting point is 130-215°C.

Poly (lactic acid), also known as polylactide, is the polyester that is dehydrated

and condensed from lactic acid in a certain processing. Ordinary raw materials are starch, sugarcane, and corns generally for industrial producing PLA. As lactic acid is a common natural compound in animals, plants, and microorganisms, its polymerisate, PLA, can be completely biodegraded, has no pollution to the environment, and is also a kind of good biocompatibility in the polymer. Although, this polymer refers to a 'poly acid', it is a coincidence with the typical properties of polyester such as thermoplastic, outstanding mechanical property and eco-friendly. Poly (lactic acid) is a chiral polymer which contains asymmetric carbon atoms. Two different isomers, L- and D- lactic acid, could be synthesized into different PLAs. PLLA is more widely applied because most biomaterial resource of isomers is L-lactic acid.

Regarding the raw material of this study, the review, result and discussion only refer to the PLLA. PLLA is soluble in dichloromethane (DCM), ethylene oxide, acetonitrile, chloroform, dichloroacetic acid, and trichloroethane. At room temperature, PLLA can only partially be dissolved in ethylbenzene, toluene, acetone, and tetrahydrofuran, and is easier dissolved when heated to boiling. Crystallized PLLA is insoluble in acetone, acetic acid and tetrahydrofuran. PLLA is always insoluble in water, ethanol, methanol, and alkanes in all cases, and is easily hydrolysed to produce lactic acids. Since PLLA has a high degree of crystallinity, this leads to its low gas permeability.

PLLA is a tough and brittle plastic. Compared with ordinary petroleum-based plastics including polypropylene (PP) and polystyrene (PS), PLLA has higher mechanical strength and modulus, but lower elongation at break and impact strength. The changes in mechanical properties between different PLLAs are mainly affected by their molecular weight, D-type lactic acid content, and high-level ordered structure, i.e., crystallinity, lamella thickness, spherulite size, and degree of molecular chain orientation. In general, PLLA has good processability and mechanical properties like PP and PS.

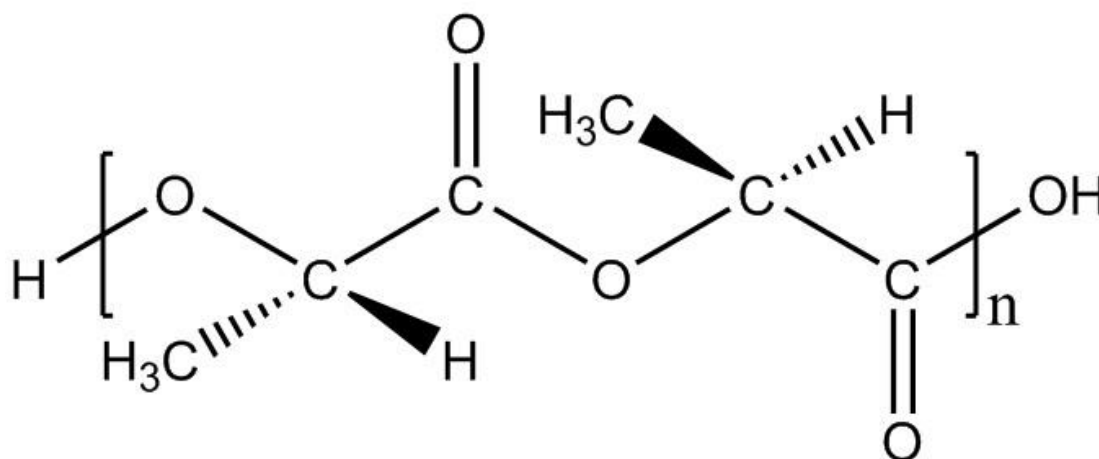


Fig. 2.2 Repeat Unit of PLLA.

2.2.2 Spinning towards fibres and electrospinning

Fabricated by a fibre fabrication method, electrospun fibres have a certain degree of lattice orientation. Specifically, when the dotted jet is ejected at top of the needle, it is highly stretched in the axial direction due to the presence of an applied electric field. However, fibres are generally not oriented during the process of stacking to form fibrous membranes. Although there have been some solutions to increase the degree of orientation, traditional electrospun fibre membranes are not oriented. Orientation can improve the tensile strength, impact strength and elastic modulus of PLLA fibres or fibrous membranes. But the elongation at break will decrease if the fibrous membrane is highly oriented. When fibre formed, the improvement of stretching effect can increase the crystallinity of PLLA. Because the mechanical properties perpendicular to the stretching direction are relatively poor, a fibrous membrane with a low degree of orientation is not necessarily a bad thing.

Electrospinning technology can prepare PLLA fibres with a diameter of submicron or nanometer level. Due to its mechanical properties are close to skin and cartilage, PLLA is expected to be used as a scaffold for artificial skin or cartilage regeneration. However, the strength and crystallinity of electrospun PLLA fibre is not satisfied yet. PLLA's potential applications are limited to biomedicine and other fields. At the same time, the production efficiency is low. At present, it is far from reaching the

requirements of large-scale production and application.

Electrospun fibrous membranes with high specific surface area and porosity can be used as efficient adsorption carriers, catalyst templates, and medical anti-adhesion isolation membranes.

Electrospinning is a method for producing nanofibres by letting a polymer solution or melt which is a flow of non-Newtonian fluid to be ejected with charge. In other words, it is a process of polymer spinning using electrostatic force. To conduct a successful process of electrospinning, the following features should be satisfied as the order of the processing protocols: 1) there is a suitable solvent with volatility to dissolve the polymer. 2) The polymer solvent has a suitable vapour pressure, which ensures that the polymer fibres can maintain integrity until it reaches the receiving device. However, the evaporation cannot be too fast to cause polymer fibres to become harden before it turns into nanoscale. 3) The viscosity and surface tension of the polymer solvent should not be too large to prevent the ejecting, nor too small to contribute to the unrestricted flow of polymer solution in the pipette. 4) The voltage is guaranteed to overcome the viscosity and surface tension of the polymer solution, allowing the ejecting occurs continuously. 5) The distance between the pipette and the receiving device should be long enough to avoid sparks between the two electrodes. But this distance should be kept allowing the solvent to volatilize in time, resulting in fibre formation.

2.2.3 Properties of PLLA

Mechanical performance is one of main indicator for the property of fibrous membranes. Degradation performance has a significant impact on the performance of filtration and separation materials, biomaterials, and flexible wearable materials. For this study, here is a brief introduction to the influence of molecular weight, crystallinity, and orientation on the mechanical and degradation properties of polylactic acid. The molecular weight influences the mechanical and degradation properties of PLLA. When the molecular weight of PLLA is relatively low, the tensile strength and flexural strength of PLLA will improve with the increase of molecular weight. When the

molecular weight exceeds a certain value ($\sim 200,000$), its influence is not so significant yet. Almost all degradation experiments can draw the conclusion that PLLA with a higher molecular weight degrades relatively slowly. For PLLA with the same molecular weight, star-shaped structured (more branched chains) PLLA degrade faster than linear structured PLLAs.

Due to PLLA's crystallinity, its mechanical properties are better than that of poly (D, L-lactic acid) (PDLLA), and its mechanical properties can be improved through crystallization. The increasing in crystallinity can improve the tensile strength and elastic modulus of PLLA, but it could contribute to a decrease in elongation at break. PLLA after thermal annealing at an appropriate temperature has higher tensile modulus and flexural modulus. PLLA in the amorphous region is more difficult to be degraded than the PLLA in the crystalline region. Of course, mechanical or degradation properties are also subject to working conditions including temperature, humidity, or enzymes, etc. This issue would be discussed in the specific chapters.

Table 2.2 Infrared spectroscopy (FT-IR) characteristic peaks of PLLA.

Bonds	Type	Wavenumbers (cm^{-1})
C—O—C	symmetric stretching vibration	1100
C—O—C	anti-symmetric stretching vibration	1250
C=O	carbonyl	1750
—CH ₂ —	methylene	2890
—CH ₃	Methyl	2960
O—H	carboxylic acids	3500

2.2.4 Applications of PLLA

PLLA has high strength and renewability and is environmentally friendly [19]. As an aliphatic polyester, PLLA can be completely decomposed under the reaction of microorganisms, water, acid, and alkali in nature and finally produces carbon dioxide and water. Compared with traditional polymer membranes, fibres and their products

themselves are the major application areas of PLAs. As a traditional textile, polylactic acid fibre is used in clothing and home textiles.

In order to fulfil the requirement of tissue engineering scaffolds, electrospinning porous PLLA nanofibres should have interconnected porous structures and high surface area. More ideally, it should also simulate the function of extracellular matrix (ECM) for culturing cells and clinical applications. Enlarging the specific surface area of electrospun porous PLLA nanofibres is a popular topic to be researched and discovered. Moreover, the mechanical performances of electrospun porous PLLA nanofibres are also significant. Regarding the most of reported PLLA nanofibres were amorphous, because of its low crystallization rate and crystallinity during electrospinning processing. The crystallized electrospun porous PLLA nanofibres with good interconnectivity and high specific surface area would have much wider applications.

2.3 Silk Fibroin (SF)

2.3.1 Material background

The source of silk fibroin is a natural filament produced by *Bombyx mori*, a kind of which means silkworm of the mulberry tree in Latin. In China, the application of silk in the field of traditional textiles could be dated back to 4,700 years ago. With the deepening of the structural characteristics and physicochemical properties of silk, nowadays, scholars in the relevant fields extend the research direction of silk from traditional textiles to other fields gradually [20]. The application of RSF materials in biomedicine is a hot topic globally [21].

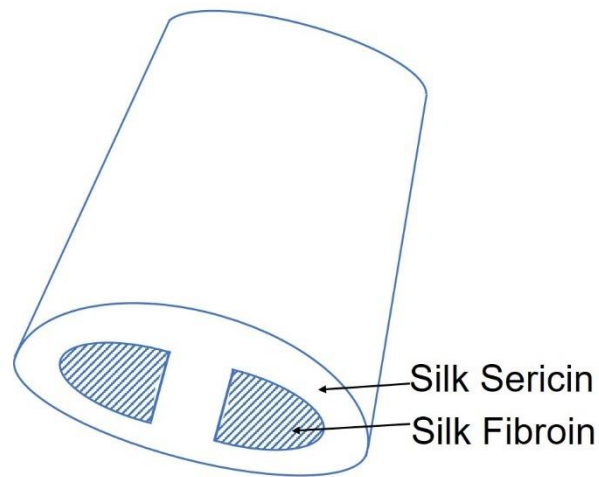


Fig. 2.3 Structure of natural silk fibre.

Natural silk fibre is oval shape. And it consists of two proteins, sericin and fibroin. Sericin is smooth and glossy, which covers two independent fibroin filaments. To obtain pure fibroin, the degumming process is necessary for the raw silk. It mainly consists of about 25% of total sericin protein and 75% of silk fibroin. Sericin, as a binder, fixed two triangular fibroin sections with an average diameter of about $10\mu\text{m}$ and wrapped in together to form a natural silk fibre. Sericin has almost no mechanical properties and is easily soluble in hot water. It is mainly separated from silk fibroin by the degumming process [22]. Natural silk contains mainly hydrogen, carbon, nitrogen, and oxygen, as well as a small amount of silicon, potassium, calcium, iron, copper, and strontium [23].

SF is the main component of natural silk. Its molecular mass is relatively high, and the molecular structure and intermolecular forces are fairly complex. The present theory believes that silk fibroin molecular chains are generally considered to consist of the following three subunits [24]:

- 1) Heavy chain (H-chain), consisting of 5236 amino acid residues, has a mass of 391kDa; 2) The light chain (L-chain), consisting of 266 amino acid residues, has a mass of 28kDa and binds to the H-chain with a disulphide covalent bond; 3) P25 protein, with a mass of 25kDa, is similar in size to the L-chain but has a completely different amino acid composition. It exists as a trace component of SF and is linked to H-chain and L-chain via hydrophobic interactions. The ratio of H-chain, L-chain, and P25 protein in SF are 6:6:1 [25]. The H-chain subunit protein forms an H-L complex with

the L-chain subunit protein, and the P25 protein is linked to six H-L complexes to form the basic unit of silk fibroin.

Silk fibroin is composed of 18 kinds of amino acids, of which glycine (Gly), alanine (Ala) and serine (Ser) account for about 85% w/w. The smaller amino acids of these substituents are arranged into relatively regular segments according to a certain sequence six peptide structure, -(Gly-Ala-Gly-Ala-Gly-Ser)- [26], which is mainly located in the H-chain crystalline region of SF, and the crystalline portion is uniformly distributed in the continuous amorphous region. Other amino acids with larger substituent groups are always located in the amorphous region. As a result, the crystalline region only takes the 37% w/w in fibroin.

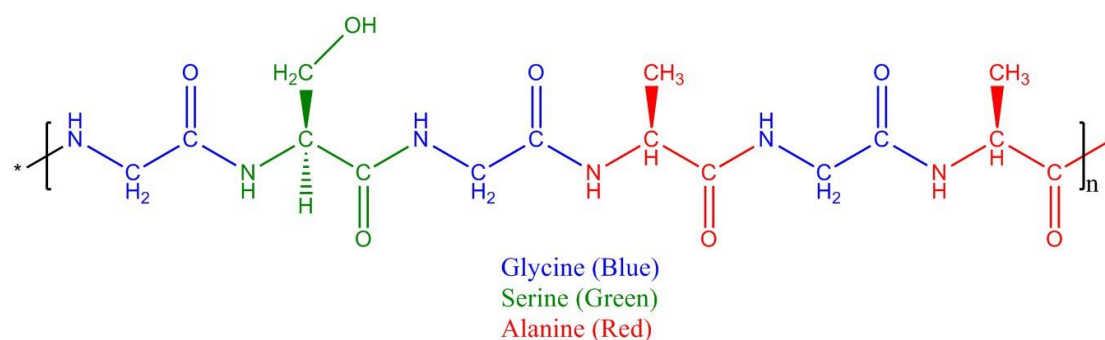


Fig. 2.4 Structure of hydrophobic Crystalline Region of SF.

The secondary structure of a protein refers to the confirmation of the local peptides in the peptide chain. The secondary structure is also the basis of the complex spatial conformation of the protein which is regarded as the tertiary structure of the protein [27]. The secondary structure of silk fibroin is mainly divided into three conformations: random coil, α -helix, and β -sheet. Moreover, the β -sheets are divided into Parallel β -sheet conformations which the N-terminus of all peptides are at the same end (Bent), and Antiparallel β -sheet conformation which the N-terminus of all peptides are alternately arranged in the forward and reverse directions (Linear). Hence the Antiparallel β -sheet is the most stable due to the best assembly between segments and the energy of hydrogen bond between carbonyl and amine is at its lowest level [28].

The aggregated state structure of SF is divided into a crystalline region and an

amorphous region, and the two are alternately distributed. Thus, the crystalline region is uniformly dispersed in a continuous amorphous region. The H-chain passes through both the crystalline region and the amorphous region, while the L-chain exists only in the amorphous region. Crystalline regions are usually divided into Silk I and Silk II. Lotz *et al.* proposed the crystal structure model of SF [29]. Masanobu thought that three-dimensional conformation of Silk I is crank-shaped, which is an intermediate between α -helix and β -sheet. In other words, Silk I conformation is a metastable structure. Marsh proposed a crystal structure model of Silk II, an Antiparallel β -sheet conformation, based on XRD results [30]. Due to the structural instability of Silk I, it can be converted to Silk II structure by certain conditions (alcohol solvents, heat treatments, *et al.*). The highly oriented crystalline portion along the fibre axis gives the silk a high strength, and the non-crystalline region absorbs most of the energy when subjected to stress and makes the silk highly flexible.

2.3.2 Processing and modification

Sericin is irregularly attached to the periphery of SF by scaly granules, accounting for about 25% of silkworm cocoon mass, contains a small amount of wax, carbohydrates, pigments and inorganic components [22]. The secondary structure of sericin is dominated by random coils, supplemented by partial β -sheet, and contains almost no α -helix conformation. Moreover, the inner sericin close to silk fibroin contains β -sheet conformations higher than the outer side of sericin. Under the influence of environmental conditions, the outer layer of sericin can be irreversibly converted to β -sheet conformation from some random coils. The sericin of silk is coated on the outside of SF and covered with four layers. Since the water solubility of the sericin coating layer gradually weakens from the outside to the inside, the degree of crystallinity increases in turn, and thus the outer layer of sericin is the easiest to remove.

In normal circumstances, the use of acid, alkali, soap, high temperature and high pressure and enzyme treatment under certain conditions can achieve the purpose of removing sericin. However, improper degumming treatment methods will cause the

decrease or change of SF's material properties, which will affect the physical and chemical performances of SF for further applications. The common silk degumming methods include sodium carbonate solution degumming, water bath boiling degumming, high temperature and pressure degumming, soap, and alkali degumming, *et al* [31].

Because of a large quantity of hydrogen bonds exist in silk, SF performances a stable physicochemical property. Therefore, after sericin degumming, the precondition of reprocessing fibroin is dissolution. This processing for SF dissolution goes through two stages. Solvent molecules penetrate the interior of fibroin structure at first to make fibroin swelled. And then fibroin molecules are evenly dispersed in the solvent, forming an entire solution of fibroin molecularly dispersed homogeneous system. Researchers have developed some methods to dissolve silk fibroin. These methods could be concluded into three kinds of mechanism.

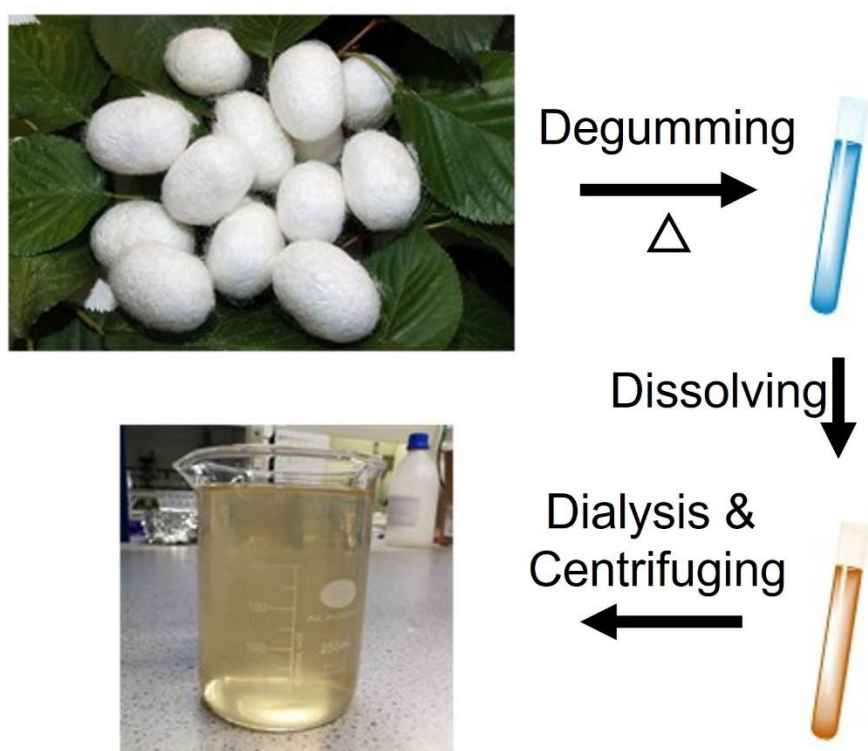


Fig. 2.5 Preparing protocols of silk fibroin solution.

The first mechanism is related to inorganic acid system and cuprammonium

solution system that could be dated back to the last century. Strong acids are mainly used to dissolve fibroin in the early studies. Prior to the work of Camille [32], inorganic strong acids such as sulfuric acid were used under the concentration of 25-75 vol% to dissolve fibroin at a low temperature. Ishizaka *et al.* hydrolysed silk fibroin by orthophosphoric acid solution and then ammonium sulfate and sodium sulfate solution were applied when fibroin solution was made into artificial fibres by coagulation bath wet spinning method [33]. However, it was found that the use of strong acid to dissolve silk would degrade SF far seriously. Therefore, few researchers choose to use strong acid as a solvent to dissolve SF now. Gustavus used cuprammonia solutions to dissolve fibroins and spun regenerated protein fibres in 1931, but cuprammonia solvents cause serious degradation of fibroin molecules either [34].

The second dissolving method is using neutral salt dissolution systems. Subsequent studies found that high concentrations of neutral salt solution, e.g., halogen, nitrated thiocyanate of calcium, magnesium, lithium, zinc, can dissolve SF. Yazawa *et al.* used high concentrations of magnesium nitrate solutions to dissolve SF followed by dialysis, concentrated in a saturated ammonium sulfate solution coagulation bath wet spinning artificial silk fibre. Lock reported that a solution of SF was obtained by dissolving silk fibroin with 90 wt% formic acid and 10% w/w lithium chloride as solvent to obtain an RSF solution with a concentration of 15.3 wt% [35]. Matsumoto *et al.* obtained regenerated silk fibroin solution with LiBr·H₂O-EtOH-H₂O as solvent [36], Hudson dissolved fibroin with Ca (NO₃)₂-CH₃OH [37], and Park *et al.* used CaCl₂-EtOH-H₂O ternary solvent to dissolve SF [38]. Among many supersaturated salt solutions, CaCl₂-EtOH-H₂O ternary solution and LiBr aqueous solution are the most used two silk regeneration systems, which have good dissolving ability and dissolution effect and are both economic and convenience.

The third dissolving method relays on the ionic liquid dissolution system. The rise of ionic liquid provides a new choice for dissolving fibroin and its regeneration issues [39]. In 2004, Philips *et al.* proposed the ionic liquid cation and anion structure on dissolving SF. The study found that when the branches of the cation are shorter, chloride ions liquid performs well on the SF dissolving. The mechanism is that anions form

hydrogen bonds with fibroin macromolecules and destroy the hydrogen bonds of protein inter macromolecules to dissolve fibroin. The more anions form hydrogen bonding, the stronger the dissolving ability to fibroin, such as 1-ethyl-3-methylimidazolium chloride can dissolve silk at 100°C. More researchers began to study the ionic liquid dissolved silk protein [40]. Zhang found ionic liquids such as 1-butyl-3-methylimidazolium chloride and 1-hexyl-3-methylimidazolium chloride can well dissolve SF.

Furthermore, Zuo proposed salt-formic acid solvent system is a low concentration solvent [41]. The addition of low concentrations (1 wt%) of calcium chloride to formic acid dissolves the silk fibroin at room temperature and opens its internal β -sheet crystal structure. The dissolution process can be controlled at the level of nanofibrils, rather than the conventional dissolving fibroin to molecules level. Compared with the traditional solvents, this dissolution method has the characteristics of low salt concentration, rapid dissolution under normal temperature conditions and dissolution control at the level of nanofibrils. The preservation of the nanofibrillar structure is very beneficial for preparing high-performance RSF materials. Since the room temperature ionic liquid has the advantages of strong polarity, non-volatility, small toxicity, strong solubility, and easy recovery, it is a promising green solvent with basically no waste during the dissolution process and avoids the traditional dissolving process pollution problem.

Due to SF expansion caused by water molecules infiltration is insufficient to destroy the internal stability of the silk crystal structure, SF will swell in the water. When calcium chloride is added to the water, the water molecules combine with the salt ions firstly and requiring higher concentrations of neutral salt or heating conditions to dissolve the fibroin. When formic acid is used instead of water, formic acid is preferentially infiltrated into the interior of SF to expand the volume of silk fibroin. The expanded interior space of fibroin increases, which is favourable for salt ions to enter and interact with fibroin molecules. The strong polar ions in the solvent produce strong hydration, which is beneficial to salt ions and interact with fibroin molecules. Strong polar ions in the solvent produce strong hydration, a large number of carboxyl groups

adsorbed on the surface of fibroin, weakening the van der Waals forces between the molecular chains of fibroin and intermolecular hydrogen bonds, hence the fibroin peptide chains become active enough to destroy the intramolecular or intermolecular hydrogen bonds in SF molecules and to dissolve SF fibres to nanofibrillar levels. In addition, the salt ions and the polar amino acid residues in SF molecules, such as histidine and serine, coordinate to form complexes that destroy the intermolecular hydrogen bonds. As the dissolution continues, the crystal structure of the interior of SF fibres is destroyed.

2.3.3 Properties of silk fibroin molecular

X-ray diffraction (XRD) and X-ray photoelectron spectroscopy (XPS) are two vital technologies to observe and analysis macromolecular materials.

XRD is based on the theory of the coherent scattering of X-rays. Its application is under the Bragg's equation ($2d \times \sin \theta = n\lambda$), Crystal field theory and reciprocal lattice. Specifically, the diffraction could observe the relationship between chemical bond and the structure or properties for SF [42]. The Table 2.3 & 2.4 demonstrated the d-spacing and 2θ of silk fibroin from a copper target as the mainstream radiation [43]. The Cu K α wavelength is 1.5418 Å.

Table 2.3 The diffraction peak of Silk I [43].

d (Å)	2θ (°)	Intensity
7.25	12.2	Medium Strong
4.50	19.7	Strong
3.60	24.7	Medium
3.16	28.2	Medium
2.77	32.3	Weak
2.44	36.8	Medium Weak
2.25	40.1	Medium Weak

Table 2.4 The diffraction peak of Silk II [43].

d (Å)	2θ (°)	Intensity	bonding
9.7	9.1	Medium Strong	Hydrogen-bonded interchain
4.69	18.9	Medium Strong	
4.30	20.7	very Strong	Intra-hydrogen-bonded β-sheet spacing
3.67	24.3	Weak	
2.27	39.7	Weak	

The principle of XPS is to use X-rays to irradiate the sample and to stimulate the emission of the inner electrons or valence electrons of atoms or molecules. Electrons stimulated by photons are called photoelectrons. To obtain sample information, photoelectron spectrogram could be figured as the abscissa axis is photoelectron kinetic energy, and the ordinate axis is relative intensity (pulse/s) via measuring the photoelectron energy. Since XPS is widely used for chemical analysis, it is also called Electron Spectroscopy for Chemical Analysis.

The main applications are the qualitative analysis of the elements. All elements except H and He can be identified based on the position of the characteristic line appearing in the energy spectrum. Specifically, XPS could be used for analyzing the surface and structure of SF, which including the surface of the chemical composition or elemental composition of SF and measuring of the chemical shift of the inner electron binding energy provides information on chemical bonding and charge distribution of SF accurately.

Fourier transform infrared spectroscopy (FT-IR) is the primary means of investigating the secondary structure of proteins. Since the 1980s, the study of protein secondary structure by infrared spectroscopy has entered a quantitative stage. Therefore, this approach can analyse the conformational characteristics, the conformational transition process, and the factors that affect the conformational transition of fibroin. At the same time, it also has the advantages of easy operation, high wavelength accuracy, good resolution, high scanning speed, and high sensitivity.

As a protein polymer, the secondary structure of silk fibroin is closely related to the different types of hydrogen bonds formed in its molecule. FT-IR is an excellent resort for the study of hydrogen bonds. It can obtain infrared spectra of almost all biological substances under various environmental conditions. In addition, FTIR also has advantages such as less sample consumption, unaffected by the molecular weight of protein, no influence of light scattering and fluorescence, and the possibility of retention for kinetic studies.

In general, proteins contain a variety of different secondary structures, and each characteristic absorption peaks of a protein are usually formed by the stretching vibration absorption sub-bands that represent the α -helix, β -sheets, and random coil structure components. Because the inherent width of each sub-band is less than the resolution of the instrument, it is difficult for conventional spectral techniques to separate them.

In 1950, Elliott proposed a hypothesis that the peak of the infrared amide with a band of 1660-1650 cm^{-1} belonged to the α -helix conformation, and the peak of 1640-1630 cm^{-1} belonged to the β -sheet conformation. For a long time, FT-IR conformational research on proteins has basically been a superficial and qualitative method. The Fourier deconvolution technique offers the possibility of obtaining quantitative information on the protein conformation from the infrared spectrum. In 1983, Susi and Byler first applied FT-IR's second derivative theory to study secondary structure. In 1986, they applied the deconvolution method to secondary structure analysis, making an infrared analysis of protein secondary structure into the quantification stage. The application of the second derivative and deconvolution method has improved the resolution of the infrared spectrum and thus can be effectively used for protein thermal denaturation, solvent denaturation, chemical deformation, chemical modification, and minor conformational changes resulting from the substitution of individual amino acid residues. In other words, FT-IR became an important tool to reveal quantitative changes in protein conformation now.

Table 2.5 Infrared spectroscopy characteristic absorption peaks of proteins.

Absorption bands	Wavenumber (cm ⁻¹)	Random Coil	β-sheet
A	~3300		
B	~3100		
I	1690-1660	1661-1650	1640-1625
II	1575-1480	1531-1545	1525-1515
III	1301-1229	1245-1220	1270-1245
IV	970-895		
V	800-640	632-620	700-690
VI	606-537		
VII	200~		

2.3.4 Applications of silk fibroin

The application of silk fashions could be traced back to thousands of years ago. However, the silk has been considered as biomaterials or other kinds of advanced materials since 1990s. Bioactive tissue engineering material is one of the most emerging subjects in this century, contents varieties of knowledge not only limit to molecular biology but also material engineering. Tissue engineering subject tries to heal or replace human organs and tissues, if injured, by means of certain scaffolds. The main function of silk as biomaterial, regenerated silk fibroin scaffold, is the enhancement and support to the organs and assistance of tissue reconstruction [27].

Applied as a tissue engineering material, SF normally was dissolved and proceed into fibres, sponges, gels, microspheres, and films. In recent years, silk fibroin has been applied to 3D tissue engineering scaffolds, but there is a contradiction between its aperture size and mechanical properties. In terms of vascular scaffolds, the porous size of scaffolds has a significant effect on the long-term implant efficiency, while the cellular metabolic efficiency is also related to the scaffold pore size [44].

In recent years, with the maturity and market promotion of 5G communication technology, the concept of the Internet of Things has received extensive attention from governments, researchers, and investors [45]. Energy harvesting and storage devices or

smart wearable sensors using silk fibroin as raw materials are developing rapidly. Compared with traditional synthetic polymers or silicon-based materials, silk fibroin is easily degraded. So, it has significant advantages for contact with the human body, especially implantable sensors. It should be noted that the research on silk fibroin wearable flexible device is based on the exploration of silk fibroin biomaterials in the past few decades. Because silk fibroin biomaterials have the advantages of easy processing, high yield, biocompatibility, controllable biodegradability, and optical transparency, which are the key advantages of silk fibroin for flexible wearable sensors.

2.4 Theory and Mechanism Development of Electrospun Porous Fibres

As the primary parameter of electrospun PLLA fibres, solvent selection distinguishes the different mechanisms to form porous structures. It has been introduced in the fabrication strategies section that the relationship between solvents and macromolecules not only affects the formation of fibres, but also has a significant impact on the morphology of electrospun fibres.

How to summarize and summarize the formation mechanism of electrospinning porous fibres. This is still a stage for the frontier researchers to reach a consensus. In section, I tried to summarize some theoretical developments of porous formation in recent years, among which electrospun polymer fibres, especially PLLA, are the main research objectives.

2.4.1 Hildebrand and Hansen solubility parameters

Since the molecular weight between the polymer and the solvent often has a gap of multiple orders of magnitude, the molecular motion speeds of these two phases are also significantly different. In other words, solvent molecules can penetrate into the polymer relatively quickly, while the diffusion of polymers into the solvent is much

slower. Therefore, the polymer/solvent dissolution process of the polymer has to go through two stages. First, the solvent molecules penetrate into the polymer to expand the volume of the polymer, which is called swelling. Then, the polymer is gradually uniformly dispersed in the solvent to form a homogeneous system in which completely dissolved molecules are dispersed. For some cross-linked polymers, swelling also occurs when in contact with solvents. However, because of the bondage of cross-linking, the solvent can no longer break up the cross-linked molecules. In this case, the relationship between the solvent and the polymer can only remain in the swelling stage and will not dissolve.

For further quantitative discussion, the dissolution is a process of which solute molecules and solvent molecules are mixed with each other. Under constant temperature and constant pressure, the necessary condition for this process to proceed spontaneously is the change of Gibbs free energy $\Delta F_M < 0$, by the standard thermodynamic equation (2.1) [46]:

$$\Delta F_M = \Delta H_M - T\Delta S_M < 0 \quad (2.1)$$

Where T is the dissolving temperature (Kelvin), ΔS_M is entropy of mixing, which means the change in entropy of polymer and solvent when they are mixed. Because in the process of dissolution, the arrangement of molecules tends to be more chaotic, and the change in entropy would be increased, which means $\Delta S_M > 0$. Therefore, the sign of ΔF_M depends on the sign and magnitude of ΔH_M , the enthalpy of mixing.

In the case of a polar polymer in a polar solvent, the dissolution is exothermic ($\Delta H_M < 0$) due to the strong interaction between the polymer and the solvent molecule. It also means that the Gibbs free energy of the system is reduced ($\Delta F_M < 0$), so the dissolution process will happen spontaneously. For non-polar polymers, the dissolution process is generally endothermic ($\Delta H_M > 0$), so only by increasing the temperature (T) or reducing the heat of mixing (ΔH_M) can dissolving process happen spontaneously in the system.

As for the heat of mixing (ΔH_M) of the non-polar polymer and the solvent are mixed, it is necessary to use the Hildebrand solubility formula (2.2) of small molecules to calculate:

$$\Delta H_M = V_M \phi_1 \phi_2 (\delta_1 - \delta_2)^2 \quad (2.2)$$

Where V_M molar mixing volume of two molecules, and ϕ is volume fraction. The δ is called solubility parameter whose dimension is $J^{1/2} \cdot m^{-3/2}$ or $Cal^{1/2} \cdot cm^{-3/2}$. According to formula (2.2), the ΔH_M of system depends on the δ_2 of the two substances. If Hildebrand solubility parameters (δ_1 and δ_2) are closer, then ΔH_M is smaller, the two phases can dissolve each other and vice versa.

As an improved quantitative strategy for “like dissolves like”, solubility parameter is a widely acknowledged theoretical model for evaluating the specific solubility between polar molecular polymers and solvents [47]. Hildebrand solubility parameters can be considered as the vector sum of these three variables. However, the Hildebrand solubility formula is only applicable to the mixing of non-polar solutes and solvents. It is only a quantification of the empirical law of "like dissolves like".

Even just based on instinct, the solvent-polymer solute relationship cannot be described accurately and convincing relying on a parameter (δ). As a further development of Hildebrand theory, the Hansen solubility parameter is more complex but effective [47]. Hansen solubility parameters is a criterion that composed of three variables including molecular dispersion, polar and hydrogen-bonding [48]. It could be expressed by the equation:

$$\delta^2 = \delta_D^2 + \delta_P^2 + \delta_H^2 \quad (2.3)$$

Where the δ_D is the parameter for dispersion, the δ_P is the parameter for polar, and the δ_H is the parameter for hydrogen-bonding. These three parameters are used to locate the vector points in a three-dimensional space (i.e., Hansen space in Figure 2.6) [49].

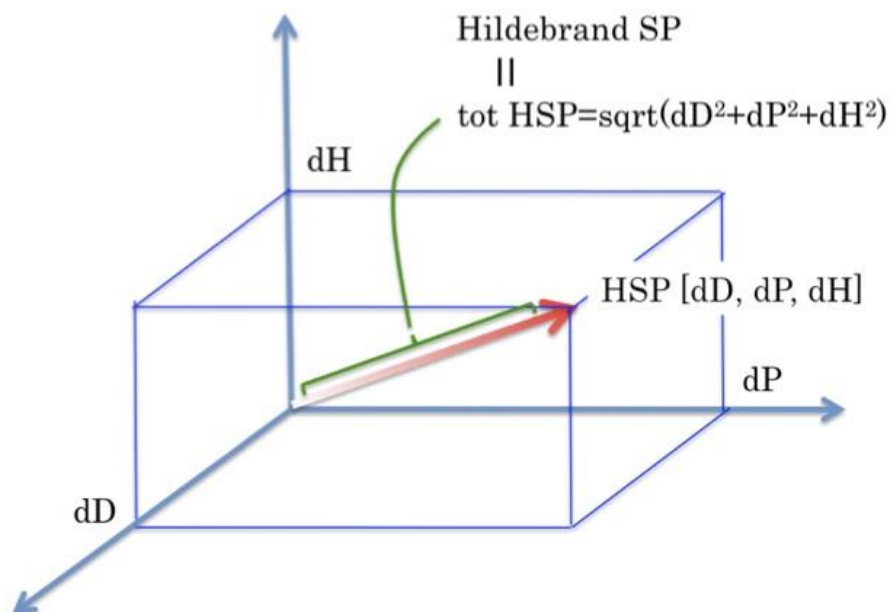


Fig. 2.6 The geometric expression of the Hansen and Hildebrand solubility parameters in the Hansen space [49].

Based on the two vectors which stands for two molecules' Hansen solubility parameters, their position and distance in the space could indicate their relative solubility properties. For comparison, the concept of Hansen solubility is based on the relative parameters obtained by comparing two or more different molecules, while Hildebrand solubility is an absolute value. Based on the geometric meaning in the Figure 2.6, Hansen solubility is the distance between two vectors in the Hansen space, while Hildebrand solubility is just the difference in the absolute value of the length of the two vectors.

2.4.2 Flory-Huggins theory

After the polymer dissolved in the solvent, the solute/solvent system can be quantitatively analyzed throughout Flory-Huggins theory which was established by Paul J. Flory & Maurice L. Huggins [50,51]. Flory-Huggins theory is a molecular thermodynamic model to characterize the system of macromolecule solution. This theory regarded the polymer molecules as the chains of segments, which would be

equivalent in size to a solvent molecule. In other words, the interactions between solute molecules, solvent molecules, and solute/solvent molecules in the solution can be analyzed equally. In such an ideal solution, the Gibbs free energy of mixing in (Eq 2.1) can be further expressed as:

$$\Delta F_M^i = \Delta H_M^i - T\Delta S_M^i = kT(N_1 \ln X_1 + N_2 \ln X_2) \quad (2.4)$$

Where the N is the number of molecules, X is the mole fraction, the subscripts 1 & 2 stand for solvent and solute respectively, and k is the Boltzmann constant. The major significance of Flory-Huggins theory for this study is that a simulated lattice model. This lattice model could interpret the phase separation happened upon the temperature and solute/solution composition changed. It should be recognized that Flory-Huggins theory could guide the fabrication strategy to best the best parameter of electrospun porous fibres.

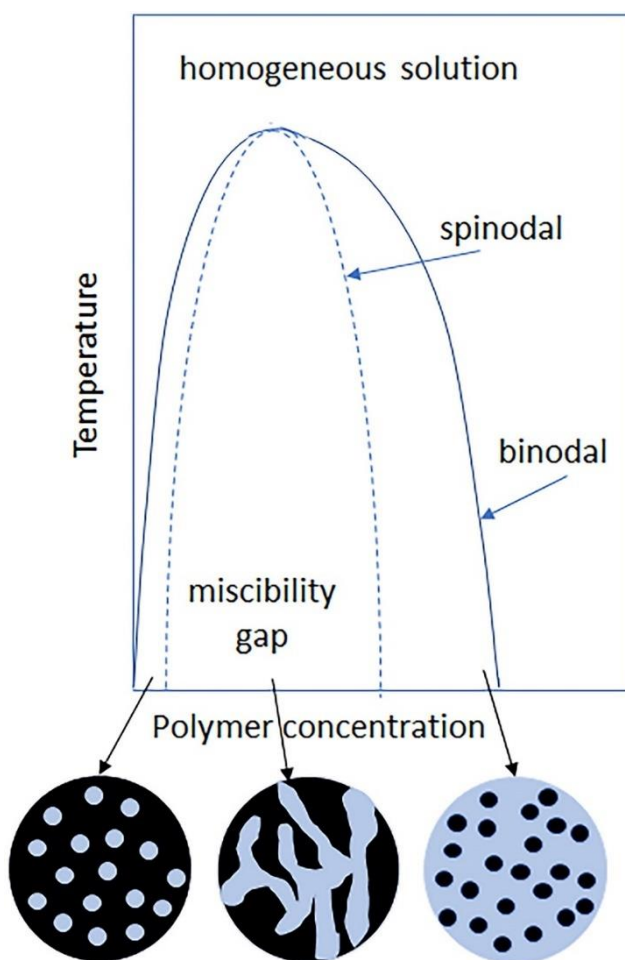


Fig. 2.7 The isothermal diagram for phase separation scenarios in a polymer/solvent

binary phase system [52].

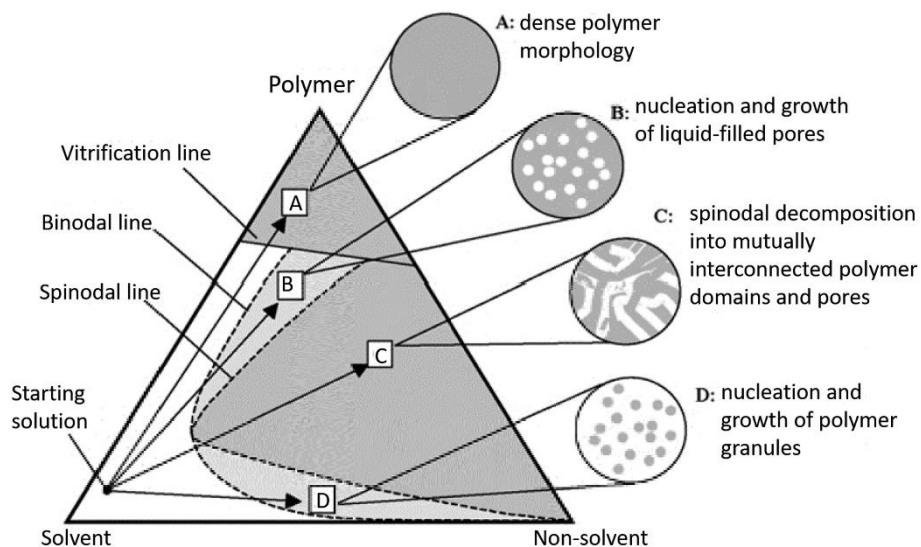


Fig. 2.8 The isothermal diagram for phase separation scenarios in a polymer, solvent and non-solvent ternary phase system which illustrates four hypothetical formations and morphologies [53].

Figures 2.7 & 2.8 show two typical scenarios. Figure 2.7 is the solute/solution binary phase system. In this binary system, the nucleation and growth changed with the increasing of polymer concentration. Figure 2.8 is the solute/solution/non-solution ternary phase system. In this ternary system, there are four coagulation routes which have been presented in the figure with details.

2.4.3 Breath figure mechanism

The breath figure mechanism should be mentioned in advance, due to the two reasons. Firstly, breath figure has been widely used in conventional polymer casting film fabrication. Secondly, breath figure is a typical applied technology of Flory-Huggins theory. In the casting process of polymer film, relatively high humidity and the use of volatile solvents can contribute to the formation of an ordered array of pores on the surface of the film. Frankly speaking, breath figure mechanism is similar with a ordinary phenomenon, i.e., the water droplets condensation on cold interface from the

water vapour in the air.

Specific to the application of breath figure mechanism in electrospinning technology. Combining the phase separation diagrams in Figures 2.7 & 2.8 and Flory-Huggins theory, it is not difficult to predict that the selection of volatile solvents and the temperature decrease during the spinning process are two necessary conditions for obtaining phase separation of electrospinning polymer fibres. Moreover, in order to avoid the solvent remained on the electrospinning fibre affecting the water condensation process, the electrospinning solvent should be hydrophobic and water immiscible. More specifically, DCM, chloroform, and tetrahydrofuran are good volatile solvents for PLLA. As Figure 2.9 c demonstrated, the water vapour will condense on the interface of polymer fibres if the evaporation rate of solvent is too fast so that the temperature of fibres' surface decrease. These condensed water droplets could occupy certain spaces on the wet fibres. The pores then finally formed after all solvent and condensed water evaporated.

Figure 2.9 demonstrates the pores on the surface of conventional casting film and electrospun fibre. Both of them were formed through breath figure mechanism. These two porous structures are highly similar: similar round shape and laid on the polymer surface. The above two characteristics are also the limitation breath figure mechanism. In other words, the porous structures formed by the breath figure mechanism are monotonous and superficial.

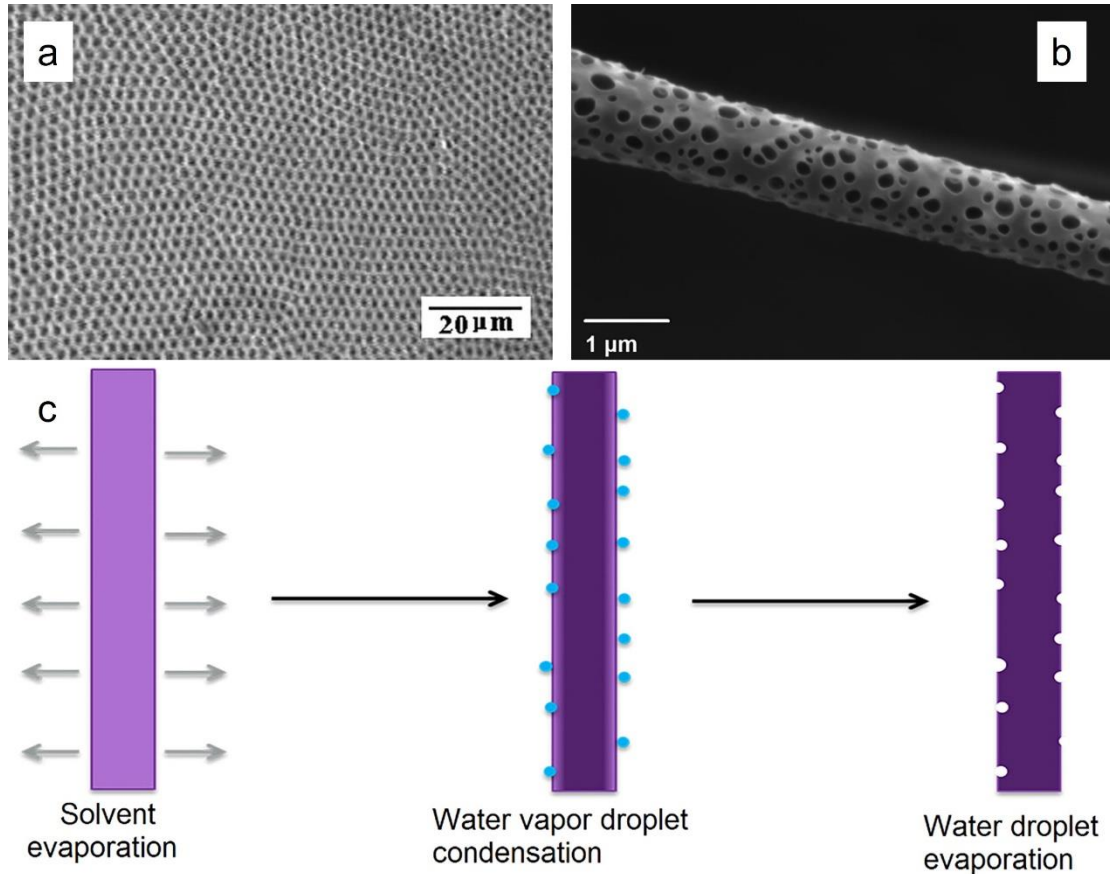


Fig. 2.9 (a) The porous structure on the casting film formed by breath figure mechanism [54]. (b, c) The porous structure on the electrospun PLA fibre formed by breath figure mechanism and the diagram of the pores forming process [16].

2.4.4 Phase separation mechanism

The occurrence of phase separation is also caused by many reasons during and after the electrospinning process. Among them, the scenario most close to the breath figure mechanism should be vapour-induced phase separation (VIPS). Vapour-induced phase separation can explain the formation mechanism of pores in a single solvent electrospinning system and involves with water vapour. While the polymer jet is stretched at a high speed within a high-voltage electrostatic field, the solvent is volatilized rapidly. Meanwhile, the jet is phase-separated in a short time to form solvent-rich phases and polymer-rich phases. Finally, the polymer enrichment phases gradually solidify to become the overall skeleton of the fibres while the solvent

enrichment phases form voids in the fibres. Oppositely, VIPS is contributed by low evaporated, water miscible, and hydrophilic solvent, while it would be highly volatile, hydrophobic, and water immiscible for breath figure mechanism.

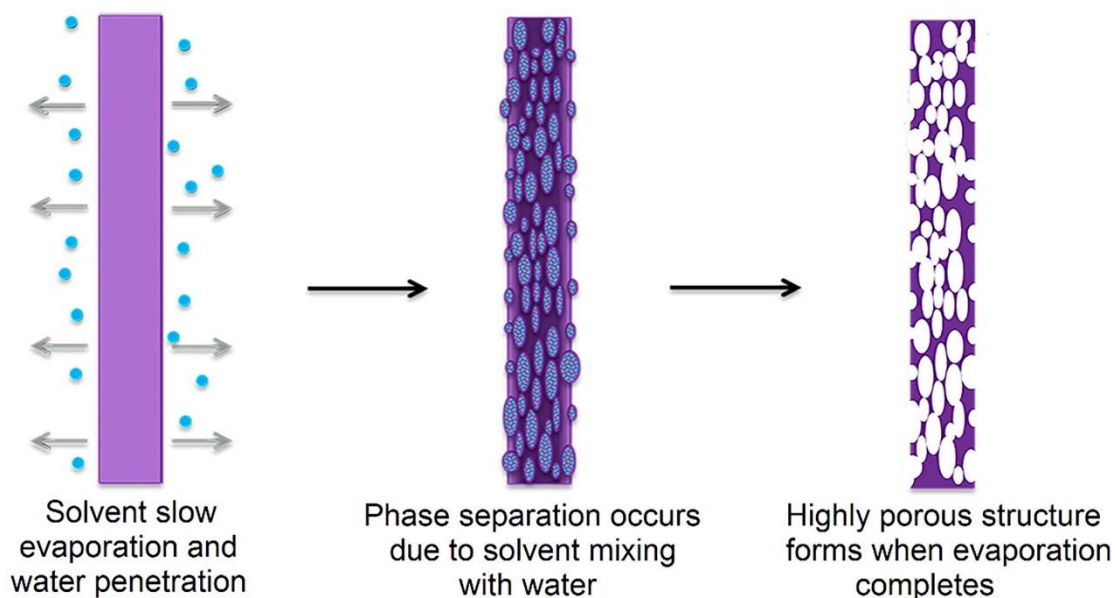


Fig. 2.10 The diagram of the pores forming process due to the vapour-induced phase separation mechanism [16].

For a dual-solvent system with one good solvent and one nonsolvent or bad solvent of the polymer, the nonsolvent induced phase separation (NIPS) is the main reason to generate porous structures, especially when the good solvent has a higher evaporation rate than that of the nonsolvent [15]. Fast evaporation of a good solvent causes the phase separation, and small nonsolvent droplets are trapped inside polymer matrixes. Some small pores are left after nonsolvent droplets have completely evaporated. In addition to solvents, environmental factors can also be controlled to produce the porous structure during electrospinning. For example, tiny water droplets attach on the surface of polymer fibres in a high humidity environment and leave small round depressions after the fibres have totally dried [55]. For contributing to the nonsolvent induced phase separation, the vapour pressures of solvent and nonsolvent should have significant difference. The solvent should be high volatile and the nonsolvent should be low volatile. By adjusting the appropriate parameters, the nonsolvent can remain in the fibre

for a period of time, occupying some space. After the nonsolvent evaporated, some pores are formed in the space left on the fibre.

Thermally induced phase separation (TIPS) would only happen when the temperature of fibre's surface decrease due to the evaporation of solvent [56]. Then polymer-rich and solvent-rich regions would lead to the porous structure after the completely evaporation of solvent.

2.4.5 Solvent induced crystallization

Though the efforts of these researchers, some porous fibres have been fabricated with more porous structures and higher surface areas than solid fibres. However, most of these pores are either too big or only distributed on the fibre surface, not throughout the whole fibre. Hence, the surface area of these porous fibres has only a limited improvement. Compared with breath figure and phase separation mechanisms, solvent induced re-crystallization is a relatively new strategy to prepare electrospun porous fibres.

Crystallization is one of the major physical change of polymers. The extent of crystallization of polymers would be decided by many properties of polymers including molecular weight, melting point, and cooling rate [46]. The experiments have also demonstrated higher crystallinity the polymer is, the higher density it will be. It also has been found that most of crystalline polymers contains both crystalline and amorphous regions. In other words, these of crystalline polymers are *de facto* semi-crystalline state. When the crystallinity of polymer elevated, various properties of polymer would change. The optical property of polymer will change from transparent to opaque due to the orientation of the molecular chains. The mechanical property of polymer will be enhanced though crystallization, too.

The most of macromolecular electrospun fibres are in a low-crystalline or non-crystalline state [57]. There are many factors could induce the crystallization of polymers, including theorem, photo, forces, and solvents. Therefore, organic solvent system induced re-crystallization of macromolecules is an option to modify fibre's

hierarchical porous surface morphology after electrospinning.

Specifically, Naga *et al.* have proved that PLLA could be induced to elevate its degree of crystallinity and crystallized into α crystals by some organic solvents including acetone, diethyl ether, ethyl acetate, methanol, , toluene, and xylene [58,59]. Gao et al. further manipulated the surface morphology of PLA from spherulite to shish-kebab and bamboo-cage-like structure by solvent induced crystallization [60]. Gao et al. also proposed the mechanism of crystallization, which the acetone dissolved or destroyed the fibril interface of polymer. Then, the solvent would evaporate and spherulites would grow on the surface of polymer when the polymer and solvent were separated.

The recent published systematic research has successfully implemented this theory on PLLA fibres [61]. Thus, most of electrospun polymer materials can be induced re-crystallization by solvents [62]. The solvent that induces polymer recrystallization needs to swell the polymer fibre but cannot dissolve the polymer. It means that this solvent cannot be a good solvent for the polymer, but it can significantly increase the crystallinity of the polymer. Combining with the solubility parameters introduced in Section 2.4.1, the solubility of solvent should not too close between solvent and polymer. But if their parameter could keep the dissolve do not happen but the solvent/solute system can restrict the Tg of polymer to under the environmental temperature, so that it will be benefit for crystallization. DCM and chloroform have too good solubility parameters for PLLA so that their dissolution interaction surpluses the solvent induced influence for PLLA. Acetone is the most suitable solution because it rearrange of the PLLA molecular chains wins the competition with its dissolution of PLLA.

In view of the dissolution characteristics of polymer, the careful selection of solvent systems to ensure that the polymer swells rather than dissolves is the key to the successful fabrication of electrospun porous fibres. The selected solvent systems would enter recycled fibre interior where the NIPS mechanism formed during the electrospinning.

2.5 Applications of Electrospun Porous Fibres

The applications of electrospinning are wide and complex. In the past decade (2011-2020), the main applications of electrospinning materials that have been developed include: air filtration; liquid filtration; oil-water separation; super-hydrophobic interface for self-cleaning; waterproof and moisture-permeable interface; adsorption and catalysis; biomedical engineering and biochemical separation; optical or mechanical sensors; energy storage and conversion materials; and thermal insulation materials. Regarding the major works presented in this thesis, this section discusses some previous studies about air filtration and bioengineering electrospinning materials. Furthermore, it also introduces some hot multidisciplinary research areas combining electrospinning with other chemical and electronic science and engineering subjects.

2.5.1 Environmental protection and sustainable development goals

Electrospun fibrous materials for filtering air pollutants [63–65] and wastewater [66] have been studied widely because these membranes have high porosity and interconnectivity. The advantages of electrospinning porous fibres for air filtration materials are mainly due to these fibres have relatively small fibre diameter and high specific surface area. Benefiting from relatively small pore size and high porosity, electrospun fibrous membranes are potentially more effective to filtration and adsorption of solid pollutant particles. The nanofibrous membrane prepared by the electrospinning technology has the characteristics of good fibre uniformity, controllable pore size distribution, and adjustable hierarchical structure [67]. Therefore, different polymer raw materials can be selected according to actual use environment requirements during the manufacturing process of electrospinning, to prepare air filtration materials with high filtration efficiency and low air pressure drop for solid particles of different sizes. Obviously, electrospun nano-fibrous membrane is not the only solution for air pollution control. The followed Table 2.6 summarizes and compares the current mainstream technology routes of air filtration.

For evaluating the filtration quality of fibrous filters, some parameters should be taken into consideration. First, filtration efficiency refers to the ratio of the volume of particles captured by the fibrous filter to the volume of particles in the upstream dusty gas when the upstream dust-containing gas passes through the fibrous filter. Second, the air pressure drop refers to the gas pressure difference between the upstream air inflow side and the downstream air outflow side of the fibrous filter under the rated air volume. Combining the filtration efficiency and the air pressure drop, the quality factor could be obtained to express comprehensive quality of the fibrous filter. Dust holding capacity is also a key parameter of the fibrous filters. It refers as the total mass of the experimental dust volume collected by the fibrous filter from the initial resistance to the final resistance under the rated air volume [68]. The greater the dust holding capacity, the longer the service life of the filter material.

The mechanism of electrospun fibres to filter air particles or aerosols includes physical interception, diffusion effect [69], inertance, gravity [70], and electret charge effect [71]. When the electrospun fibres sacked up as fibrous membrane, the whole membrane filters air particles or aerosols on its surface or interior, where depends on the pore size and the particle size [72].

The advantage of hierarchy structure on electrospun fibres is elevating the roughness of the fibres' surface. Consequently, the specific surface area, pore volume, and porosity could be improved. For aerosol filtration application, the possibility of interception or adhesion could be further increased. Under this circumstance, the capturing mechanisms of aerosol particles by the fibrous filters are synergy between interception and diffusion [73].

Table 2.6 The comparison of current mainstream air filtration devices fabrication strategies.

Technology roadmap	Electrostatic precipitator	Phase separation casting film [74]	Thermoforming membrane	Nuclear track membrane [75]	Fibrous membranes			
					Conventional non-woven fibres	Melt blown electret fibres	Glass fibres	Electrospun fibres ☆
Advantages	Efficient in filtration and energy consumption	Small pore size; and facile fabrication	Thin thickness; small pore size; high porosity.	Compact, uniform, and straight channels.	Highly isotropy stacked fibres	Highly isotropy stacked fibres	Small fibre diameter; low stacking density	Small and uniform fibre diameter and high porosity
Disadvantages	Producing ozone; short service life;	High pressure drop, and consequent energy consumption	Low loading volume; pressure drop increasing sharply after applied	Expensive and high pressure drop	Difficult to minimize fibre diameters	Unstable due to the low charge potential well.	Brittle and easy to break	Poor mechanical compared with other fibrous filters.
Filtration mechanism	The force induced by electrostatic charge impeding through a gas flowing unit.	Physical trap and interception.	Physical trap and interception.	Physical trap and interception.	Physical trap and interception.	The electret charge carries out electrostatic adhesion on particulates.	Physical trap and interception.	Physical interception and electret charge adhesion.

2.5.2 From electrospun fibre-based biomaterials to wearable sensors

The industrialization and promotion of Internet of Things (IoT) technologies are in the ascendant with the successive introduction of 5G telecommunication infrastructure plans in major industrial countries in the world [76]. Smart wearable devices are important IoT ports for human-machine interfaces. Since smart wearable devices need to be worn or even implanted into the human body for a long time, they generally have the characteristics of traditional biomaterials such as mechanics, biodegradability, and biocompatibility. Therefore, there is an inseparable relationship between the research of flexible smart wearable materials and biomaterials.

Wearable sensors produced from electrospun fibres or fibrous membranes mainly include sensors for mechanics, gas, and humidity. Mechanical sensors are the most mainstream, and the subdivisions include pressure sensors, strain sensors, and sensors that collect sound or other human body parameters through vibration.

Chapter 3: Materials & Experimental Methods

3.1 Materials

PLLA pellets used in the whole project was obtained from PURAC Biochem BV. (Corbion, The Netherlands), which is a subsidiary of TOTAL S.A. (France). The specific product number of PLLA is PL 65. The average molecular weight of this kind of PLLA is 1,430,000 g/mol. Raw *bombyx mori* silk was supplied by Shengzhou Xiehe Silk, Shaoxing Zhejiang, China.

DCM ($\geq 99.9\%$), DMF ($\geq 99.8\%$), Phosphate buffered saline (PBS), Dulbecco's modified eagle medium (DMEM), and diamidino-2-phenylindole (DAPI) fluorescent stain were purchased from Sigma-Aldrich, Co., MO USA. Acetone ($\geq 99.7\%$) was purchased from VWR, LLC., PA USA. Ethanol (99%, Alfa Aesar), sodium carbonate (99.8%, Alfa Aesar), LiBr (99%, Alfa Aesar) and Alamar blue cell viability reagent (Invitrogen) were purchased from Thermo Fisher, USA. A7r5 rat smooth muscle cell (SMC) line was purchased as CRL-1444 from ATCC, USA.

3.2 Experimental instruments and methods

3.2.1 Preparation of PLLA/DCM/DMF spinning solution

The PLLA pellets should be stored in the 4°C refrigerator and put into 60°C oven for 4h before further use. The weighted PLLA was slowly added to DCM at the certain ratios. The PLLA/DCM two phase solution was heated by a hotplate stirrer at 50°C for at least 2h till PLLA was dissolved. After the PLLA/DCM solution was cooled to room temperature, DMF was added at the certain ratios. The Duran bottle contains this

PLLA/DCM/DMF ternary system mixture was sealed and stirred at room temperature for at least 1 day. This ternary solution should be further used within 2 days to avoid the evaporation of organic solution.

3.2.2 Electrospinning method and post treatment

TL-Pro Electrospinning Units contains a semi-hermetic chamber connecting ventilation pipe. One or two Luer plastic syringes could be used to load electrospinning solutions which were ejected at controlled feed rate through different metal needles by a dual positions syringe pump (TL-F6, Tongli Tech, China). The vertical dimension of the electrospinning needle could be adjusted, and the horizontal scanning distance could be set from 0 to over 50 cm. This machine uses a grounded metallic rotating roller whose diameter is 10 cm to collect nano-fibres. A baking paper or a foil paper was covered and fixed on the roller to hold the fibres. Voltage and receiving distance between the needle and rotating roller could be set respectively. The distance between needle to collector could be adjusted from very close to 35 cm.

The specific parameters electrospun fabrication used in this project were listed in Table 3.1. Due to the chamber of Electrospinning Unit is semi-hermetic, the interior environment of this chamber cannot be controlled precisely by the heating lamp and humidifier.

Table 3. 1 General experimental parameters of electrospinning method in this project.

Electrospinning Parameter	Value and Unit
PLLA concentration	1.8-2.2 wt%
DCM volume in solvent	95% wt
DMF volume in solvent	5% wt
Camber temperature	~20°C
Camber humidity	~30%
Spinning time	0.5-4.5 h
Ejection speed	5 ml/h

Receiving distance	20 cm
Rotation speed of the receiving roller	200 rpm
Spinning voltage	23 kV

Pristine electrospun fibrous membrane need to be kept in spinning unit chamber with ventilation pipe or fume board for 4 h to evaporate organic solvent. Then, the fibrous membrane was peeled-off from holding baking paper or foil paper and fixed by a stainless-steel frame for post-treating. The fixed pristine PLLA fibrous membrane was immersed into acetone bath for 5 mins as the post-treatment.

3.2.3 Preparation of silk fibroin aqueous solution

Silk fibroin was dissolved by using lithium bromide solution [77]. Frankly speaking, natural *bombyx mori* silk was degummed in the boiling 0.02 M Na₂CO₃ aqueous solution. The degummed silk was dissolved by 9.3 M LiBr aqueous solution in 60°C oven for 4 h. Cellulose semi-permeable membranes (molecular weight cut-off 12,000-14,000, SERVAPOR, Germany) was applied to dialysis the dissolved high concentrated silk fibroin/LiBr solution. The regenerated silk fibroin solution was filtrated and centrifuged twice for further processing. To examine the concentration of silk fibroin solution, 1 ml freshly prepared SF solution was doped on the petri dish and put the solution and dish into a 60°C oven for 4 hours. After the water in SF solution evaporated, the concentration could be measured by dividing the weight of left SF solid membrane and original 1 ml SF solution. In most cases, the concentration of freshly dissolved SF solution by LiBr, the protocol used in this work, is around 6-7 % w/w. It can be diluted to lower concentrations by water or concentrated to higher concentrations by large molecular weight polyethylene glycol.

3.3 Characterizations

3.3.1 Thickness of fibrous membrane

PLLA fibrous membrane is quite loose before acetone treatment. After treatment, it becomes more compact, like a piece of tissue paper. So, the thickness of one layer of membrane is too small to be measured accurately. The fibrous membrane was folded and measured 8 layers of samples by a Mitutoyo thickness gauge (PK-0505, Japan). Its accuracy is 1 μm .

To further confirm the thicknesses, another micrometre gauge (RS Pro 705-1279, UK), with accuracy $\pm 2 \mu\text{m}$ and resolution 1 μm , was used for verification measurement. This micrometre follows the standard T411 om-97, which applies to soft materials. The results are consistent with that of Mitutoyo gauge.

3.3.2 Surface morphology

The surface morphology of PLLA fibres was observed by a field emission scanning electron microscope (FE-SEMs, Zeiss Ultra55, Germany) after platinum coating. For each sample, one cut small piece specimen was attached on adhesive carbon tape and coated a 10-nm-thick platinum layer by a sputter coater (Emitech K550, USA). To avoid PLLA fibres melting under the field emission gun, the operating voltage of SEM was 1.5 kV.

3.3.3 Thermophysical Properties

Differential scanning calorimetry (DSC) was performed using Q1000 (TA instrument Ltd., DE USA), under a nitrogen (N_2) flow, with a heating rate of $10^\circ\text{C}/\text{min}$ from 20 to 200°C . Thermogravimetric analysis (TGA) was employed via Q500 (TA instrument Ltd., DE USA) to analyse properties of samples under a range of temperatures which are between 30°C and 800°C and the heating rate is set at $10^\circ\text{C}/\text{min}$.

3.3.4 Mechanical performance

The tensile test for PLLA fibrous membrane was prepared by following the

schematic in Fig 3.1. The effective testing area of fibrous membrane was a 25 mm × 5 mm rectangle. The tensile tests of membrane samples were run on INSTRON 3344 (MA, USA) with a 5 N cell load at a deforming rate of 5 mm/min. Based on the recorded stress–strain curves, Young’s module and tensile strength were obtained. Five samples of each membrane group were repeated for the mechanical properties of fibrous membrane.

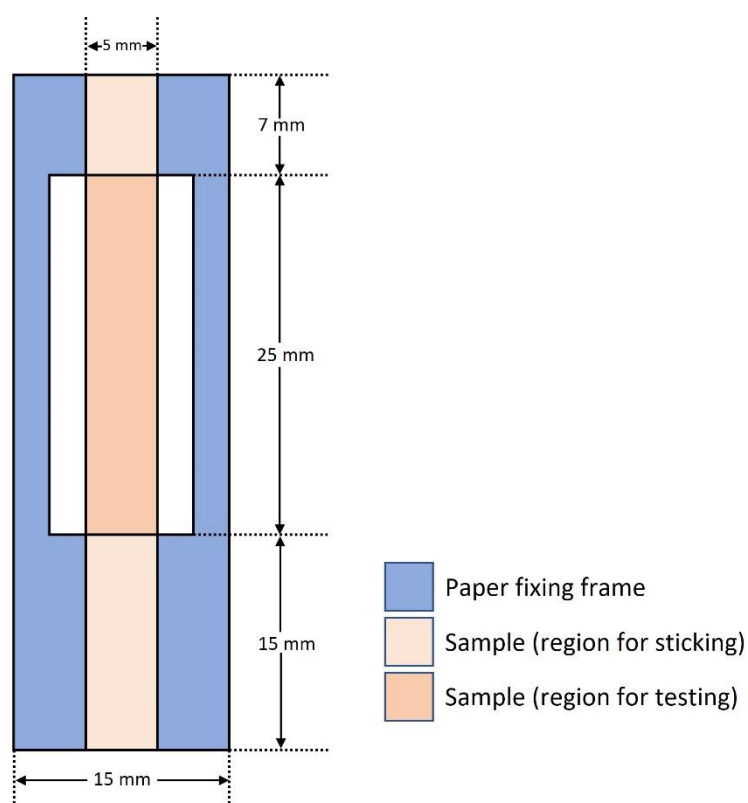


Fig. 3. 1 Schematic diagram with size of paper fixing frame for mechanical test samples.

3.3.5 XRD

X-ray diffraction (XRD) patterns of samples before and after post-treatment were performed via a X’Pert Pro’s X-ray diffractometer (Panalytical, UK) with reflection mode Cu-K α radiation operated at a voltage of 40 kV and a filament current of 40 mA, employing a scanning rate of 2 °/min in a 2 θ range from 4° to 65°.

Chapter 4: Hierarchical Porous PLLA Fibrous Membrane for Aerosol Filtration

Reprinted (adapted) with permission

Jun Song, Bowen Zhang, Zihan Lu, Zhiying Xin, Ting Liu, Wenyuan Wei, Qasim Zia, Kewen Pan, R. Hugh Gong, Jiashen Li.

Hierarchical Porous Poly(l-lactic acid) Nanofibrous Membrane for Ultrafine Particulate Aerosol Filtration.

ACS Applied Materials & Interfaces **2019**

<https://doi.org/10.1021/acsami.9b18083>

Copyright © (2021) American Chemical Society.

My contributions:

I have examined the parameters and prepared the samples of PLLA fibrous membranes. I also did the further characterizations including optimizing air filtration and press drop tests, but except several SEM images for membranes. I analysed all the data, drew all the figures, and wrote the manuscript solely.

4.1 Chapter Synopsis

An aerosol filter with hierarchical pore structure was developed by the solvent-treated electrospun PLLA fibrous membranes. Firstly, nano/micro PLLA fibres were prepared by electrospinning with dual solution system to form a membrane (Fig. 1 i). In order to further increase the surface area of PLLA fibres, fibrous membrane was treated by acetone to achieve a blossoming porous structure throughout each single fibre (Fig. 1 ii). Consequently, the specific surface area of fibres and fibrous membrane was improved dramatically, while PLLA was transformed from amorphous to crystalline state. With a hierarchical porous structure from several nanometres to several micrometres, the treated PLLA membranes were investigated as filters for removing ultrafine particles from air. Aerosol filtration efficiency tests of sodium chloride (NaCl) aerosol particles (≤ 100 nm) were conducted for the obtained PLLA membrane samples prepared with different PLLA weight percentage in solutions and electrospinning time. The high specific surface area and large pore volumes of certain PLLA membranes contributed to excellent filtration efficiency (99.99%) for ultrafine aerosol particles (30-100 nm) with a low pressure drop (110-230 Pa) continuously. Under 7.8 cm/s flow rate, the membrane samples performed better for filtering smaller-sized aerosol particles than the larger ones when evaluated by the quality factor. The findings demonstrate that the electrospun membrane with hierarchical pore structure can be used as filter materials under salty and moist environments.

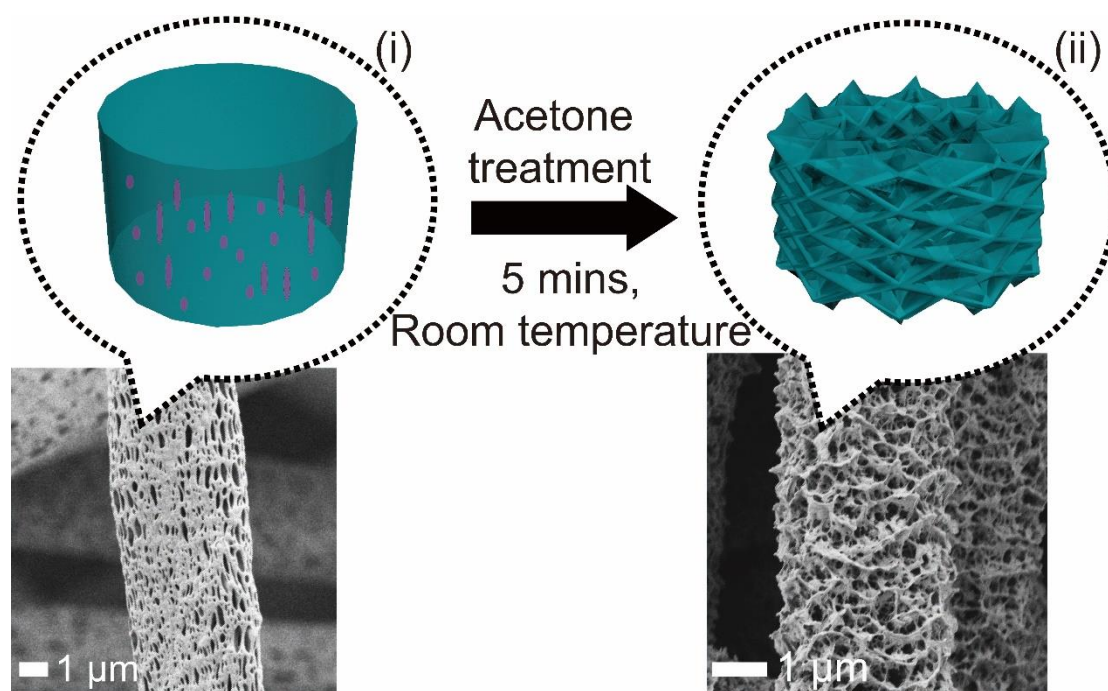


Fig. 4. 1 Schematics of the pristine electrospun PLLA fibre and hierarchical porous PLLA fibre after acetone post-treatment.

4.2 Literature Review: Fibrous Membrane Filter for Ultrafine Aerosol Particles

Air pollution has been increasing globally due to increasing industrialization. Finding solutions to reduce air pollution has long been an important research topic to the researchers [78]. It has been suggested that air pollution is the health risk factor which exceeds that of cigarette smoking [79]. Typical air pollution aerosol particles composed of microscopic solid or liquid matter suspended in the atmosphere of earth are generally classified as particulate matter under $2.5\text{ }\mu\text{m}$ ($\text{PM}_{2.5}$) or PM_{10} [80,81]. Research on filter membrane materials for such particle sizes has been widely practised, and commercialised products have emerged [63]. However, for particles below $0.3\text{ }\mu\text{m}$, mainly relating to smoke, virus and carbon dust, filter materials and devices are still being developed. Some standards have been set up by the US Department of Energy or European Union to distinguish types of air filter among High-Efficiency Particulate Air

filters (EPA, HEPA, ULPA) [82,83]. Nevertheless, even the highest standard, Ultra-Low Particulate Air filter (ULPA), is classified as for filtering particle sizes above 100 nm only. There is currently no standardised commercial classification of filter materials for aerosol particle sizes smaller than 100 nm.

In 1827, a Scottish scientist, Robert Brown, found a phenomenon called “Brownian movement”. This theory believes that nanoparticles always keep in random movement in the air caused by the bombardment of gas molecules. It is a significant finding for investigating the mechanism of air filtration by membranes. For aerosol particles with a size lower than or equal to 100 nm, the filtration efficiency of fibrous membranes is more manifested as a diffusion mechanism and contains a few impactions [84]. Based on this theory, while ensuring the fibrous membrane structure, increasing the specific surface area of the fibres can significantly trap more aerosol particles by the filters [63,84]. For this level of particle sizes, the typical applications are for reducing the spread of airborne pathogens, carbon dust and sea salts in recirculated air of pharmaceutical or semiconductor manufacturing ultra-clean rooms, aircrafts and military assets [84]. For example, the M1 series main battle tank of the United States Army uses an electrospun fibrous membrane material as the main filter for its air-filtering apparatus [85].

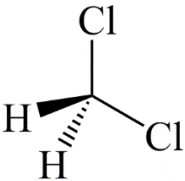
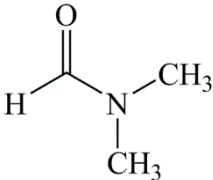
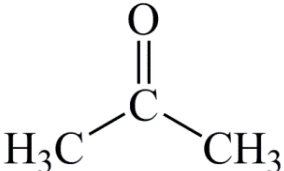
It is an objective of this study to produce a hierarchical porous fibrous membrane with a high porosity and blossoming porous electrospun fibres while maintaining the diameter at sub-macro size. By contrast, the conventional idea is that increasing the specific surface area of the membrane material by fabricating the finer nano-scale fibres, and to increase the contact between the material and the aerosol particles to achieve a better filtering result in the current research on electrospinning air filtration materials. Both dual solution electrospinning and post-treatment processes are applied to achieve the hierarchical structure. Induced phase separation and solvent induced crystallization are porous structure forming mechanisms of electrospinning and post-treatment processes, respectively. While traditional filters for macroscale particles such as PM 2.5 have been studied widely, this research focuses on the aerosol filtration of particles from 30 to 100 nm.

4.3 Materials and Methods

4.3.1 Materials

PLLA (PL 65) was obtained from PURAC biochem, Holland. DCM and DMF, as shown in Table 4.1, were purchased from Sigma-Aldrich, Co., USA. All other chemicals were of analytical grade without any further purification and purchased from Fisher Scientific, UK.

Table 4. 1 Properties of solvents used in this project (boiling point; viscosity (η); dielectric constant (ϵ); Hansen solubility parameter (δ) [47]; vapour pressure).

Solvent	Boiling Point (°C)	Dielectric Constant	Solubility Parameter (MPa ^{1/2})	Vapour Pressure (mmHg, 20°C)	Structure
DCM	39.8	9.1	18.4	354.8	
DMF	153	36.7	24.8	2.7	
Acetone	56	20.6	19.7	184	

4.3.2 Preparation of PLLA solution, electrospinning and post-treatment

PLLA granules were dissolved by a dual solvent system at concentrations ranging from 1.6 to 2.2 wt%. Dual solvent consists of DCM and DMF at 19:1 w/w. PLLA

granules were added into DCM and stirred for 1 h at 60°C, and then DMF was added dropwise and stirring continued until PLLA completely dissolved.

The electrospinning operation was conducted by a Nanofibre Electrospinning Unit (TL-Pro, Tongli Tech, China). Luer plastic syringes were used to load PLLA solutions which were ejected at a controlled 5 ml/h feed rate through a metal needle with an inner diameter of 0.8 mm by a syringe pump (TL-F6, Tongli Tech, China). PLLA fibrous membrane was collected on a grounded metallic rotating roller whose diameter is 10 cm. Voltage and receiving distance between the needle and rotating roller were set as 23 kV and 30 cm respectively. This electrospun setup was shown in the Fig. 4.2. For post-treatment, the electrospun PLLA membrane (Fig. 4.3) was immersed in acetone for 5 minutes at room temperature and then dried in the air. The details of experimental settings are shown in Table 4.2.

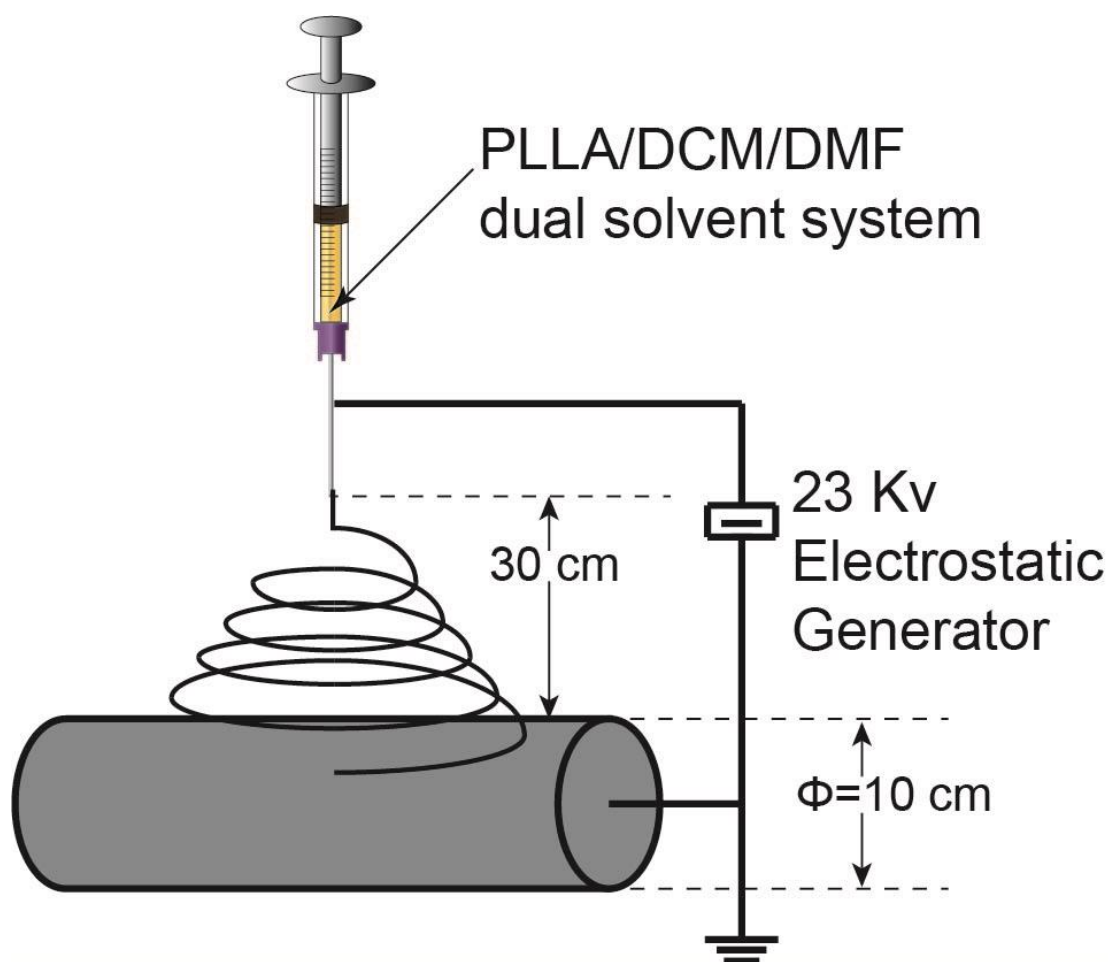


Fig. 4. 2 The schematic of an electrospinning process.

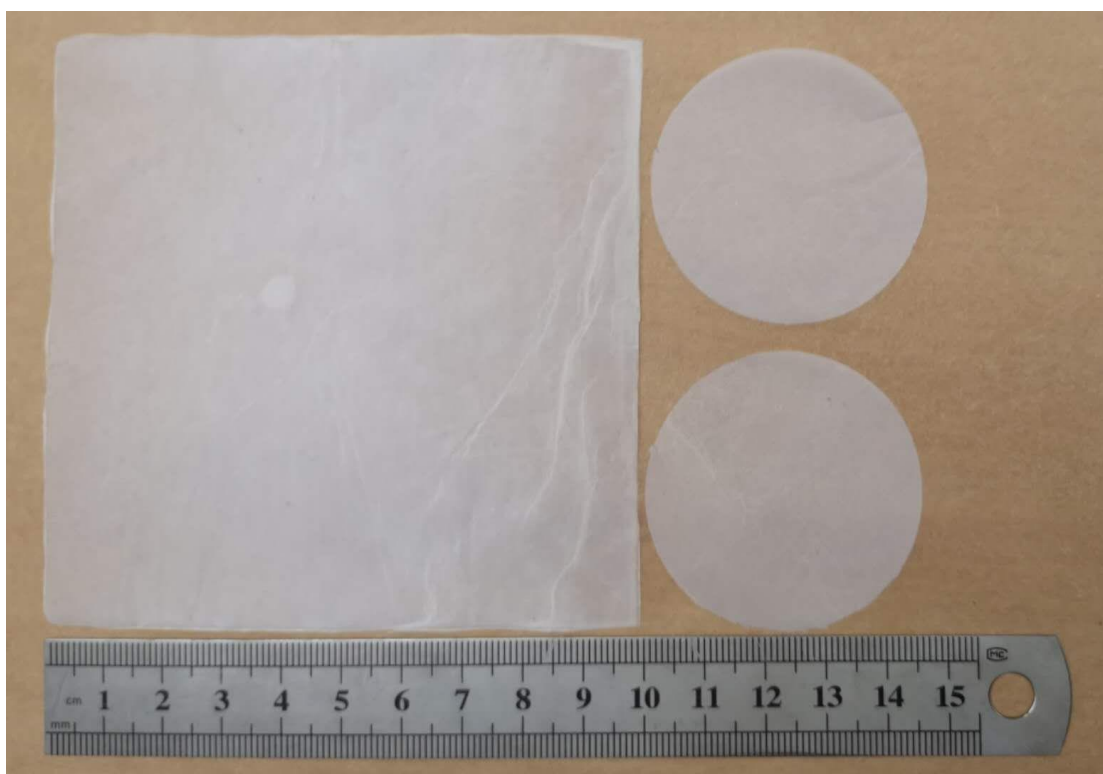


Fig. 4. 3 The photos of a piece of treated PLLA membrane and round air filter samples.

Table 4. 2 Electrospinning parameters. ,.

Sample ID	PLLA concentrations (wt%)	Electrospinning time (minutes)	Sample thickness (μm)
S-1A	1.6	60	8.75 ± 1.15
S-1B	1.6	90	13.25 ± 1.11
S-1C	1.6	120	17.00 ± 0.88
S-2A	1.8	60	12.50 ± 2.16
S-2B	1.8	90	14.00 ± 1.04
S-2C	1.8	120	18.00 ± 1.04
S-3A	2.0	60	14.75 ± 0.88
S-3B	2.0	90	17.25 ± 1.05
S-3C	2.0	120	19.25 ± 1.89
S-4A	2.2	60	22.00 ± 2.42
S-4B	2.2	90	24.75 ± 1.04
S-4C	2.2	120	31.75 ± 1.85

4.3.3 Characterizations

Field emission scanning electron microscopy (FE-SEM) images of membrane specimen were obtained after gold-coating via an Ultra 55 (Zeiss, Germany) with 5 kV and 1.5kV accelerating voltage. Images processing software (ImageJ) was used to calculate fibre diameters and pore sizes.

Thermogravimetric analysis (TGA) was employed via Q500 (TA instrument Ltd, USA) to analyse properties of samples under a range of temperatures which are between 30°C and 800°C and the heating rate is set at 10°C/min.

Different scanning calorimetry (DSC) was performed using Q1000 (TA instrument Ltd, USA), under nitrogen flow, with a heating rate of 10°C/min from 20°C to 200°C. Both before and post treatment samples were measured three times and the average of three times was recorded.

Tensile test of samples before and after post-treatment were run by INSTRON 3344 (INSTRON, USA) at a deforming rate of 5 mm/min. The samples were cut into 5 × 47 mm². From the recorded stress-strain curves, the Young's module and tensile strength were obtained.

XRD characterization was performed by following the section 3.3.5.

The Nitrogen (N₂) adsorption and desorption characterization was conducted over the relative pressure range (0.00005-0.99) via QUADRASORB Evo Surface Area Analyser (Quantachrome, USA) at 77 K while BET and density functional theory (DFT) methods were used to analyze specific surface area, specific pore volume and pore size distribution.

The porosity (ε) of PLLA fibrous membrane was evaluated by the following equation:

$$\varepsilon = \left(1 - \frac{m}{Z \cdot S \cdot \rho}\right) \times 100\% \quad (4.1)$$

where m is the weight (mg) of the membrane samples measured by an electronic balance (Ohaus, Switzerland); ρ is the density of PLLA raw materials that is 1.27 g/cm³. Z is the thickness (mm) of membrane samples were measured by and PK-0505 thickness gauge (Mitutoyo, Japan) and S is the samples size (mm²) of relevant samples.

4.3.4 Air filtration and pressure drop tests

The aerosol filtration efficiency of membrane was measured with a self-designed combined system which is shown in Fig. 4.4 and its optical photo is shown in Fig. 4.5. This system included one aerosol particle generator (ATM 226, Germany), one scanning mobility particle spectrometer (SMPS, TSI 3082, USA) and two ultrafine condensation particle counters (CPC, TSI 3776, USA). Sodium chloride (NaCl) aerosol particles of 30, 50, 100 nm average diameters were prepared by the aerosol particle generator. The particle size was controlled by an electric field in SMPS. Two CPC were used to collocate particle quantity before and after filter membrane for further analysis. The membrane was prepared as 47 mm diameter circular samples and fixed in a filter holder then flowed through by neutralized NaCl aerosol particles with the continuous air flow rate at 7.8 cm/s. It should be noticed that this air filtration test was relied on the assistance with National Atmospheric measure facilities in National Centre for Atmospheric Science (NCAS, UK). However, NCAS only granted a two-day study for this project. Thus, the experiments only took once for each group of samples.

The pressure drop of membranes was measured by air permeability tester (M021A, Sdlatlas, India) with the samples cut as 20 cm² size and the same air flow rate with the filtration tests. In the literature, the quality factor (QF) was commonly referred to as the tread-off parameter to measure filtration performances of materials comprehensively [86]. The QF equation is defined as:

$$QF = \frac{-\ln(1-\eta)}{\Delta p} \quad (4.2)$$

where η and Δp are the filtration efficiency and pressure drop across the membrane, respectively.

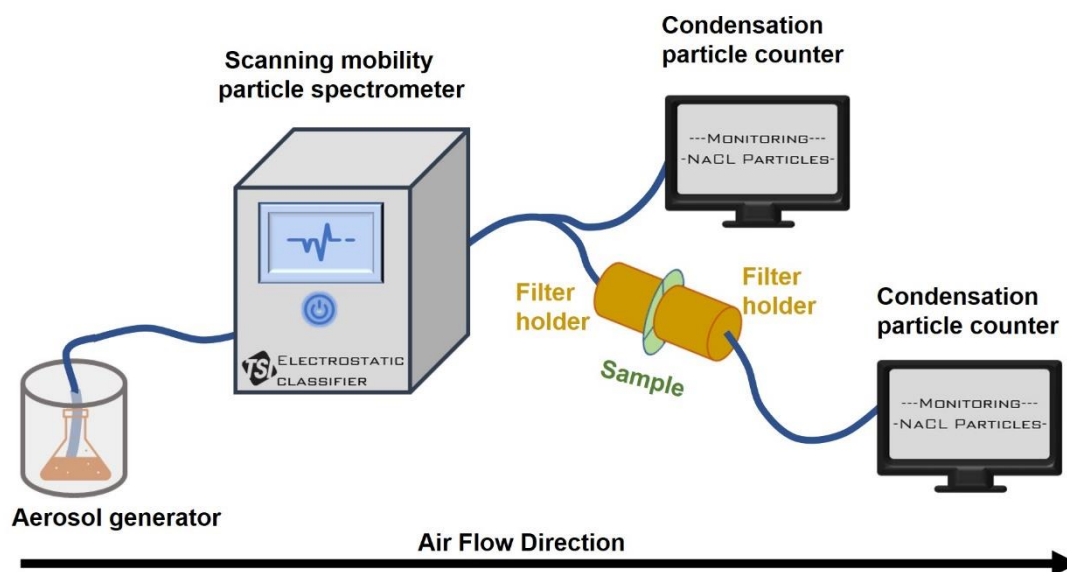


Fig. 4. 4 Schematic diagrams of air filtration testing instrument setup.



Fig. 4. 5 The air filtration instatement setup.

NaCl aerosol particles of 30, 50, 100 nm average diameters were prepared by the aerosol particle generator. The particle size was controlled by an electric field in SMPS.

Two CPC were used to collocate particle quantity before and after filter membrane for further analysis. The membrane was fixed in a filter holder and flowed through by neutralized NaCl aerosol particles.

5.3.5 Statistics

Fibre diameters were calculated via ImageJ (NIH, USA). Tensile and specific surface area results were expressed as means \pm standard deviations. Statistical differences between samples were evaluated by Student's t-test in Origin software (9.0) using the least significant difference (LSD).

4.4 Results and Discussions

4.4.1 Morphology and induced phase separation mechanism

Fig. 4.6 - 4.9 showed the well uniformed original electrospun fibrous membrane and detailed calculation of their diameter sizes are in Fig. 4.14. At the same time, the unevenness of the fibrous membrane surface is clearly shown by the depth of field of SEM images. The surface of original fibrous membrane shows two completely different structures, one with nano-sized pits or pores on flat fibres and the other roughly wrinkled. The pores could be attributed to the breath figure theory while wrinkles are resulted from the spinodal phase separation, occurred after the evaporation of solvent during the electrospinning process. Furthermore, the rough surface morphology can be ascribed to the combination of these two mechanisms. As the concentration of PLLA increases, the electrospun fibres begin to evolve from circular cross section fibres to strip fibres. It is because the addition of DMF causes the evaporation rate of the solvent to decrease.

Solvent selection is a key factor influencing the morphology and other properties of electrospun fibres. DCM is an excellent solvent for PLLA and highly volatile, whilst DMF is a poor solvent for PLLA granule, especially with very high molecular weight. As phase separation includes three sub-classifications, the mechanisms in this study are

a mixture of non-solvent induced phase separation (NIPS) and vapour induced phase separation (VIPS). The NIPS occurs when a non-solvent is incorporated into the polymer solution. In this case, it is done by adding 5 wt% DMF into PLLA-DCM solution as a non-solvent. VPS happens if a water-miscible solvent with high boiling point is involved in a related humid space, and DMF plays this role in this study as its boiling point is 153°C. Thus, DCM and DMF were selected as the dual solvent because their boiling points, solubility and volatility are all significantly different.

The membrane samples after post-treatment are shown in Fig. 4.10 -4.13. Their morphology differs significantly. Also, the fibre diameter increased sharply with the increasing of PLLA solute concentrations as shown in Fig. 4.14. This kind of porous structure guarantees a significant improvement of specific surface area and pore volume. Additionally, lamellae structure, which was transverse to the direction of the fibres, was clearer than the original membrane. The small interspaces among lamellae range from 10 nm to 100 nm. These can service as traps of small particles. Furthermore, the enhanced surface roughness of the PLLA fibrous membrane can increase the friction coefficient between the fibres and the particles during air filtration, which helps the capture of particles less than 100 nm.

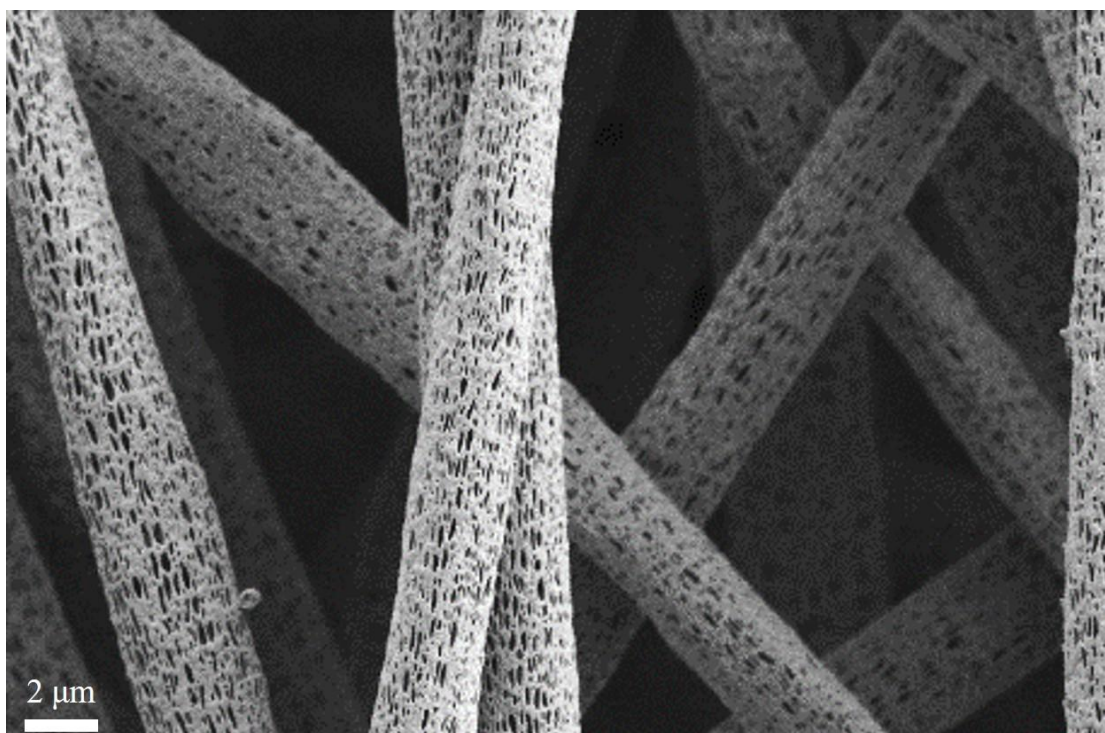


Fig. 4. 6 SEM image of 1.6 wt% (S1-B) electrospun PLLA fibrous membrane before treatment.

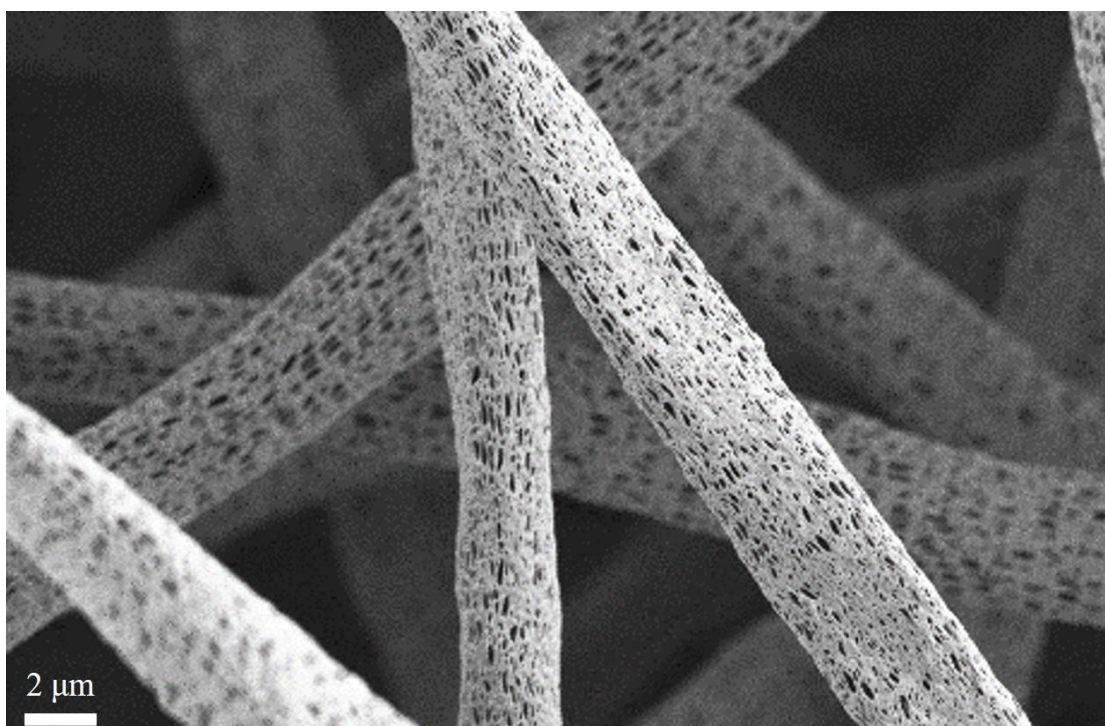


Fig. 4. 7 SEM image of 1.8 wt% (S2-B) electrospun PLLA fibrous membrane before treatment.

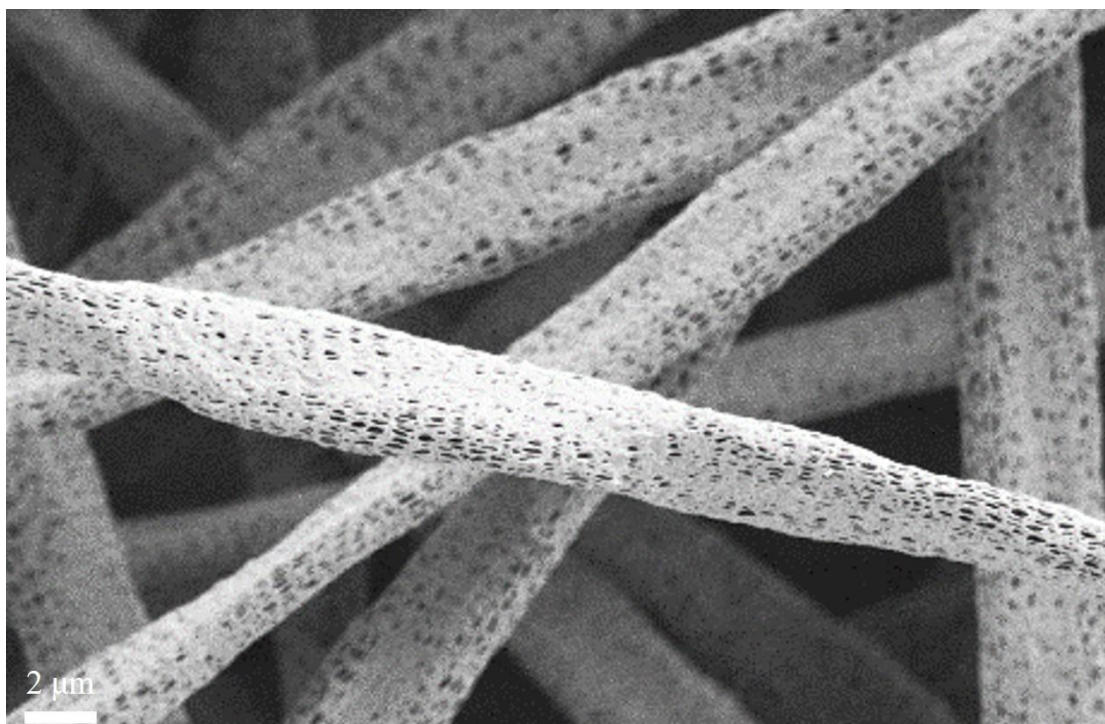


Fig. 4. 8 SEM image of 2.0 wt% (S3-B) electrospun PLLA fibrous membrane before treatment.

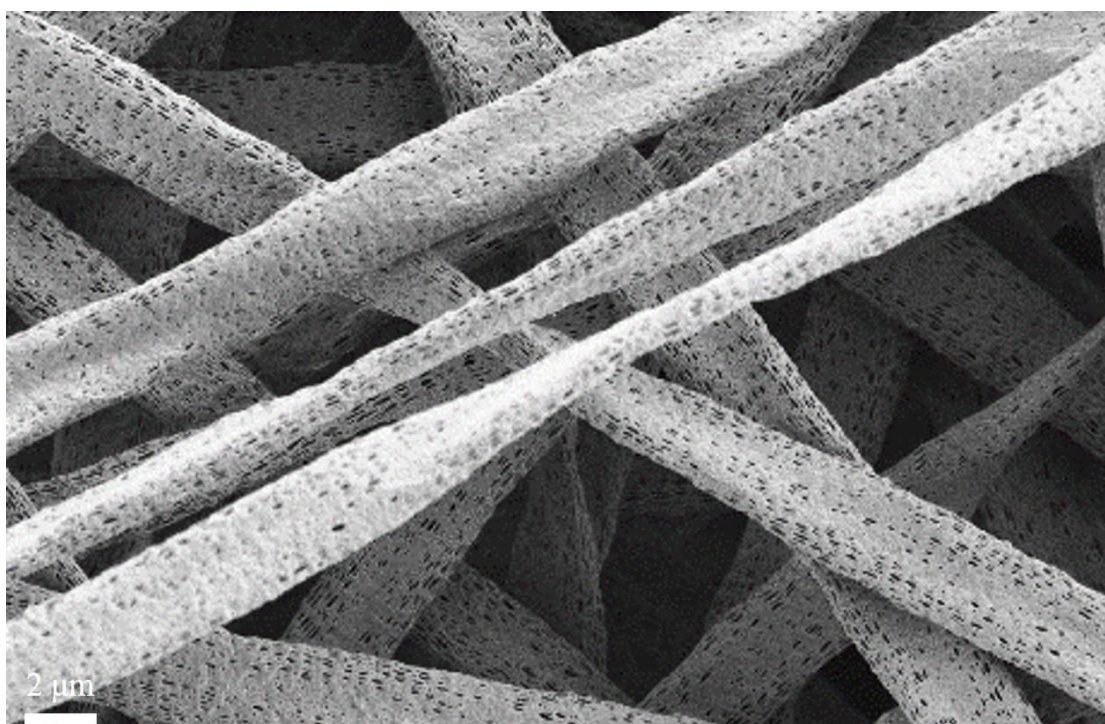


Fig. 4. 9 SEM image of 2.2 wt% (S4-B) electrospun PLLA fibrous membrane before treatment.

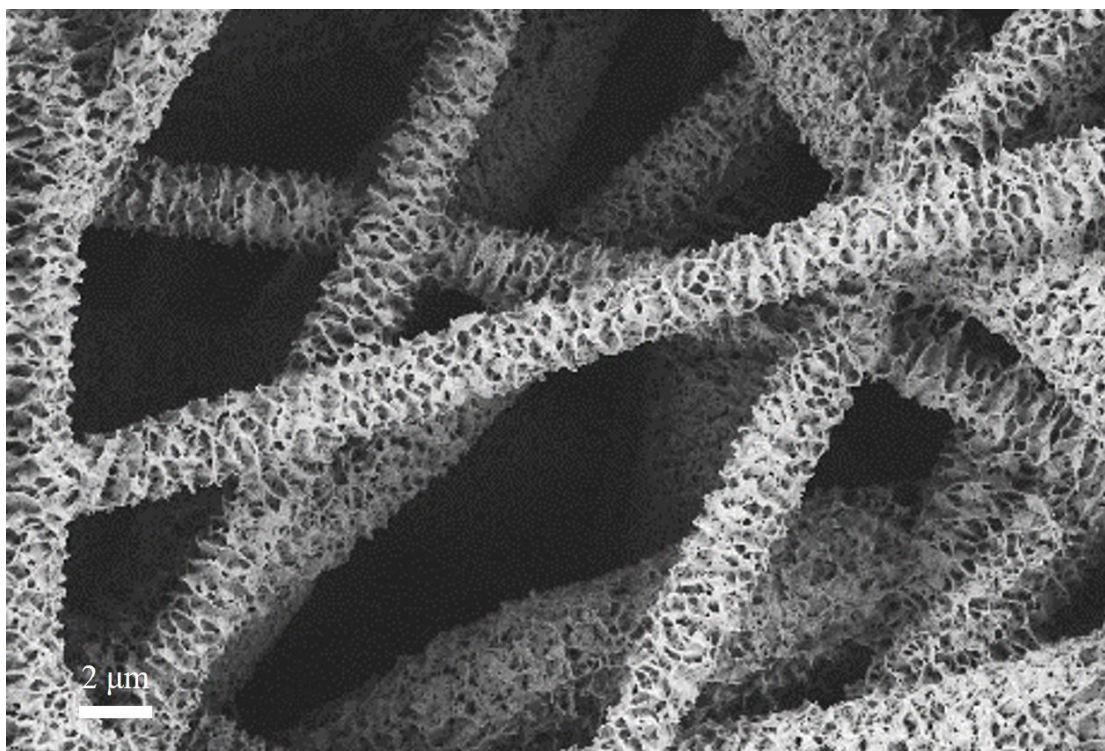


Fig. 4. 10 SEM image of post-treatment 1.6 wt% (S1-B) electrospun PLLA fibrous membrane.

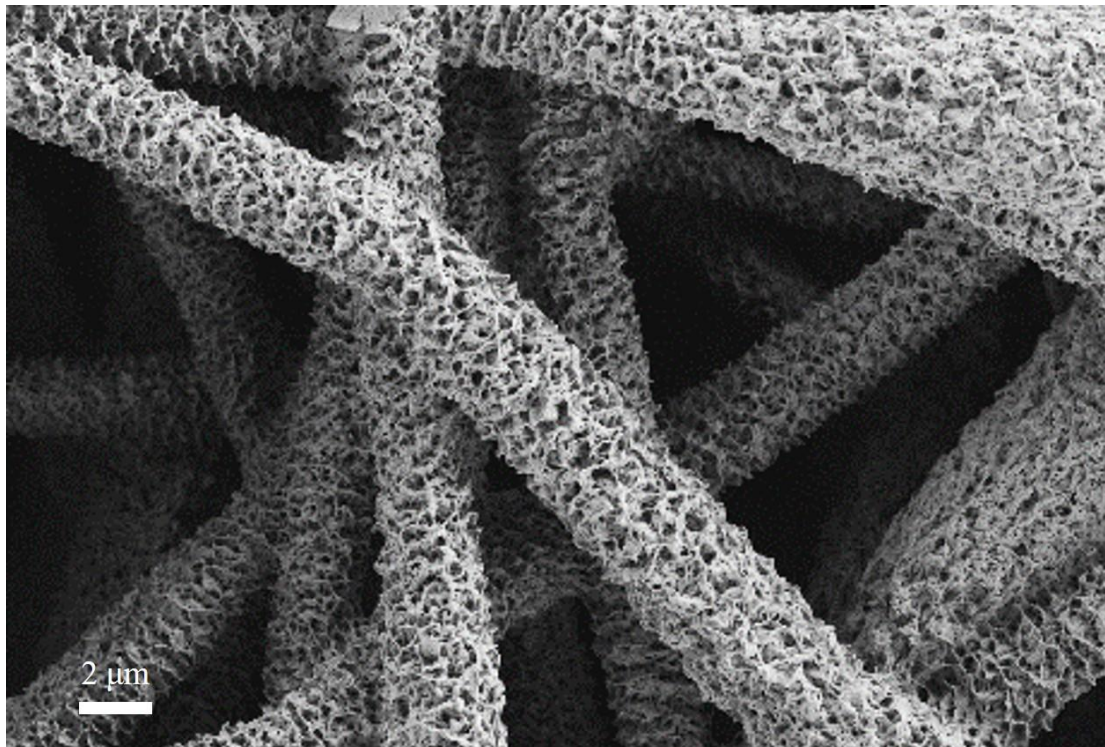


Fig. 4. 11 SEM image of post-treatment 1.8 wt% (S2-B) electrospun PLLA fibrous membrane.

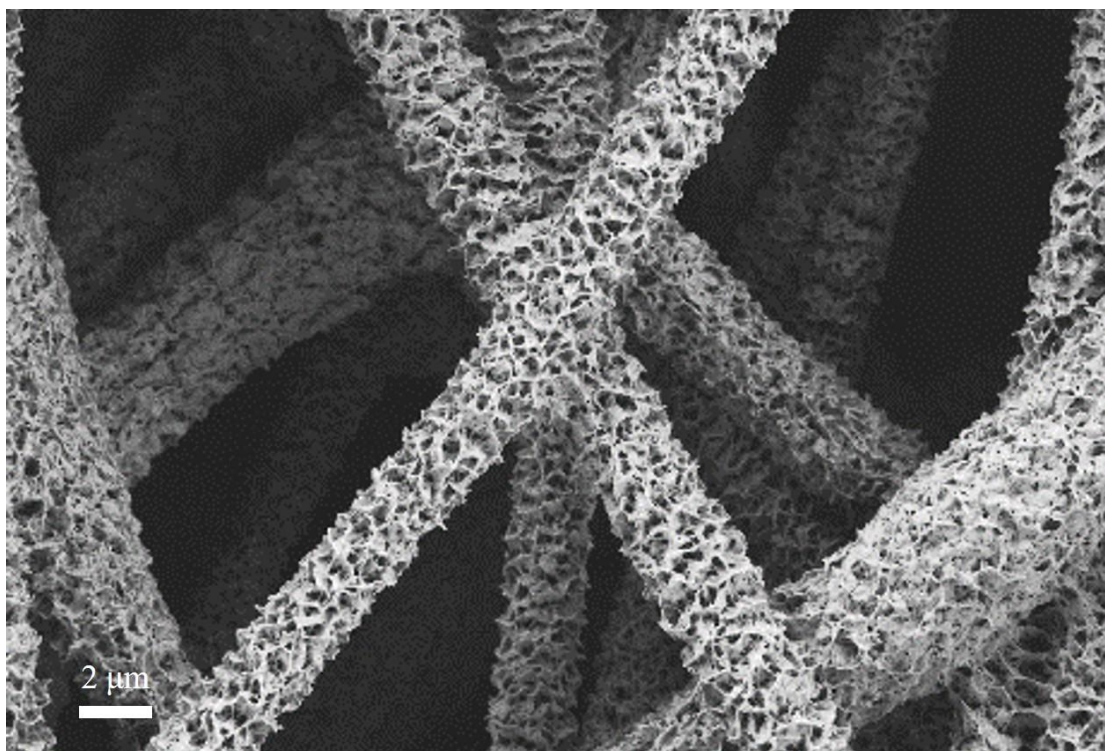


Fig. 4. 12 SEM image of post-treatment 2.0 wt% (S3-B) electrospun PLLA fibrous membrane.

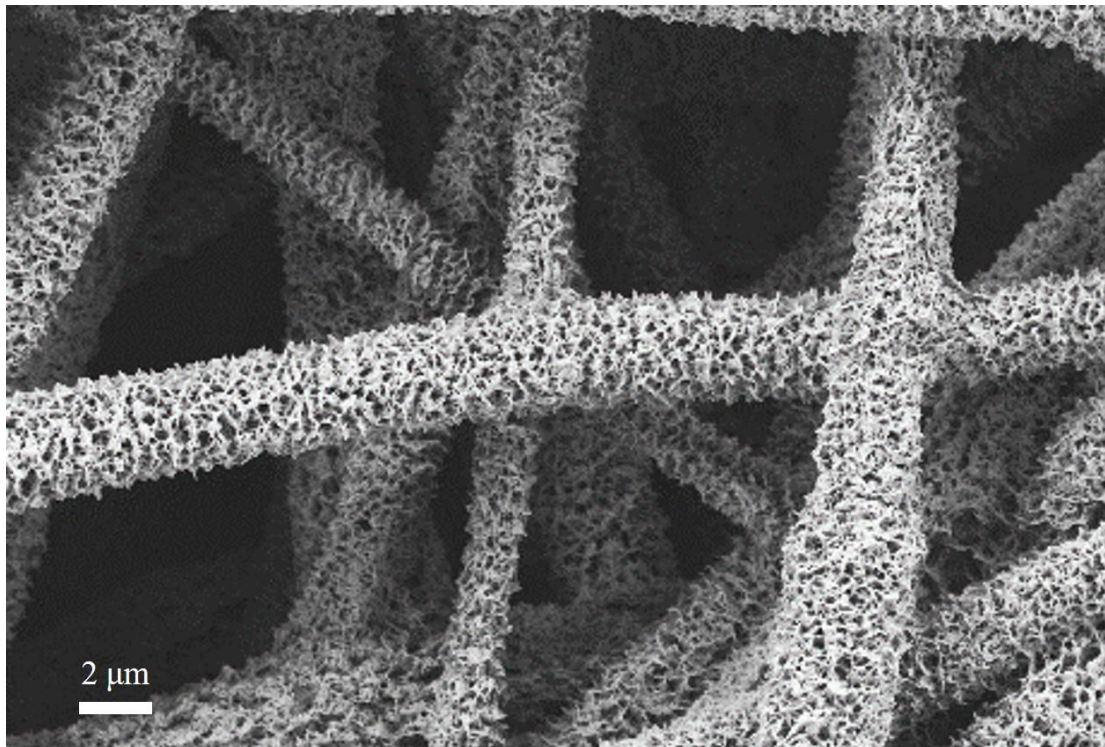


Fig. 4. 13 SEM image of post-treatment 2.2 wt% (S4-B) electrospun PLLA fibrous membrane.

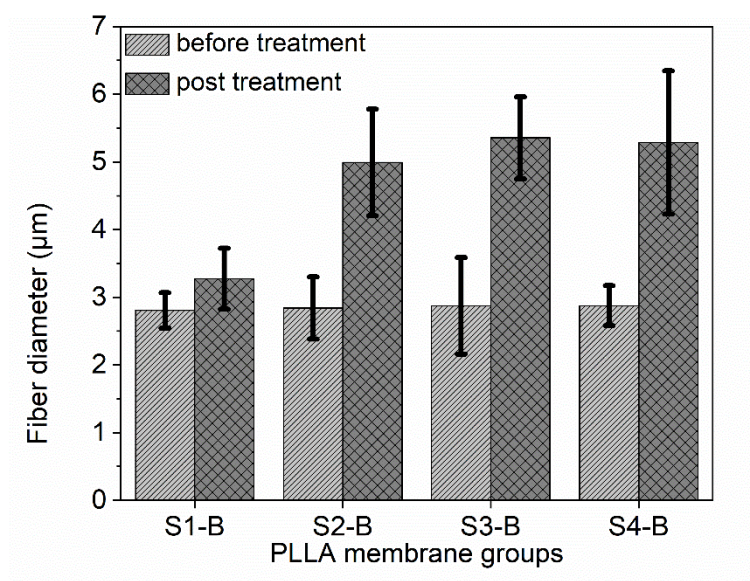


Fig. 4. 14 Fibre diameter of B group samples, before treatment and post treatment.

4.4.2 Mechanical property and crystallization mechanism.

Due to the low-speed crystallization of PLLA and the rapid solvent evaporation break solute polymer chains to form ordered structures during electrospinning process, collected PLLA membrane remains in low crystalline state in majority. From the smoothed XRD patterns of before and after post-treatment samples (Fig. 4.15), the crystallization state of membranes can be analyzed qualitatively [12]. The broad diffraction peak of original electrospun PLLA fibres illustrates that most of fibres keep their low crystalline state which leaves room for the solvent induced recrystallation of polymer chains.

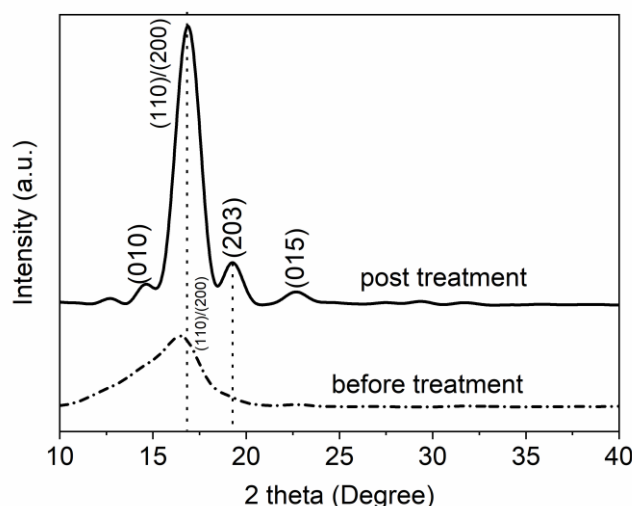


Fig. 4. 15 XRD patterns of PLLA fibrous membranes.

Four XRD diffraction peaks of post-treatment sample are shown in solid lines which show high crystallization. Without post treatment, the crystallization peak of electrospun PLLA is quite weak which is shown in dotted line.

After PLLA fibres were treated by acetone, four crystallization peaks can be observed. The most intense diffraction peak of treated PLLA sample is at 16.6° which is referred to as (200)/(110) plane [87]. Another dominant peak appears at 19.0° which is attributed to (203) reflection. There are two other relatively weak peaks located at 14.7° and 22.3° , which indicate (010) and (015) crystal planes. Regarding this crystallization conditions, PLLA is crystallized into α modification that is most common under a cold or solution crystallization circumstance. Since the location of (200)/(110) and (203) planes are relatively regular and not shifted to a higher angle values nor decreased in lattice spacing, the post-treatment membrane is a stable standard α -form instead of an extremely disordered α' -form. The mechanical and thermal properties of an electrospinning polymer membrane strongly depend on the crystal structure and morphology. The low mechanical property is one of shortcomings for electrospinning semi-crystalline polymer membrane, but crystallized structure can overcome this problem. The electrospinning process of this study allowed the PLLA to remain in an amorphous state by selecting a volatile solvent (DCM) [88]. This protocol implements post-treatment to induce polymer crystallization.

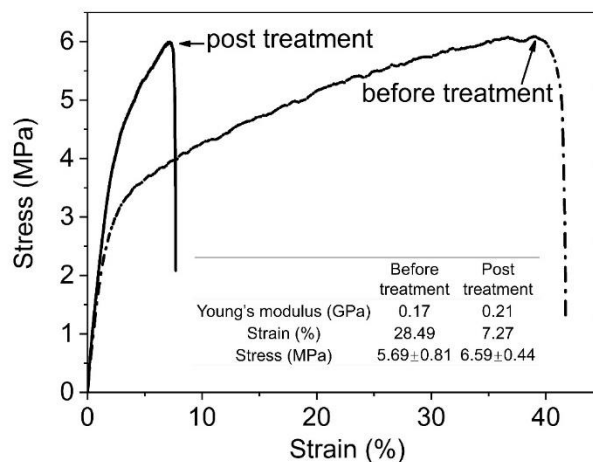


Fig. 4. 16 Stress-strain curves of PLLA fibrous membranes.

The stress-strain curves of post-treatment sample is shown by black solid line and before treatment sample is shown in light grey dotted line.

The tensile strain-stress curves of the electrospun PLLA nanofibrous membrane are shown in Fig. 4.16. About 2% or 3% linear elastic behaviour deformations are observed for before and post treatment samples. Consistent with the XRD results, the Young's modulus of sample has been improved as the membrane is crystallized by acetone. However, after crystallization, the elongation break of the sample is significantly reduced. The pristine membrane exhibits more ductile fracture because of its amorphous form. Comparing with other randomly oriented fibres [6,7], this fibrous membrane achieves higher Young's module and tensile strength. The before and after treatment samples of group S2-B were selected for both tensile and XRD characterizations. Compared with the ductile fracture and low modulus sample, the high modulus crystalized membrane is more suitable for short-duration and high-intensity filtration demand.

4.4.3 Thermal properties analysis

In order to compare the difference between samples before and after treatment, the DSC tests were conducted by heating only instead of heating-cooling-heating cycles.

The traces of DSC (Fig. 4.17) showed that the original sample has a relatively high glass transition temperature (T_g) and cold crystallization temperature (T_{cc}), whereas the treated sample has a relatively low T_g . It is proposed that T_{cc} of the pristine sample corresponds to the amorphous state polymer chains having mobility above their T_g and recrystallization. The phenomenon would not be possible in semi-crystalline polymers. The lower T_g after treatment is ascribed to the residual acetone, which is regarded as a plasticizer in the polymers. The result of DSC also matched that of XRD, further confirming the crystallisation after treatment.

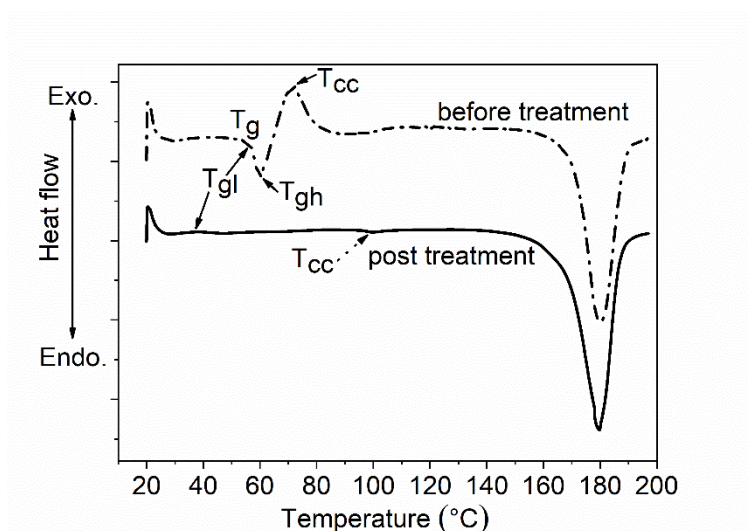


Fig. 4. 17 DSC traces of samples. Post-treatment sample is shown by solid line and before treatment sample is shown in dotted line.

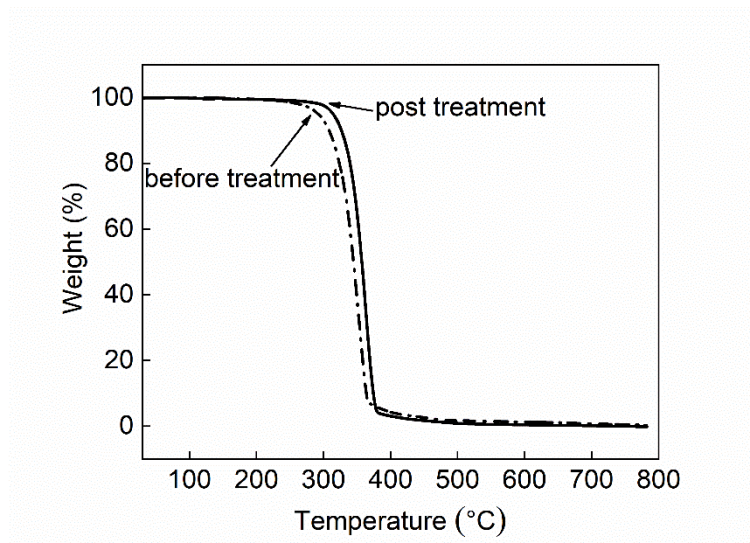


Fig. 4. 18 TGA curves of samples. Post-treatment sample is shown by solid line and before treatment sample is shown in dotted line.

Low glass transition temperature (T_{gl}), high glass transition temperature (T_{gh}) and cold crystallization temperature (T_{cc}), are illustrated.

As shown in Fig. 4.18, TGA of the samples before and after treatment confirms the presence of crystallized polymer with the post-treatment, as a cross validation for XRD and DSC analysis.

Original membrane has been found to thermally decompose at $\sim 300^{\circ}\text{C}$ whilst post-treatment processed one decomposes at a higher temperature of $\sim 320^{\circ}\text{C}$, which can be explained by a more thermally stable structure of PLLA fibres. The thermal decomposition curves for the blend fibres show distinct peaks for degradation temperatures of the two blend polymers, as shown in Fig. 4.18. Both before and after treatment samples significantly have weight losses, 0.227% before treatment and 0.157% after treatment.

4.4.4 N_2 sorption isotherm and BET surface area analysis

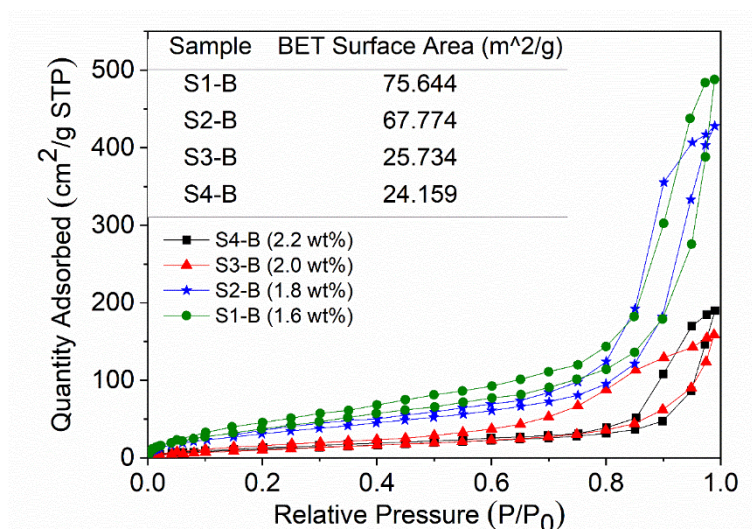


Fig. 4. 19 N₂ adsorption-desorption isotherms graphs of corresponding PLLA fibrous membranes.

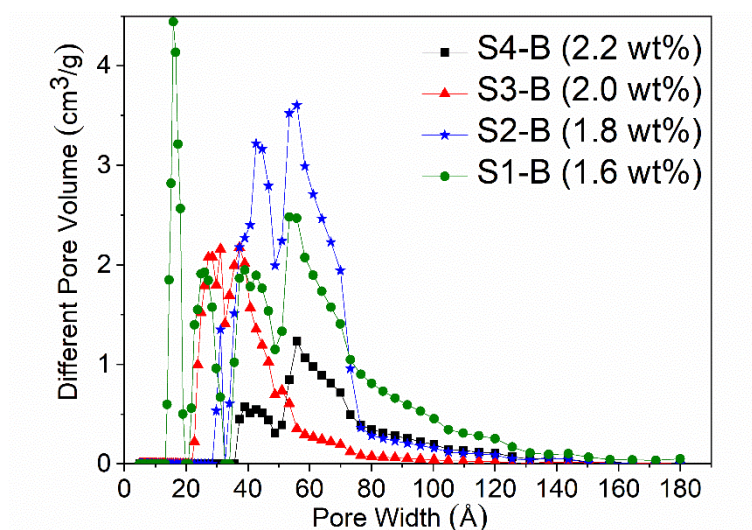


Fig. 4. 20 DFT pore size distribution curves of corresponding PLLA fibrous membranes. N₂ adsorption-desorption isotherms graphs of PLLA fibrous membranes under different concentrations from 1.6 to 2.2 w/w, identified as the typical Type IV isotherm materials.

Table 4. 3 Specific surface area (BET) for before and after acetone treatment samples.

Sample Name	Specific Surface Area (m ² /g)
Nonporous PLLA fibrous membrane	4.2±0.2
Porous PLLA fibrous membrane	75.6±0.6

N₂ sorption analysis was conducted on PLLA fibrous membranes prepared at various solute concentrations; the resulting isotherms are displayed in Fig. 4.19 & 4.20. This physical characterization method can accurately analyse microporous and mesoporous structures whose pores are less than 50 nm materials. Under IUPAC classifications [89], the N₂ adsorption-desorption isotherm graphs of PLLA fibrous membranes (Fig. 4.19) should be identified as the typical Type IV isotherm material, due to the presence of majority proportion of mesopores (2-50 nm) inside the specimens. Since similar hysteresis loops caused by capillary condensation appeared in all four curves, filling and emptying of mesopores are evident in these membranes. From the table shown in Fig. 4.19, BET surface areas decreased from 75.644 m²/g to 21.159 m²/g with the increasing of PLLA solute concentrations, but it is still a relatively high BET surface area compared with previous studies [6,7,56]. As already discussed in the results of the SEM observation, over-high solute concentration causes the squash and bond among fibres after recrystallization post-treatment, significantly reducing the specific surface area of the sample [90]. These phenomena correspond to the results reported in previous studies. Moreover, the pore size distribution of the relevant specimens was also analysed by employing the DFT method. as shown in Fig. 4.20. This illustrates that the pore size is in the range of 2-18 nm. It is observed that the sample under a solute concentration of 1.6% w/w has some pores smaller than 2 nm which can be classified as micropores. For all samples, most pores are between 2 nm and 14 nm. Furthermore, with the increase of solute concentrations, the pore size tends to increase, which corresponds to the SEM observation (Fig. 4.5).

4.4.5 Hierarchical porous structures

In addition to N₂ adsorption characterization, macroscopic porosity measurements were also performed and analyzed. The thicknesses of samples are 13.25 µm (S1-B), 14.00 µm (S2-B), 17.25 µm (S3-B) and 24.75 µm (S4-B). Based on equation (1), the porosities of these samples are 78.12%, 78.44%, 78.70%, 79.17% respectively. These

porosity values are relatively high compared with previous studies [6,7,56]. Combined with the BET and DFT analysis discussed above, these membranes show a hierarchical highly porous structure.

From all the characterization conducted above, the processing and mechanism of pore formation can be concluded and are shown in Fig. 4.11. Initially, the liquid of electrospinning dual solvent system containing DCM, DMF and PLLA is ejected by high voltage at the tip of needle. During this stage, the liquid system is homogeneous without any phase separation which is shown in Fig. 4.21(i). When the liquid system is drawn and forms fibre between the tip of needle and roller collector, the non-solvent induced spinodal phase separation (NIPS) and breath figure occur because DCM is evaporated. Fig. 4.21(ii) illustrates this polymer/non-solvent system. The non-solvent is then evaporated and only dried polymer phase remains [11]. Regarding the phase separation leading to the non-solvent (DMF) occupied some space, the channel-like gaps were distributed inside fibres after drying which is shown in Fig. 4.21(iii) [91]. These original cylindrical fibres are separated by these channel-like gaps, forming thinner fibrils and pores, which favours the permeation of organic solvent for crystallization as shown in Fig. 4.21(iv). At this stage, the polymer chains are in a random coil state, and entangled with each other. The solvent used during post-treatment, acetone, has similar solubility parameter to PLLA but limited dissolvability. While PLLA fibres are immersed in acetone, acetone entered PLLA, destroying and swelling the coil-like PLLA molecules which give free space for the movement and re-crystallisation of PLLA chains. Due to the rearrangement of polymer phases and the generation of lamellae structures, innumerable voids were generated throughout the PLLA fibre. To sum up, while electrospinning is a typical method for preparing high porosity materials, the post treatment process in this research results in a hierarchical porous nano-fibrous membrane.

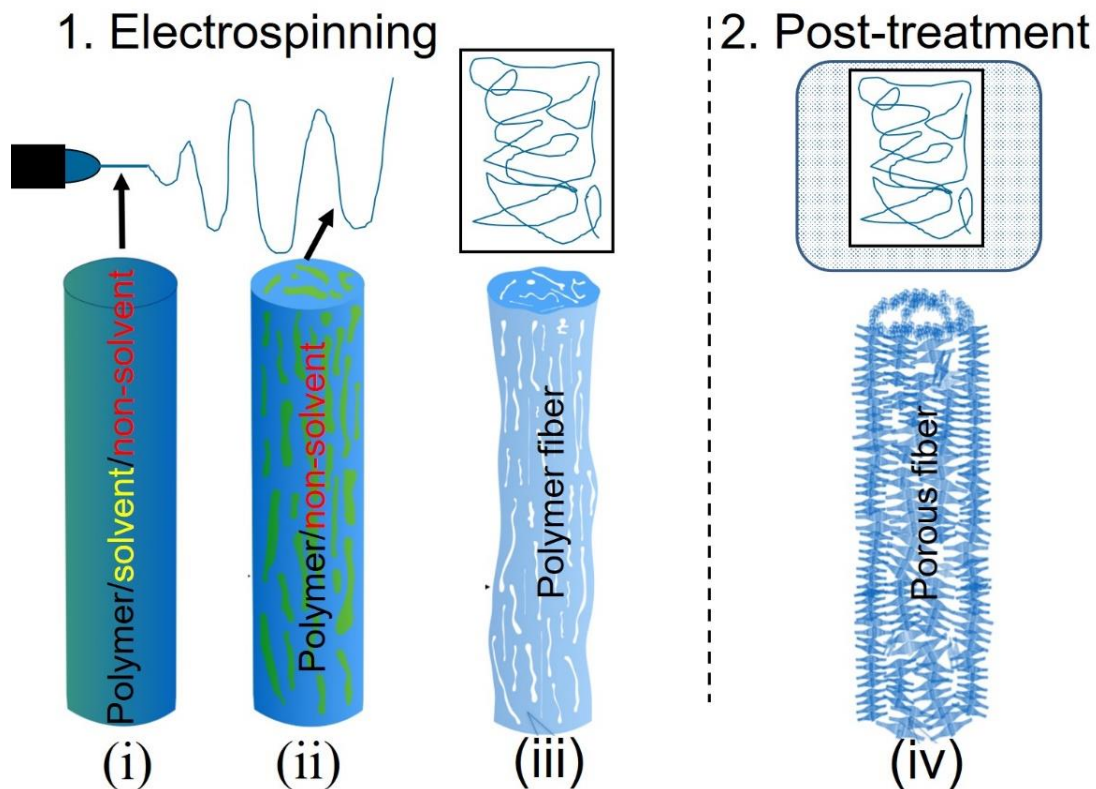


Fig. 4. 21 Structures of each stage of the electrospinning and the posttreatment process.

4.4.6 Air filtration performance

Fig. 4.22 – 4.24 illustrates the filtration efficiencies of the air filters obtained at face velocities of 7.8 cm/s, for 12 groups of membranes. The filtration efficiency of S4-C is the highest due to its smaller through-pore size which provides more opportunities to capture the NaCl aerosol particulates. Conversely, S1-A exhibited the lowest filtration efficiency due to its excessively fine fibre diameter and lighter thickness.

As the PLLA concentration and electrospinning time reached the 1.8 wt% and 90 minutes, the filtration efficiency can reach above 99.9%. Under the same test environment, the membranes with 120 minutes exceeded the filtration effect of the commercial nonwoven filter membrane (99.53%). Combined with the previous SEM and N₂ adsorption characterization results, we can conclude that the highest specific surface area itself does not bring the best air filtration effect. An optimum balance between the morphology and diffusion effect of the membrane needs to be reached.

Fig. 4.26 shows the pressure drop results. Good air permeability requires lower pressure drop [92]. Clearly, the pressure drop for S4 groups is much higher compared with S1 groups as the concentration of the PLA solution increased gradually. This can be attributed to the thicker specimen and wider fibre diameter range. In other words, samples with better filtration efficiency led to a relatively lower facilitating the penetration of air flowing across the membrane.

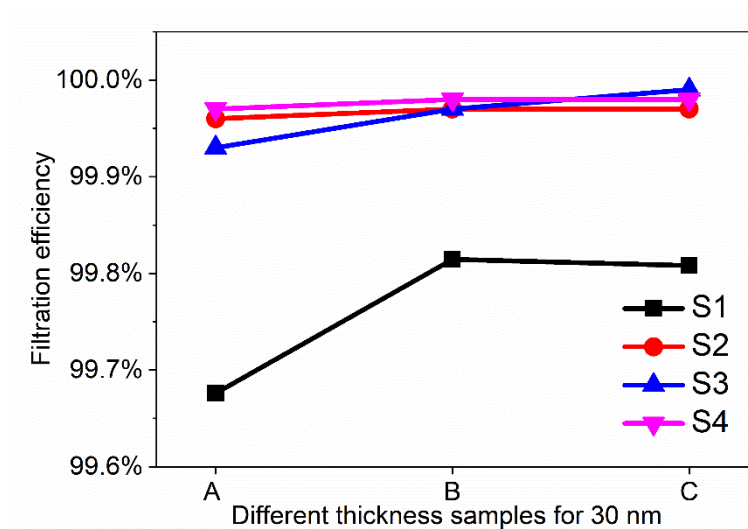


Fig. 4. 22 30 nm particles filtration efficiency of membrane samples set in Table. 3.2, with different PLLA wt%.

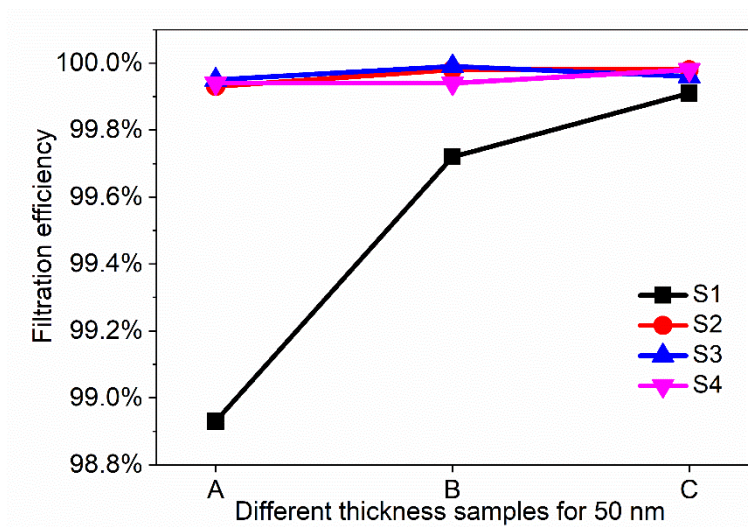


Fig. 4. 23 50 nm particles filtration efficiency of membrane samples set in Table. 3.2, with different PLLA wt%.

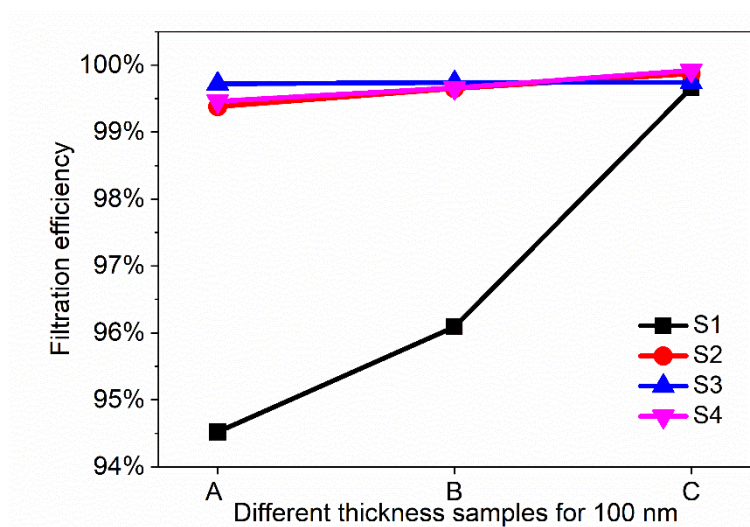


Fig. 4. 24 100 nm particles filtration efficiency of membrane samples set in Table. 3.2, with different PLLA wt%.

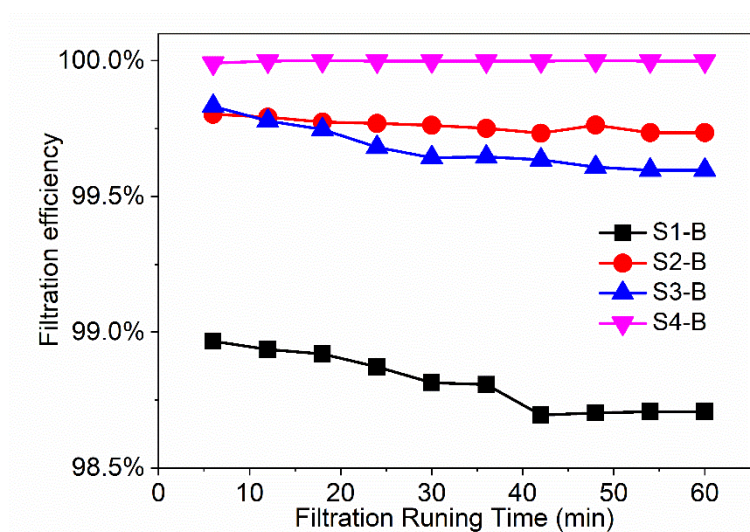


Fig. 4. 25 Filtration efficiency of membrane samples with 1-hour continuous filtering test of group B.

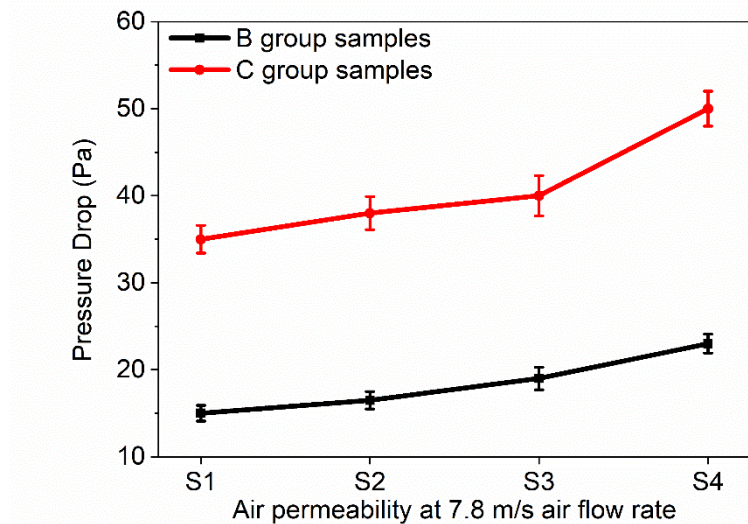


Fig. 4. 26 Pressure drop of membrane groups B and C.

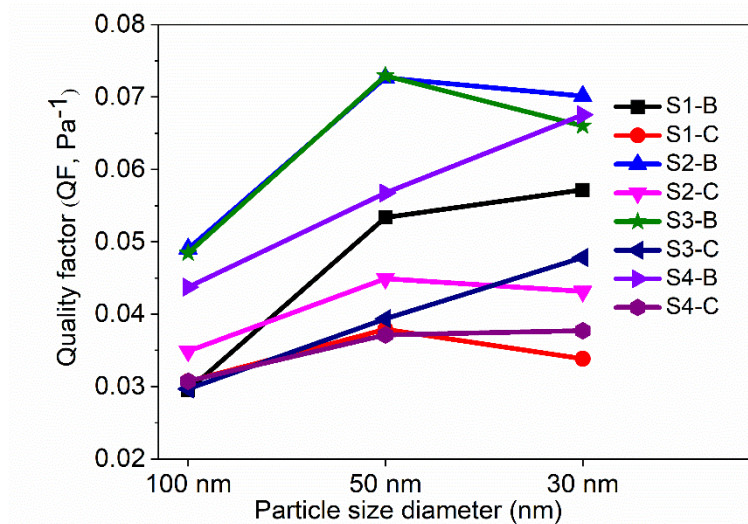


Fig. 4. 27 Quality factor (QF) of membrane samples for 30, 50 and 100 nm particle sizes.

4.4.7 Air filtration quality factor (QF)

As the ultimate indicator of quantitative analysis, QF results are shown in Fig. 4.27. Contrary to expectations, as filtering particle sizes decrease, QF of membrane becomes higher. The most likely explanation is that as the particle diameter decreases, its activity manifests mainly as random Brownian motion, while high specific surface area and high pore volume lead to more contact with aerosols, and the diffusion mechanism is

more effective.

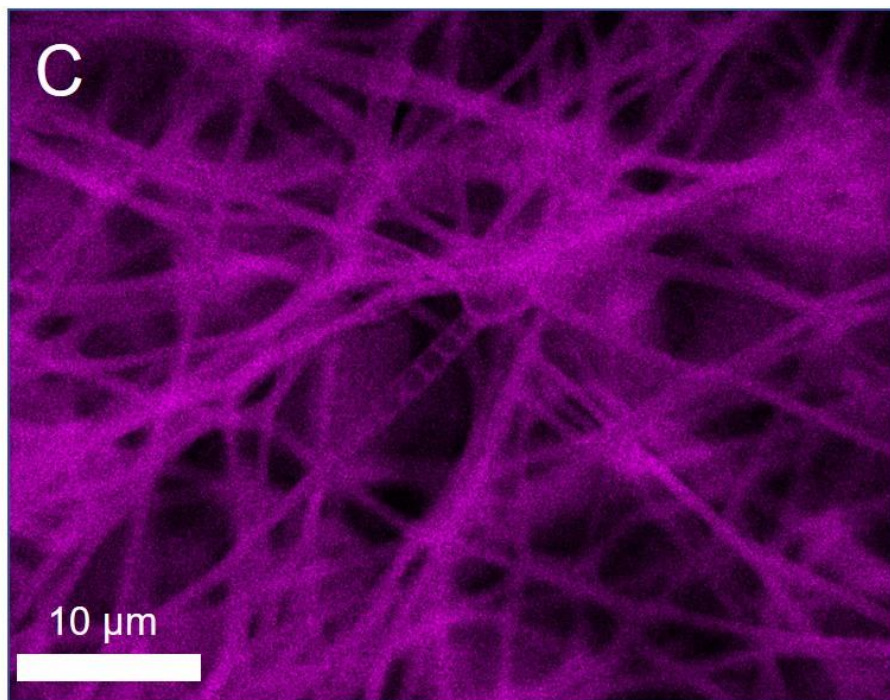


Fig. 4. 28 Energy-dispersive X-ray element mapping of the front side of the membrane after filtration testing (Carbon, C).

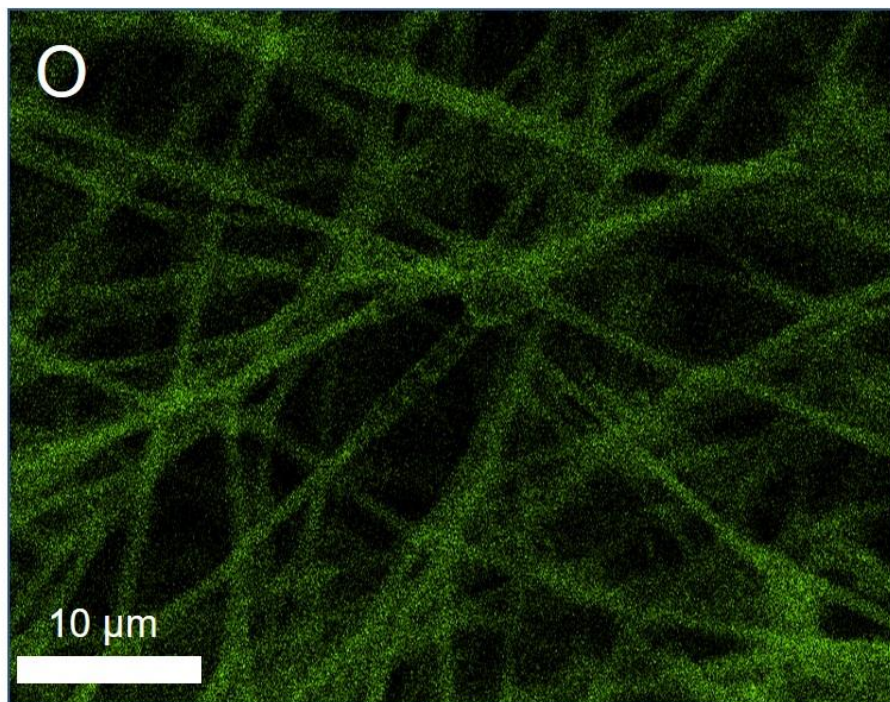


Fig. 4. 29 Energy-dispersive X-ray element mapping of the front side of the membrane after filtration testing (Oxygen, O).

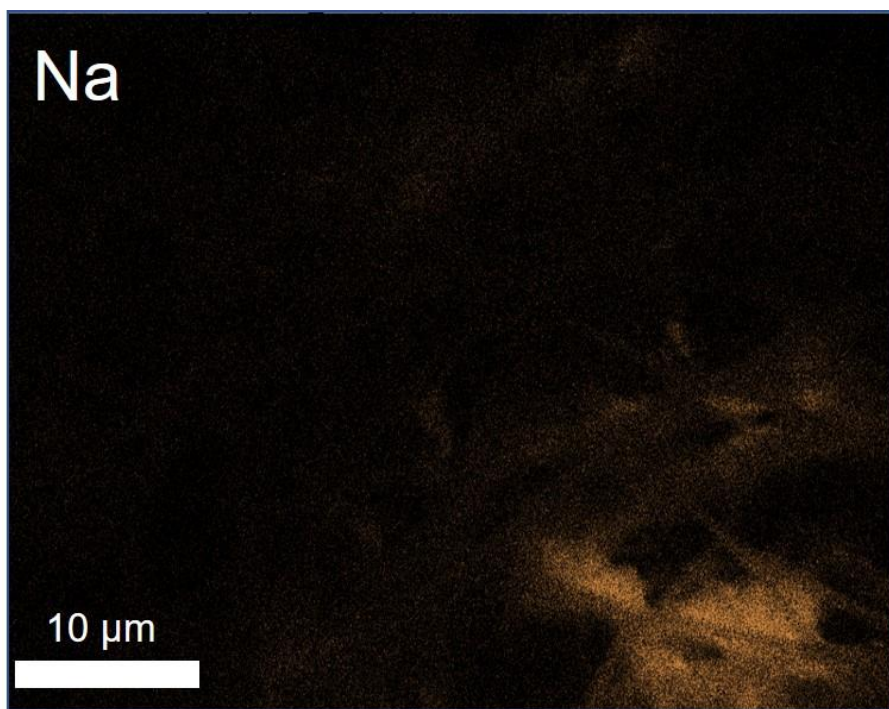


Fig. 4. 30 Energy-dispersive X-ray element mapping of the front side of the membrane after filtration testing (Sodium, Na).

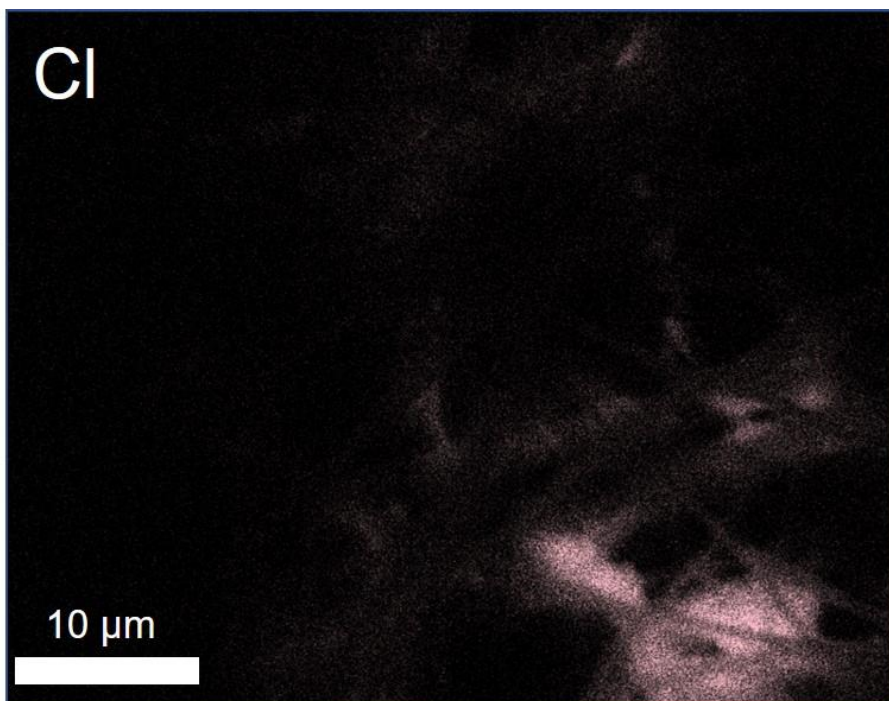


Fig. 4. 31 Energy-dispersive X-ray element mapping of the front side of the membrane after filtration testing (Chlorine, Cl).

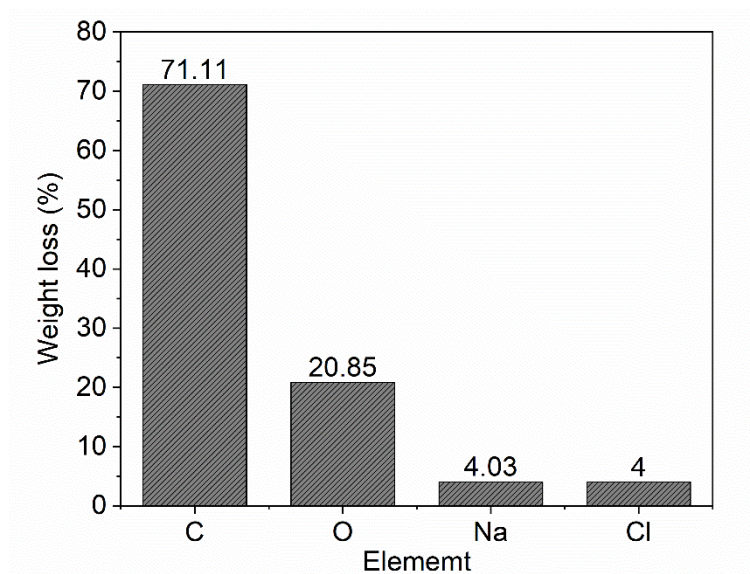


Fig. 4. 32 EDX elements distribution of front side of filtered sample.

EDX patterns strongly proved the successful filtration process, with sodium and chloride elements being detected on the surface of the membrane.

Within particle size range from 30-100 nm, salty and moist environment is highly damaging to precision instruments within large coastal and marine facilities [93]. In this study, sodium chloride was selected as the aerosol particle to investigate the main proposed application. Compared with existing coating protection, electrochemical protection, electrical insulation isolation technology, corrosion monitoring technology, and so on, the membrane material designed in this project has the characteristics of low cost, low energy consumption and small space requirement, and is suitable for ships and vessels.

Table 4. 4 Filtration efficiency of membrane samples.

Sample ID	Aerosol particles diameters		
	100 nm	50 nm	30 nm
S-1A	94.52%	98.93%	99.68%
S-1B	96.09%	99.72%	99.81%
S-1C	99.66%	99.91%	99.81%
S-2A	99.38%	99.93%	99.96%

S-2B	99.65%	99.98%	99.97%
S-2C	99.87%	99.98%	99.97%
S-3A	99.72%	99.95%	99.93%
S-3B	99.74%	99.99%	99.97%
S-3C	99.74%	99.96%	99.99%
S-4A	99.46%	99.94%	99.97%
S-4B	99.66%	99.94%	99.98%
S-4C	99.92%	99.98%	99.98%
Commercial	92.07%	99.92%	99.53%

4.5 Conclusions

In this study, electrospun PLLA fibrous porous membrane was fabricated at different concentrations and electrospinning times. As both a dual solvent system and a post-treatment applied, a significant mesopores structure can be observed in the surface of PLLA nano-fibres. Non-solvent induced phase separation (NIPS) is the main mechanism for the surface porosity of the membrane achieved in this study. Most electrospun PLLA membranes in previous studies were amorphous because of low crystallization rate and crystallinity. However, solvent induced crystallization is used in this study to achieve both higher crystallinity and blooming porous structure. By adjusting the spinning volume, the membrane thickness and porosity are controlled, and the filtering efficiency engineered consequently. The PLLA films prepared in this experiment successfully intercepted the aerosol particles while the pressure drop was kept at a reasonable level. The effect is similar to the ULPA standard, but the contaminant diameter is smaller. Because of enhanced aerosol particulate diffusion, this high specific surface area filter shows higher quality factor with the decreasing aerosol particle size. The prospective applications are primarily high efficiency filtration devices for precision instruments in harsh environments such as coastal or marine fields.

Chapter 5: Electrospun SF/PLLA Fibrous Membrane Composites towards Vascular Scaffolds

Reprinted (adapted) with permission

Jun Song, Zhongda Chen, Luis Larrea Murillo, Dexin Tang, Chen Meng, Xiangli Zhong, Tao Wang, Jiashen Li.

Hierarchical porous silk fibroin/poly(L-lactic acid) fibrous membranes towards vascular scaffolds.

International Journal of Biological Macromolecules, **2021**.

<https://doi.org/10.1016/j.ijbiomac.2020.10.266>

Copyright © 2021 Published by Elsevier B.V.

My contributions:

I have examined the parameters and prepared the silk fibroin solution and samples of PLLA/SF fibrous membranes. I also did the further characterizations except cell culture and laser confocal microscopy. I analysed all the data, drew all the figures, and wrote the manuscript solely.

5.1 Chapter Synopsis

Small diameter vascular grafts fabrication is kept as a major challenge for regenerative medicine although patients suffering from severe occluded arteries are highly demand of these tubular scaffolds to be used as a bypass or substituted conduit. Muscular artery shows a cell-specific oriented spatial structure, mimicking of this structure is a promising way for muscular artery regeneration. The work in this chapter is related with an electrospun 3D blood vessel scaffold, which mimics muscular artery tunica media architecturally and mechanically. Hierarchical porous and large fibre diameter structures could help cell grow into the tissue three-dimensionally. The electrospun Poly(L-lactic acid) (PLLA) fibrous matrices with good elastic mechanical property and hierarchical porous structures have been coupled with the coated excellent hydrophilicity cell interaction properties of silk fibroin (SF). This material fabrication object was graphically demonstrated in Fig. 5.1. In this chapter, a 40-layered SMCs structure of the tunica media was simulated by winding and stacking membrane scaffolds, and SF is a substitute of gelatine and other proteins characteristically among the layers. Despite of basic scaffold material characterization and tubular fabrication, a 14-day in vitro viability and morphology of A7r5 smooth muscle cells (SMCs) were carried out. The resulted cell adhesion rate (97%) and proliferation (64.4%) are satisfied. Additionally, either the vascular scaffolds processing methods or vascular fabrication protocol are simple and easy for mass productions. These results demonstrated that hierarchical porous PLLA/SF are promising off-the-shelf scaffolds for small diameter muscular artery regeneration.

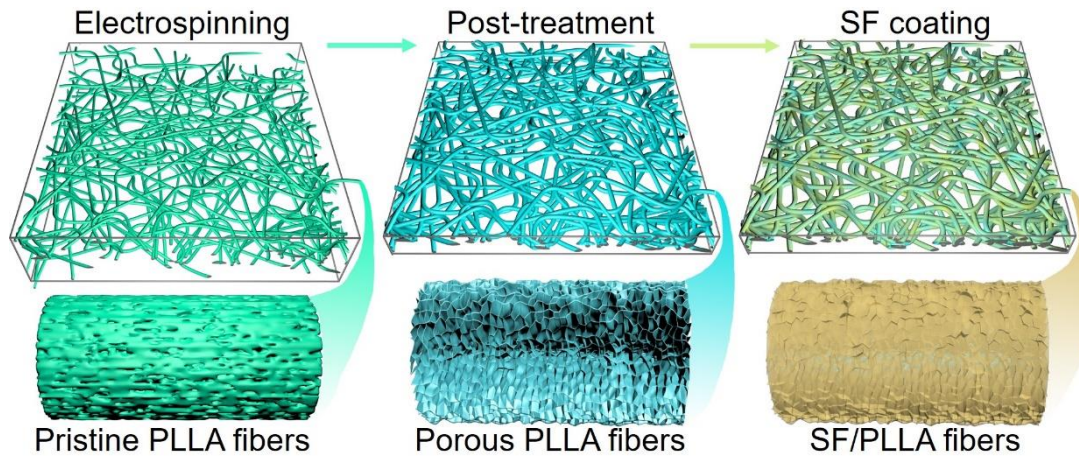


Fig. 5. 1 Schematics of the electrospun PLLA fibrous membrane, porous PLLA fibres after post-treatment and silk fibroin coating on PLLA fibres.

5.2 Literature Review: Electrospun Vascular Scaffolds

Cardiovascular diseases are the primary cause of death to the people all over the world. In a major developing country, China, this ratio is 2.96‰ in rural areas while 2.62‰ in urban areas [94]. In an emblematic developed country, the United Kingdom, as of 2019, the fatality rate of cardiovascular diseases is 0.46‰ [95]. The high cost of ischemic diseases has brought a huge economic burden to the healthcare systems and society globally. Although the autologous blood vessel is one of the solutions to severe cardiovascular diseases [96]. The low availability of autografts limits its applications [97]. As an alternative, artificial scaffolds have been widely researched and developed, especially muscular arterial tissue engineering scaffolds with small internal diameters (<6 mm) [98]. It should mimic autologous blood vessels in morphology and measure up to other biomechanical and physiological requirements via a functional scaffold. Benefiting from further differentiation of human-induced pluripotent stem cells on the artificial grafts, the in situ artificial tissue engineering strategy is possible more effective than autologous blood vessels due to reduce the post-implantation complications when they are applied in the final clinical scenario [99,100]. However, the best biomanufacturing methods for in situ tissue engineering muscle artery scaffolds

has not yet been determined. some operational and cost-effective additive manufacturing techniques (three-dimensional printing [101], freeze drying [102,103], phase separation and electrospinning) are ideal choices that could be used to manufacture tubular stents.

The electrospun fibres and subsequent fibrous scaffolds show advantages when simulating the human extracellular matrix with porosity structure, high specific surface area and elastic mechanical properties [104]. Benefitting from a porous structure in nano/micro size, the electrospun fibrous biomaterials show cytocompatibility and offer more possibilities for loading growth factors [13,52]. In the manufacture of multilayer vascular grafts, it is significant that sufficient nutrients for cells are obtained between the layers of the graft structures. To date, little effort has been made to design the framework structure specifically for tunica media. A critical strategy is to roll a piece of electrospun membrane of controlled thickness to mimic the structure of the tunica media [105]. For example, Kishida et al. electrospun a polyurethane tunica directly onto a decellularized intima media sheet medium of the artery [98].

What electrospun biomaterials should be selected is another problem that need be customized by the requirements of the scaffolds. Regenerated SF is normally dissolved in high-concentration saline solutions or mixed solution systems. Then, SF was fabricated into fibres, sponges, gels, microspheres, films, et al [106]. Despite of its excellent biodegradability and biocompatibility, SF exhibits good hydrophilicity and much better mechanical tensile property compared to most of synthetic polymers [107]. When it comes to proteins of which collagen and elastin are the major components among smooth muscle cells (SMCs) of blood vessels, SF could substitute for collagen and elastin [108]. However, it must be crosslinked to form the stable hydrophilic β -sheet scaffold, via ethanol, other crosslinking agents, or shear force treatment since SF maintains an unstable α -helical structure in water [109]. In recent years, multiple techniques have been attempted to mimic tunic media by SF based materials. For example, Alessandrino et al. made a hybrid tunica media grafts that electrospun membranes are inner and outer layers while a textile mat is the intermediate layer [108]. Faré et al. reported a small diameter vascular graft made from a crosslinked gelatin /

SF composite [110]. Mo's group used a three-step electrospinning method to fabricate a three-layer tubular graft based on fibres and threads that consisted of two kinds of proteins, collagen and SF [111]. Although the mechanical, and morphological successes were shared in these works, biocompatibility studies have proved that cells are less active and unstretched on the classical fibrous membranes' interfaces.

As mentioned above, it is common to coat SF on the surface of various components to improve the performance of the materials. For example, the polydimethylsiloxane disk could be immersed in SF solution to obtain a uniformed SF coating biomedical implant [112]. If an artificial blood vessel grafting is fabricated by a single polymer component, poly (ϵ -caprolactone), polyurethane, and PLLA were the main stream choices in the initial stage [113]. However, these synthesized polymers show disadvantages in mechanical properties, chemical modification options, and biological response, if they are compared to some natural polymers. Among them, PLLA has been widely studied as tissue engineering materials, due to its biocompatible, non-immunogenic and biodegradable properties [114]. Meanwhile, PLLA is approved as a scaffold by the US Food and Drug Administration and its counterparts already [115]. With the studies continued, pure PLLA is seldom selected as the raw material for artificial blood vessel grafting, because it has been found that pure PLLA scaffolds have some shortcomings, such as poor biomechanical property and high hydrophobicity [1]. By introducing SF into PLLA, some of the above problems could be solved. Associated with mature modification and crosslinking protocols, SF could be coated on the surface of polymeric materials to obtain a SF hierarchical porous structured fibre with tunable mechanical properties [116].

5.3 Materials and Methods

5.3.1 Materials

The sources of PLLA granules (PL 65), DCM, DMF have been stated in Chapter 3. Raw *Bombyx mori* silk was purchased from Shengzhou Xiehe Silk Co. Ltd, Zhejiang,

P. R. China. Phosphate buffered saline (PBS), Dulbecco's modified eagle medium (DMEM) and diamidino-2-phenylindole (DAPI) fluorescent stain were purchased from Sigma-Aldrich, USA. Acetone (99%, Alfa Aesar), ethanol (99%, Alfa Aesar), sodium carbonate (99.8%, Alfa Aesar), LiBr (99%, Alfa Aesar) and Alamar blue cell viability reagent (Invitrogen) were purchased from Thermo Fisher, USA. A7r5 rat smooth muscle cell (SMC) line was purchased as CRL-1444 from ATCC, USA.

5.3.2 Preparation of SF solution

As is shown in Fig. 5.2B, the SF solution was prepared by a well-known method from raw silk [31]. Firstly, natural *Bombyx mori* silk was degummed under the aqueous solution of sodium carbonate (0.2% w/w) at 100°C for 0.5 hour to remove sericin and obtain fibroin. The degummed raw SF fibres were hand washed twice by distilled water smoothly for the purpose of ions removal. Then, the SF was dried in fume board for 12 hours. The degummed SF were dissolved in 9.3 M LiBr aqueous solution what the ratio of SF to LiBr solution is 1.0 g: 4.0 ml. This SF/LiBr thick mixture was kept in an oven at 60°C for 4 hours while it was stirred mildly once per hour for a uniformed dissolve. For removing lithium ions and bromine ions, the SF/LiBr mixture was poured into a semi-permeable cellulose membrane (molecular weight cut-off 12,000-14,000, SERVAPOR, Germany) for dialysing that lasts at least 3 days. The deionized water for dialysis was changed every 6 h under the room temperature. Finally, the SF solution was filtrated and centrifuged twice with the speed of 9000 rpm for 20 minutes. Different SF concentration solutions could be obtained by further processing.

5.3.3 SF coating on PLLA fibrous membrane

As is shown in Fig. 5.2A, the preparation steps for PLLA fibrous membrane mentioned in this chapter is totally same as of Chapter 3. Both pristine and post-treated membrane samples were used in this study which are displayed in Fig. 5.1. But the PLLA volume in the electrospinning solution was mixed as 2 wt% concentration. And the electrospinning time was set for 2 hours.

It is obvious that SF concentration is one of the most signification parameters in

this study. In the early stage, SF solutions with different concentrations (0.3%, 1% and 3% w/w) were mixed with ethanol (SF : EtOH=2 : 1 v/v) for investigating best coating concentration. Before SF coating, PLLA fibrous membrane was immersed in ethanol firstly, and then washed by DI water completely. Then, 1.5 mL SF solution was coated uniformly onto a piece of wet PLLA fibrous membrane ($10 \times 10 \text{ cm}^2$). SF solution was dropped in petri dish and dried in a fume board to obtain a pure SF membrane for further testing. Ethanol was used for two reasons: infiltrate PLLA, and cross link SF. When the silk fibroin aqueous solution was applied to coat/modify porous PLLA fibres, the ethanol was used to infiltrate hydrophobic PLLA membranes. Ethanol is a traditional cross-linker for silk fibroin molecules. Due to pure silk fibroin is highly water soluble, so the ethanol, as a crosslinker, is used to make SF more stable in vitro and future works.

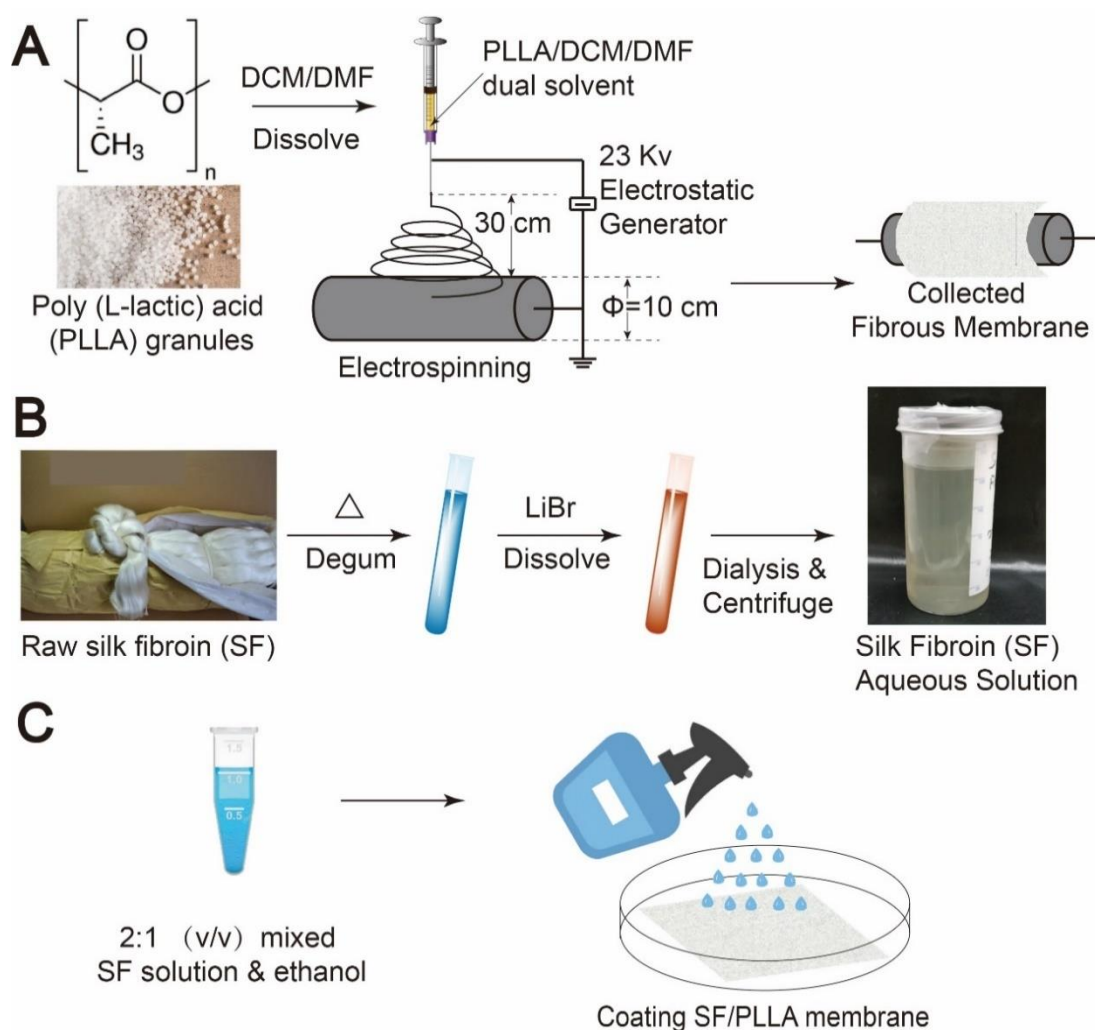


Fig. 5. 2 Schematics of the materials fabrication methods. (A) electrospinning PLLA

fibrous membrane; (B) SF solution preparation; (C) coating; and (D) spraying processing methods.

Furthermore, two coating protocols were also designed and conducted in this study. For coating and spraying SF, the PLLA membrane was immersed in ethanol as the early stage did. Then, prepared 1% SF solutions was mixed with ethanol (SF: EtOH = 2:1 by w/w). Upon SF/H₂O/EtOH solution prepared, this liquid was used to dip coat or sprayed by a 20-ml spray bottle (VWR, UK) by as shown in Fig. 5.2C, D. The 1.5 ml solution was coated or sprayed onto the surface of a 10 × 10 cm² (12 mg) PLLA fibrous membrane as aforementioned protocol.

5.3.4 Material characterizations

For the surface morphology of fibrous membranes, scanning electron microscopy (SEM) characterization for scaffolds were undertaken by Ultra 55 FE-SEM (Zeiss, Germany) with the field emission gun at 1.5 kV after gold coating. The specimens after cell culture were also characterized by Quanta 250 (FEI, Thermo Fisher, USA) SEM. Before observing scaffolds with cells, graded dehydration by ethanol were undertaken. In general, each sample was immersed into 30%, 50%, 70%, 80%, 90% ethanol aqueous solution (v/v), and 100% ethanol twice for 20 min each time, successively. Then, the specimens were kept in vacuum drier overnight before characterization.

An optical contact angle meter system (Krüss Optronic DSA100, Germany) was used to calculate water contact angle (WCA) by the sessile drop method, with a controlled 20 µL of water per drop. The contact angle between membrane's surface and water was recorded by camera in the 2nd second of water contacting with membrane.

The samples were cut into 5 × 47 mm² shapes for tensile tests in a static tensile machine (Instron 3344, MA USA) equipped with a 10 Newton cell load and a deforming rate of 5 mm/min. Based on the recorded stress/strain curves, Young's module and tensile strength were obtained. Five samples in each group of membranes were performed for tensile and WCA wettability characterization. The N₂ adsorption-

desorption test was undertaken to characterize Brunauer-Emmett-Teller (BET) specific surface area of each group samples via a Gemini 2360 Surface Area Analyser (Micromeritics, USA).

Samples from pristine PLLA fibres, porous fibres, SF/PLLA fibres and pure SF were characterized by X-ray diffraction (XRD), X-ray photoelectron spectroscopy (XPS), Raman and Fourier transform infrared spectrometer (FTIR). XRD was scanned via a X'Pert Pro's X-ray diffractometer (Panalytical, UK) with reflection mode Cu-K α radiation and employing a scanning rate of 2 °/min in a 2 θ range from 10 ° to 30 °. XPS was conducted by Kratos Axis Ultra Hybrid (Shimadzu, Japan) photoelectron spectroscopy. Raman spectra were acquired with a LabRAM Evolution Raman Spectrometer (Horiba, Japan) with a 50 \times objective and 633 nm laser at a power below 2 mW to avoid excessive thermal damage of fibroin and polymer. FTIR data were recorded at room temperature by a Fourier transform infrared spectrometer (Nicolet 5700, USA) on reflection mode.

5.3.5 Vascular grafts fabrication

For fabricating the vascular grafts, a piece of membrane (100 \times 300 mm², 18 μ m in thickness) was rolled up around a glass rod. Upon being rolled, a 160°C soldering iron was closed to, but not touched, the tube as a thermoforming processing. For further characterization, frozen sections in a cryostat (CM3050s, Leica Biosystem UK Ltd., UK) was used to get cross-section samples of vascular grafts.

5.3.6 SMCs in vitro study

A7R5 Cells were cultured with 12-15 mL of high glucose DMEM supplemented with 10% fetal bovine serum, 1% L-glutamine and 1% Penicillin-Streptomycin in T75 flasks seeded at a density of 2.5 \times 10⁶ cells per flask. Cells were maintained at 37°C in a humidified air incubator containing carbon dioxide (5%). When cells reached \approx 90-100% confluency, they were trypsinized, harvested, washed, and seeded onto 12-well plates. Membranous samples were first pre-conditioned with supplemented DMEM by incubating at 37°C for 4-6 hours prior to seeding cells [117]. Subsequently,

disassociated cells were re-suspended in DMEM and 70 μ L of cell suspensions were seeded onto the surface of membrane samples. After a 2-hour incubation, 1.5 mL cell culture medium was added for further growth in each well. Cell seeding density was approximately 1.5×10^5 cells per well for 3 groups PLLA/SF membrane samples, the glass slides and empty wells for control. Metabolic activity of living cells of each cell-laden membrane was determined by Alamar blue assay according to the manufacturer's instructions (DAL1025, Invitrogen). The cells were incubated for 2 h at 37°C with carbon dioxide (5%). Aliquots (100 μ L) of the culture medium were transferred to 96-well plates for the determination of fluorescence intensity with a micro plate reader (FLUOstar Omega, BMG, Germany) using an excitation wavelength of 570 nm and an emission wavelength of 600 nm. Cell counts were conducted in a C-Chip disposable hemocytometer (NanoEnTek, Korea) by a Countess II automated cell counter (Life technologies, CA USA). Cell morphology was monitored by a phase contrast light microscopy (Jena, Zeiss, Germany). DAPI (D9542, Sigma-Aldrich, Germany) and Phalloidin (ab176753, Abcam, UK) were used to stain cells on the membrane at 1 : 100 dilutions. Then, the morphology of cell membrane and filamentous (F-actin) on the surface of 4 groups of membranes were observed by a multiphoton microscope (Leica SP8X, Leica Biosystem UK Ltd., UK) at three time points (day 1, 4 and 7).

5.3.7 Statistics

Fibre diameter, cell density and cell size results were calculated via ImageJ (NIH, USA). Tensile, WCA and cell work results were expressed as means \pm standard deviations. Statistical differences between samples were evaluated by Student's t-test in Origin software (9.0) using the least significant difference (LSD). Differences were considered significant when $p < 0.05$ and very significant when $p < 0.01$, ultra-significant when $p < 0.001$.

5.4 Results and Discussions

5.4.1 Surface morphology

As the Section 4.3.3 stated, the concentrations of SF solutions directly related to the quantity of SF left on PLLA fibres, if the volume of SF coating solution was fixed. So, SF solutions with three different concentrations (0.3%, 1%, and 3%) were prepared and coated on PLLA fibrous membranes during preliminary experiments. For the highest concentration of SF solution (3%), not only PLLA fibres were completely coated by SF, but also the interior space of PLLA membrane was also occupied by SF (Fig. 5.7 & 5.8). While the concentration was too low (0.3%), only part of PLLA fibres was covered by SF (Fig. 5.3 & 5.4), which was not enough for cell culturing. With a suitable concentration of SF solution (1%), PLLA fibres were totally covered with SF while the overall porosity of PLLA membrane was kept (Fig. 5.5 & 5.6). More importantly, SF coating on PLLA fibres still kept a highly porous structure which was much rougher than the traditional SF electrospinning film.

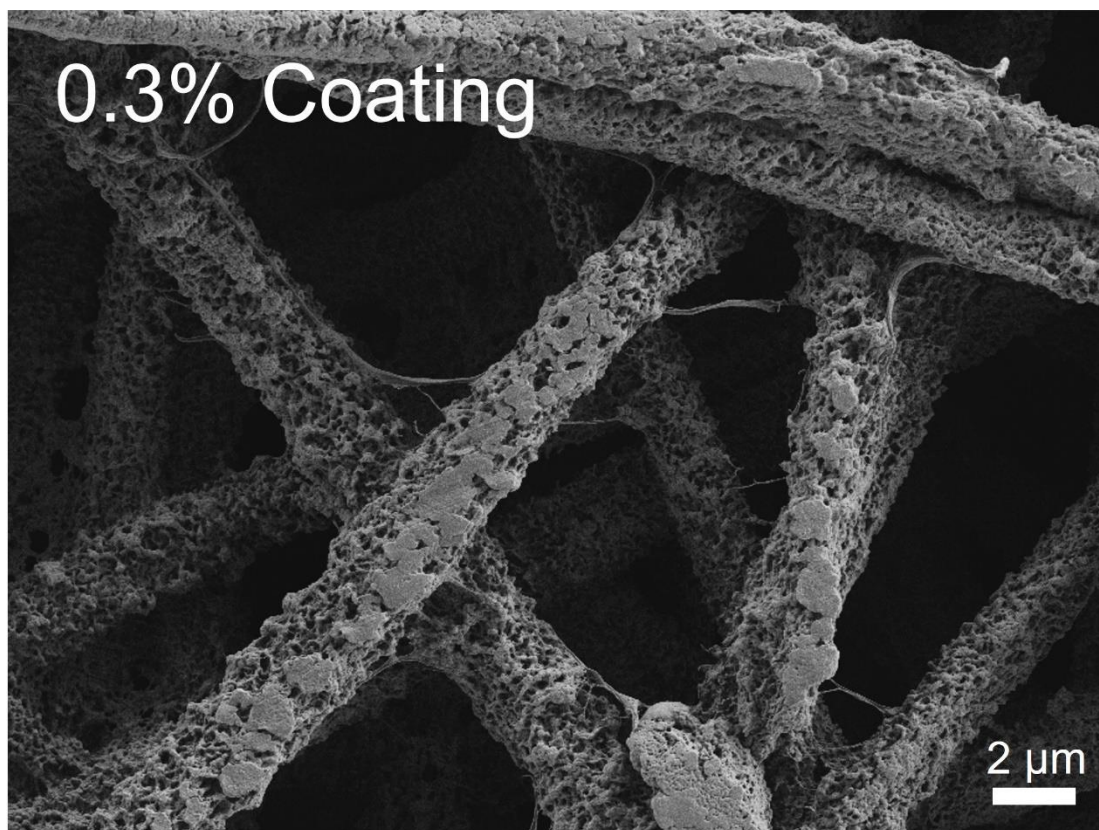


Fig. 5. 3 SEM image of 0.3% SF coated porous PLLA fibre diameter.

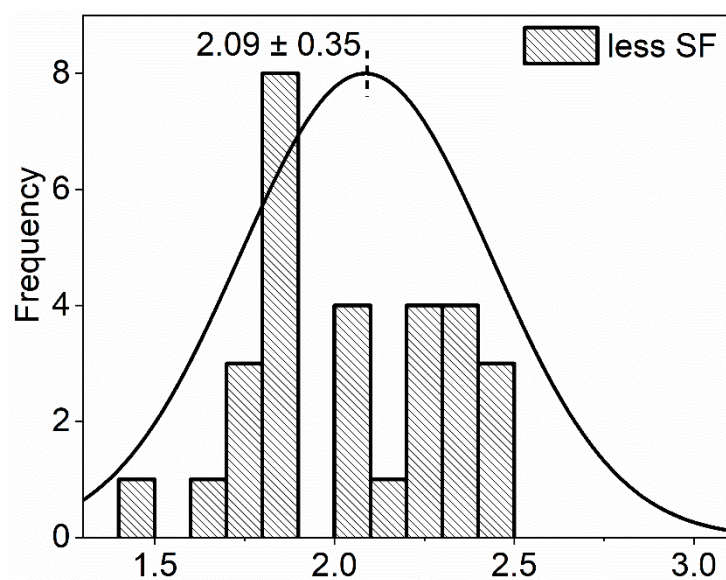


Fig. 5. 4 The counts of 0.3% SF coated porous PLLA fibre diameter.

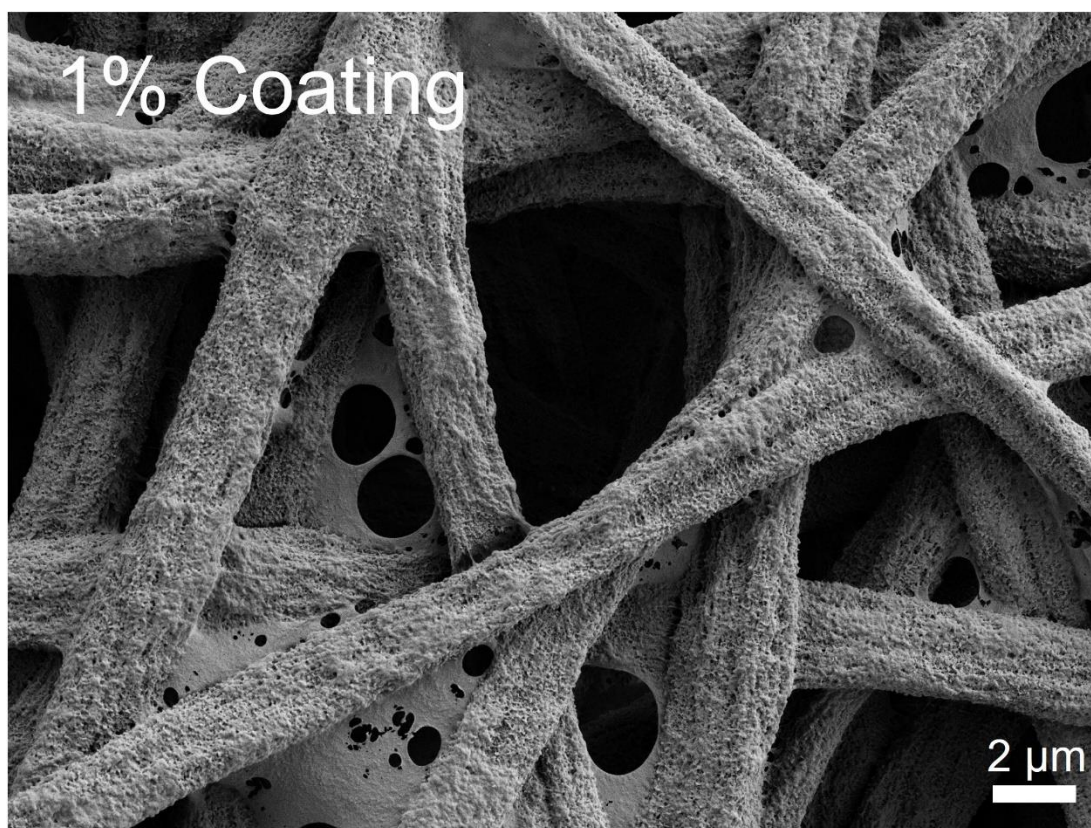


Fig. 5. 5 SEM image of 1% SF coated porous PLLA fibre diameter.

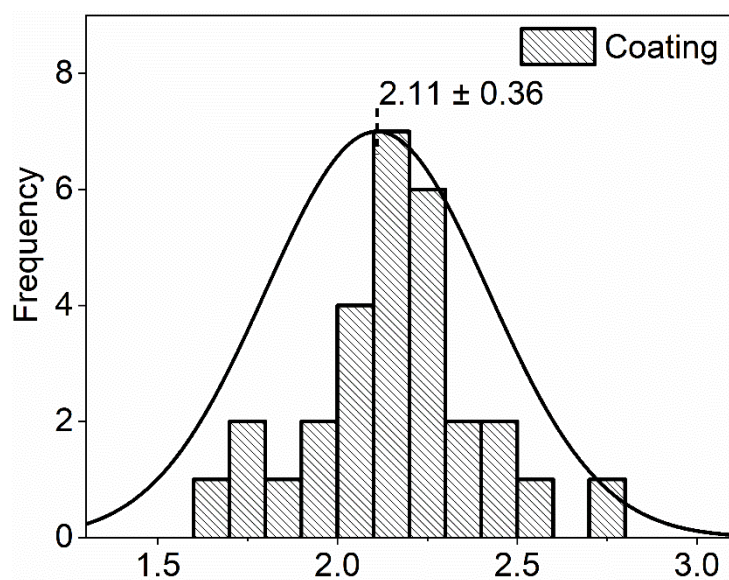


Fig. 5. 6 The counts of 1% SF coated porous PLLA fibre diameter.

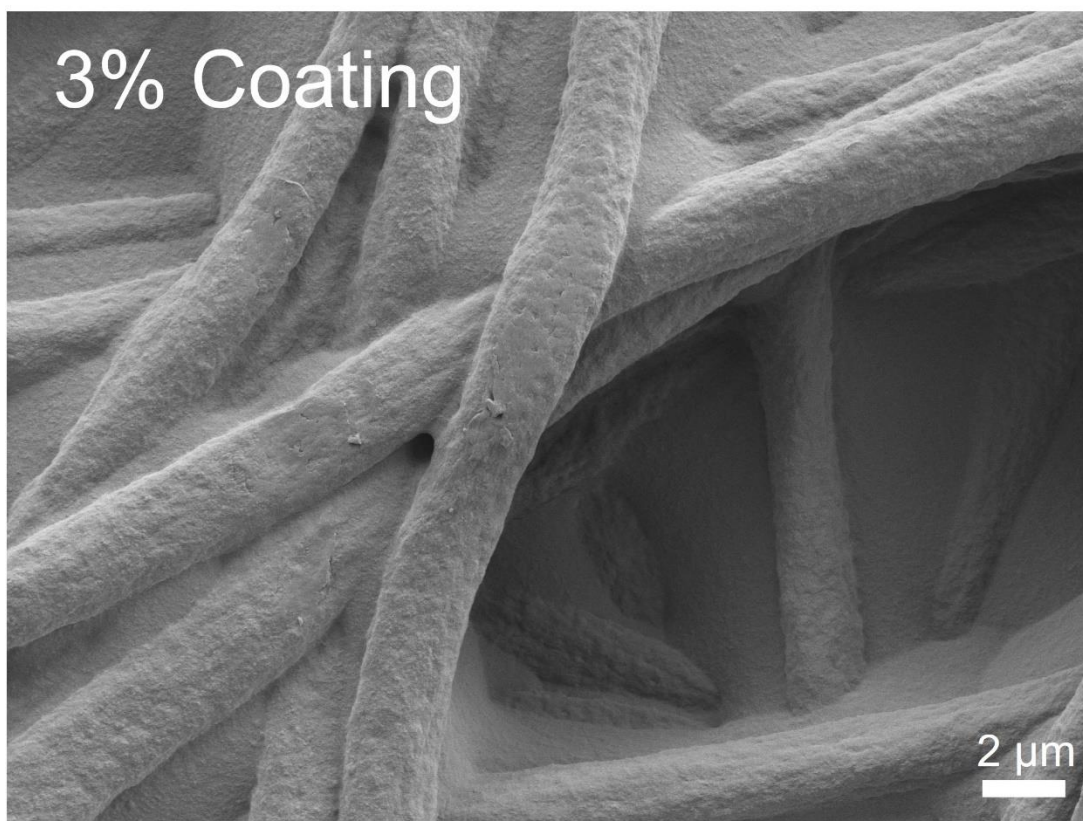


Fig. 5. 7 SEM image of 3% SF coated porous PLLA fibre diameter.

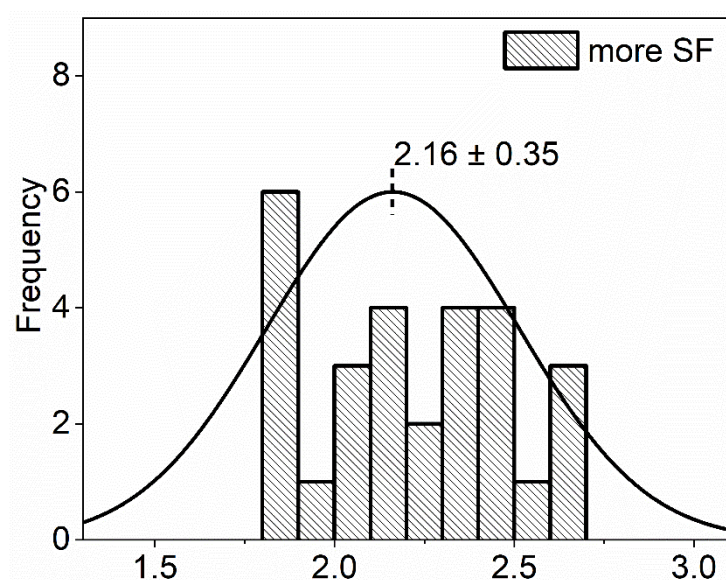


Fig. 5. 8 The counts of 3% SF coated porous PLLA fibre diameter.

After the SF concentration parameters were detected. The Fig. 5.9-12 displays the difference in morphology among pristine and porous PLLA fibrous membranes, the coating PLLA/SF membrane (C), and the spraying PLLA/SF membrane (S) at different

magnifications. As shown at the top left, smooth electrospun PLLA fibres with some pits covering the surface are not difficult to obtain by applying DCM as a solvent and mixed with some non-solvent (DMF). Previous studies demonstrated the development of these porous PLLA fibres in the past decades. The fabrication mechanisms of this electrospun PLLA fibre were concluded as NIPS induced breath figure and evaporation induced phase separation among polymer, solvent, and bad solvent during the electrospinning process. However, this study was involved into another solvent, acetone, to recrystallize PLLA fibres into a larger pore structure as a post electrospinning treatment. Only when this post-treatment is conducted, can the sample be called as a hierarchical porous PLLA fibrous membrane. At the Fig. 5.10, it can be seen that the porous fibres became quite rough. The originally smooth fibre formed a large number of open pores and was layered on the surface, which made the porous fibrous membrane looked like it was blossoming. This is the morphology of an ideal multi-level pore structure.

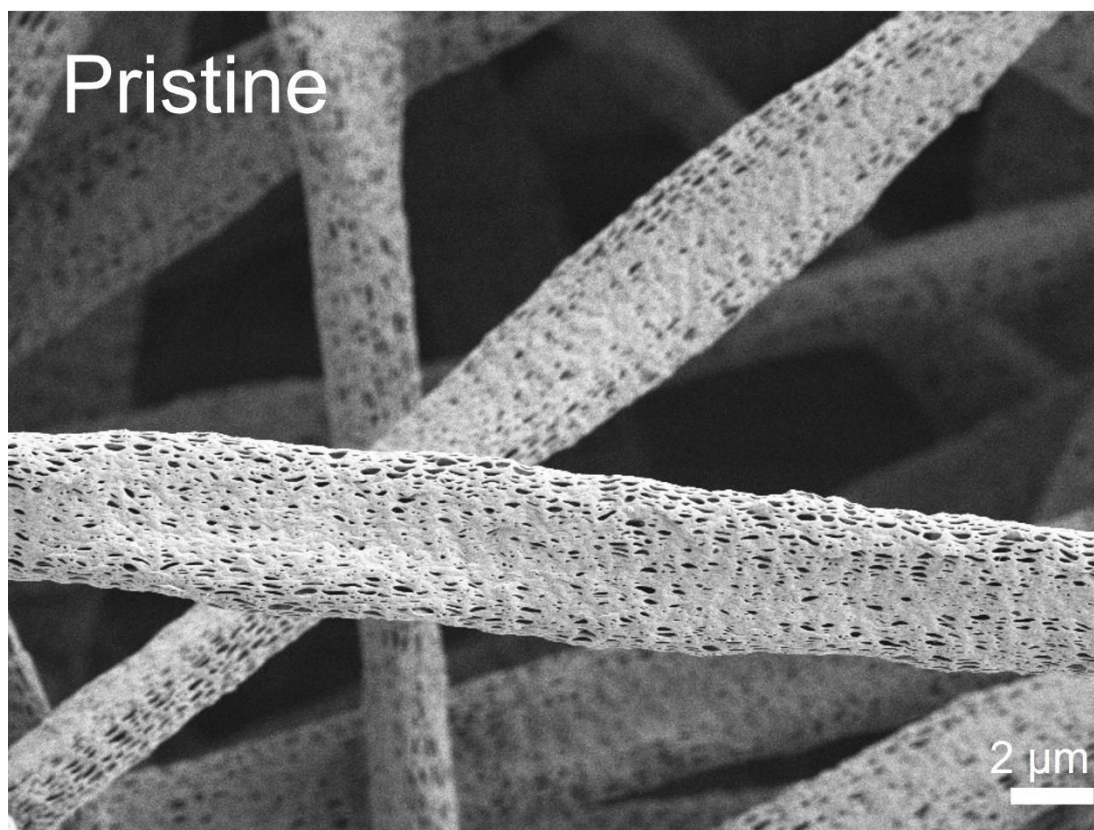


Fig. 5. 9 SEM image of pristine PLLA membrane.

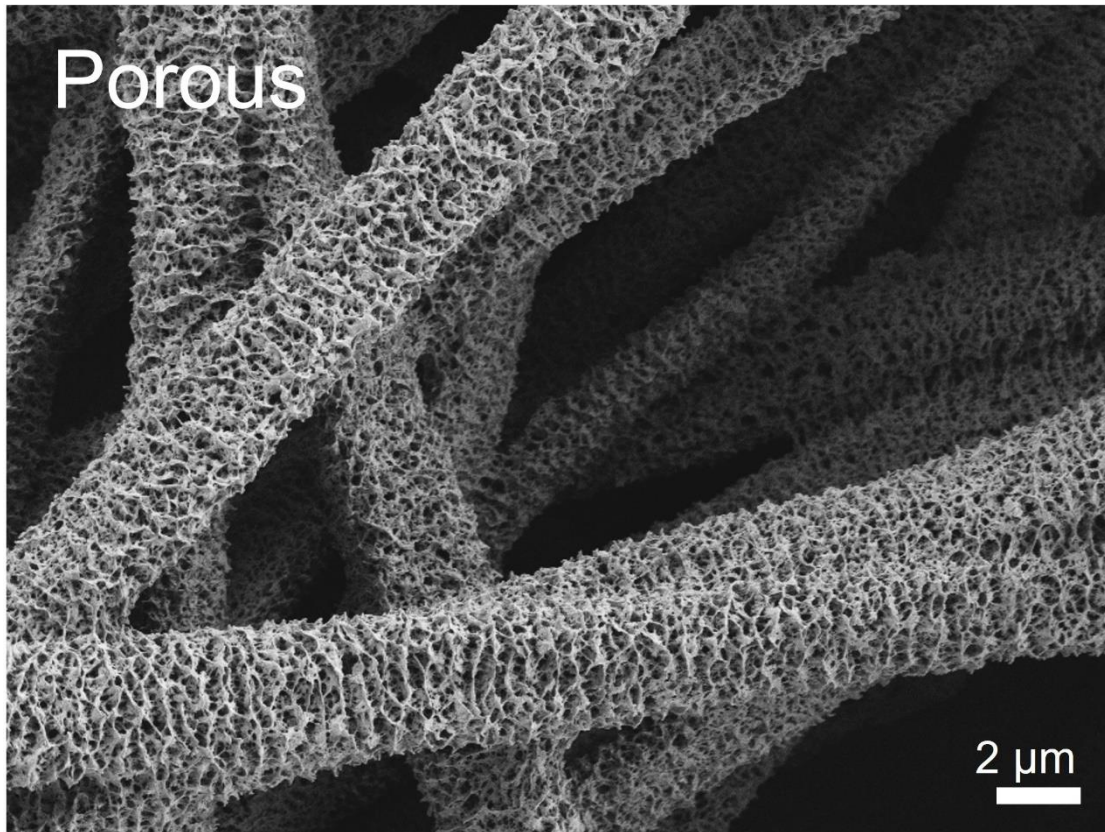


Fig. 5. 10 SEM image of porous PLLA membrane.

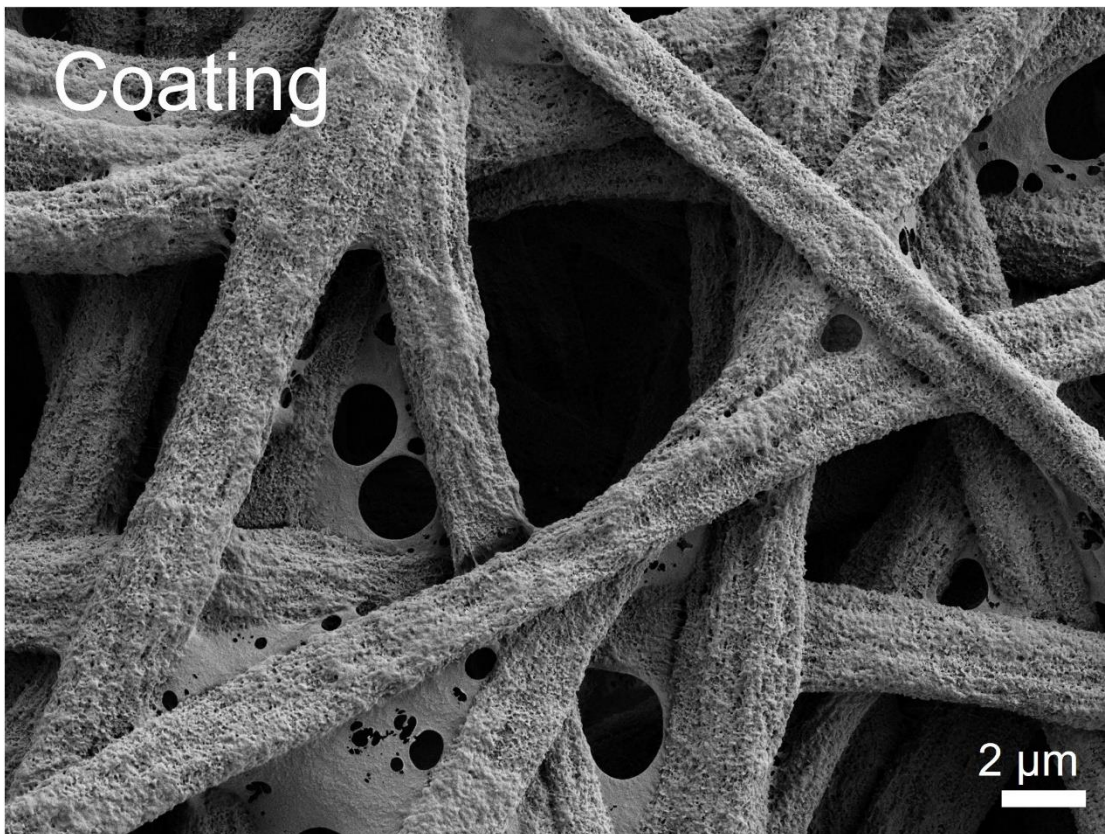


Fig. 5. 11 SEM image of porous membrane coating SF.

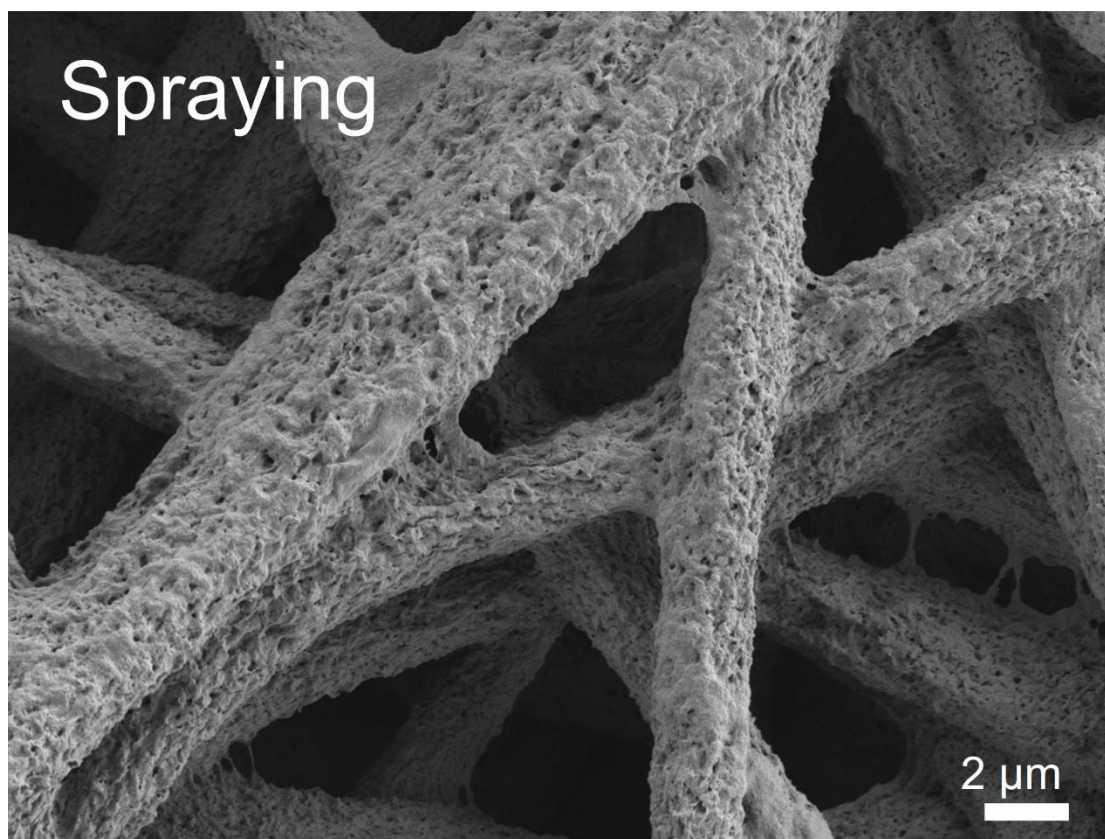


Fig. 5. 12 SEM image of porous membrane spraying SF.

In Fig. 5.11, the coated PLLA/SF film is shown. It can be seen that the surface is completely covered with a large amount of SF, which basically loses the porous morphology, but is still rougher than the traditional SF electrospinning film. Meanwhile, the diameter of SF/PLLA fibres was slightly increased from 2.08 μm to 2.11 μm . Not only that, due to the non-uniform coating, we can see that a large amount of SF remains among the intervals and the holes between the fibres, forming a film. In Fig. 5.12, the high multiples of the spraying PLLA/SF samples are shown. The SF mists in spraying sample were covered on the surface of PLLA fibres uniformly and thinly, and an obvious porous structure was preserved, realizing experimental purpose of forming PLLA fibres as substrates to form porous fibrous SF membranes.

The N_2 adsorption-desorption experiment and BET surface area analysis is another most important characterization for investigating mesoporous materials. The BET specific surface area of pristine membrane sample ($15.34 \pm 2.49 \text{ m}^2/\text{g}$) was similar with normal electrospun sub-micro fibres. The specific surface area of porous PLLA fibres

($117.31 \pm 0.79 \text{ m}^2/\text{g}$) was increased dramatically compared with pristine fibrous membrane. After porous PLLA fibres were covered by SF, their specific surface area decreased to $58.93 \pm 2.41 \text{ m}^2/\text{g}$. Even so, SF/PLLA still had much higher surface area than traditional electrospun fibres reported before.

5.4.2 Characterization and material properties of membrane samples

XPS survey is a powerful method could be used to investigate elemental content changes of PLLA membrane post-treatment and SF coating/spraying processing.

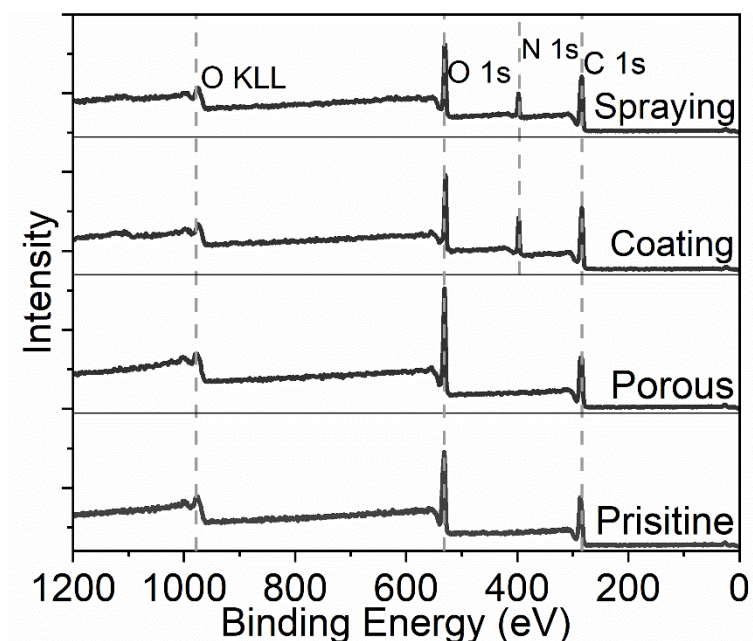


Fig. 5. 13 XPS survey of pristine and porous PLLA fibres, SF coating/spraying specimens.

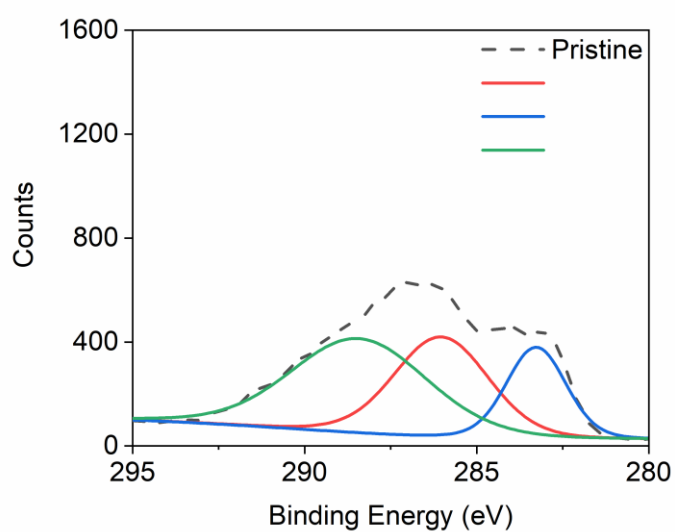


Fig. 5. 14 XPS fine peak spectral lines of carbon atoms for pristine PLLA fibres.

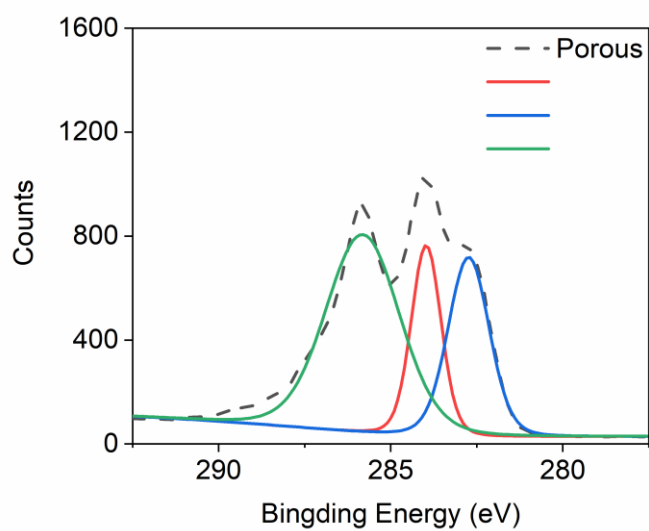


Fig. 5. 15 XPS fine peak spectral lines of carbon atoms for porous PLLA fibres.

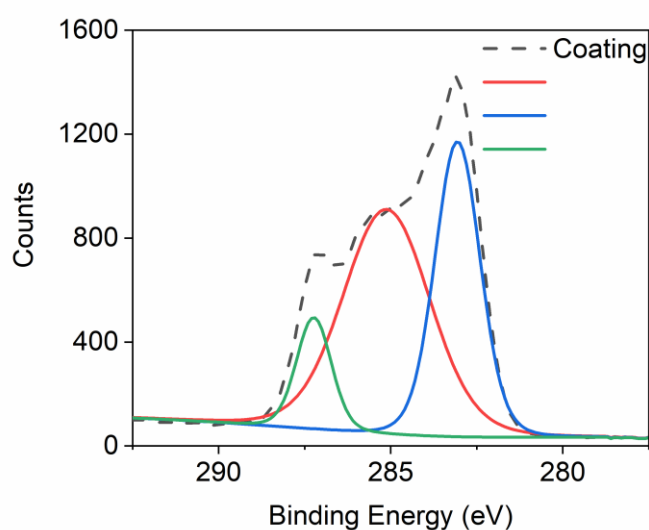


Fig. 5. 16 XPS fine peak spectral lines of carbon atoms for porous PLLA fibres with SF coating.

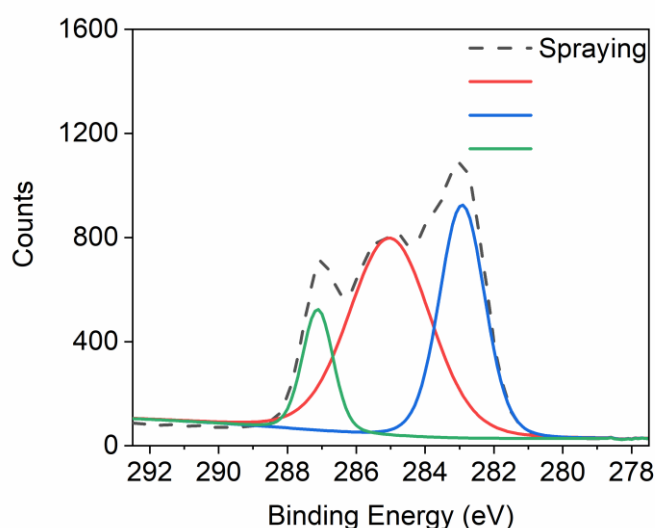


Fig. 5. 17 XPS fine peak spectral lines of carbon atoms for porous PLLA fibres with SF spraying.

As is shown in Fig. 5.13, the XPS survey is used to investigate elemental content changes of PLLA membrane post-treatment and SF coating/spraying processing. In most cases, people are not only concerned about the price of an element on the surface, but also the chemical shift of the surface element of the samples before and after the treatment. The change of the surface is used to explain the chemical state of the samples. As PLLA is a polymer, it can only be observed O 1s (532 eV) and C 1s (284 eV) peaks

in pure PLLA fibrous membrane. The difference between non-porous and porous samples are mainly reflected in the counts of the energy which could be observed in Fig. 5.14 & 5.15, the fine spectra of carbon atoms. Although nitrogen atoms could be detected in SF coated/sprayed samples whereas the pure PLLA samples only have carbon, oxygen, and hydrogen atoms as Fig. 5.16 & 5.17 shown. Carbon atom peaks were resolved to three peaks of binding energy in all four group. The binding energy of 288 eV is assign to double bond between carbon and oxygen ($C=O$, green lines in Fig. 5.14 - 17) and the binding energy of 284.5 eV is assign to the carbon-carbon bond ($C-C$, blue lines in Fig. 5.14 – 4.17) [118]. The bonds between carbon to oxygen or nitrogen ($C-N$ or $C-O$, red lines in Fig. 5. 14 – 4.17) are correspond to the binding energy in 286 eV. The intensity of carbon peak has a significant increase after the acetone induced PLLA recrystallization happened. Also, it could be seen that the relative intensity of three peaks changed after SF involved into PLLA samples. For SF modified samples, N 1s (398 eV) peak can be detected (Fig. 5.18) [119]. The coating samples show a stronger signal than that of spraying. It could be attribute to that SF are more agglomerate in the holes among PLLA fibres. Further, weak O KLL type peaks (983 eV) in an Auger spectrum can also be observed for all group samples [120].

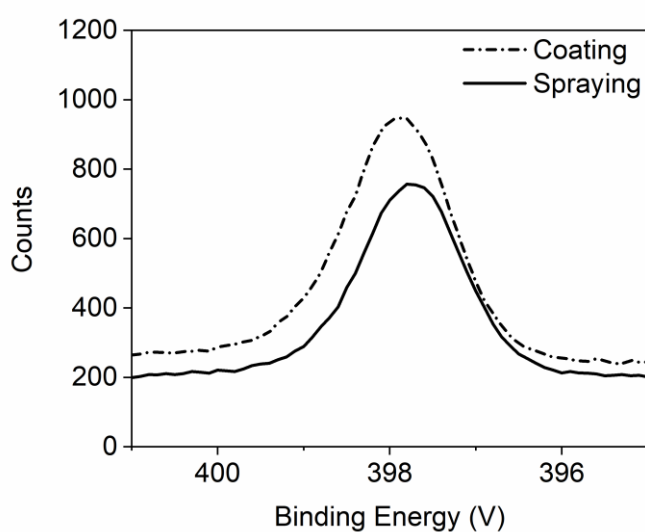


Fig. 5. 18 XPS fine peak spectral lines of nitrogen (N) atoms for porous PLLA fibres with SF coating and spraying specimens.

XRD characterization is vital in this research, due to its capability of identifying crystalline phases and determining structural properties. XRD patterns were shown in Fig. 5.19. First, it can be confirmed that the non-porous sample is in an amorphous state. For porous sample, an intense peak which centred at 16.99° (d-spacing = 0.52 nm., FWHM = 0.55°) should be referred to (200)/(110) plane of crystallized PLLA [121]. This means post-treated PLLA is highly crystalized. After SF modification, the patterns of coating and spraying sample still keep most of diffraction peaks with that of porous sample. But the most intensive peaks, 16.86° for coating and 16.87° for spraying, move towards a lower diffraction angle and narrow simultaneously. This is due to the presence of silk II's major peak (16.70°) combined together with the PLLA's peak. In addition, the d-spacing (0.54, 0.53 nm) and FWHM (0.39 , 0.52°) for coating and spraying respectively also support this result. As for the crystallinity of coating, which is higher than that of spraying, this is due to the SF agglomeration on the surface of sample coating, which shows a stronger diffraction peak. Typical diffraction peaks for cross-linked SF are located at 16.7 , 20.7 and 33.3° . It can also be observed that the 16.7° and means SF in these two samples are effectively cross-linked to the β -sheet [122]. Furthermore, XRD has an advantage when compare with FT-IR and Raman. XRD can observe SF's α -coil conformation which should located in 11.95° . This peak was found in neither sample coating nor spraying.

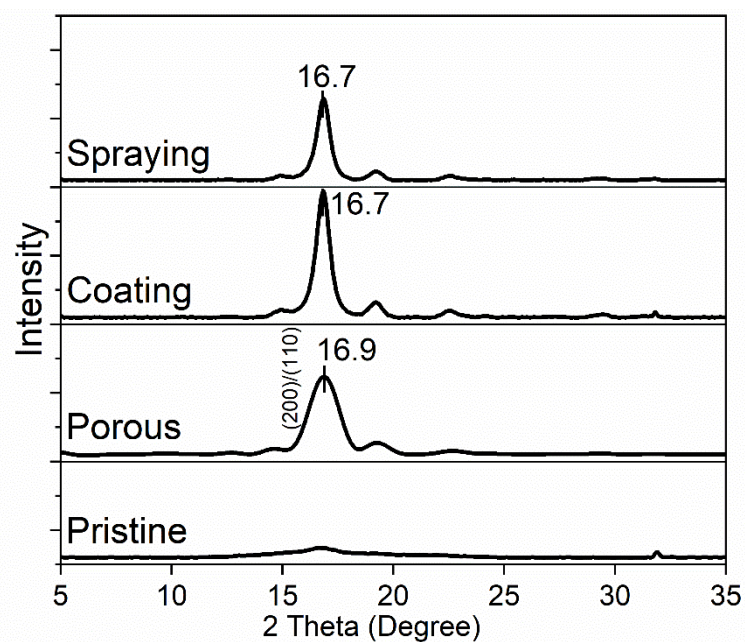


Fig. 5. 19 XRD spectra of pristine PLLA fibres, porous PLLA fibres, SF coating and spraying specimens.

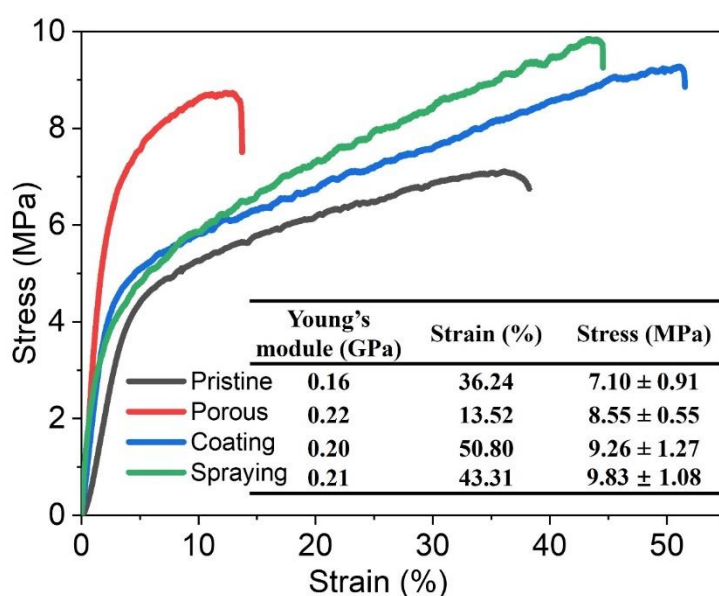


Fig. 5. 20 Tensile stress–strain curves of pristine PLLA fibres, porous PLLA fibres, SF coating and spraying samples.

The mechanical property is shown in Fig. 5.20. The strain-stress curves show the different mechanical properties of 4 groups which are significantly different. For pure PLLA samples, non-porous sample shows a good elongation performance while porous sample has the best Young's module (0.22 GPa) among all groups. This result is in good

agreement with the characteristics of re-crystallized PLLA. For samples with coating/grafting SF, they more tend to back to pristine non-porous PLLA fibrous membrane but a bit better. Both coating and spraying have higher elongation (43% and 51%) than that of non-porous and could preserve good Young's modules (0.20 and 0.21 GPa). Therefore, it can be said that SF surface modification to pure PLLA membrane significantly improved the tensile on the material, but it is also more brittle and shows better mechanical properties.

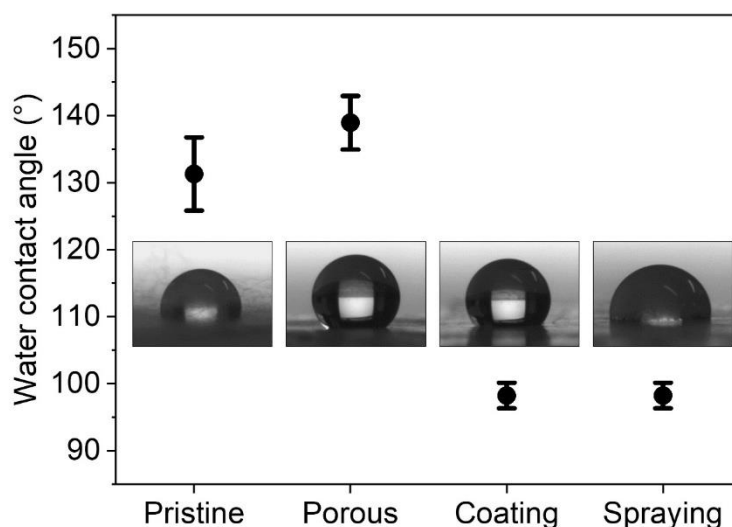


Fig. 5.21 Water contact angle of pristine PLLA fibres, porous PLLA fibres, SF coating and spraying samples.

Water contact angle is another macro characteristic for biomaterials. We can see from Fig. 5.21, that sample non-porous (131°), porous (139°) and coating (134°) are all hydrophobic, but their contact angles are not significantly different based on error bars. The porous PLLA membrane has the highest contact angle because acetone post-treatment makes the surface flatter. Only sample spraying (98°) performed hydrophilic. So, SF spraying method successfully improve the wettability of original PLLA samples. For each group of fibrous membrane samples, the origin videos of water drop on membrane had been recorded during experiment.

In Fig. 5.22, Raman spectroscopy was used to cross-validate a semi-crystalline state of PLLA and cross-linked SF with infrared spectroscopy results. PLLA Raman

bands are assumed to be cylindrically symmetric owing to their helical molecular structure. The most prominent peaks in Fig. 5.22 are located at 872 cm^{-1} , which is assigned to both crystalline and amorphous regions of $\nu\text{C-COO}$ in PLLA, whereas the band at 926 cm^{-1} could be assigned to the crystalline regions only. Other strong peaks appear at 2943 cm^{-1} as semicrystalline and 2942 cm^{-1} as amorphous and are assigned to the symmetrical νCH_3 group. Further, semicrystalline shoulder peaks at 2960 cm^{-1} and 2970 cm^{-1} are assigned to the asymmetric νCH_3 group. To observe amides of SF in Raman curves, we can see two very weak peaks at 1669 cm^{-1} and 1232 cm^{-1} representing β -sheet amide I and amide III, respectively.

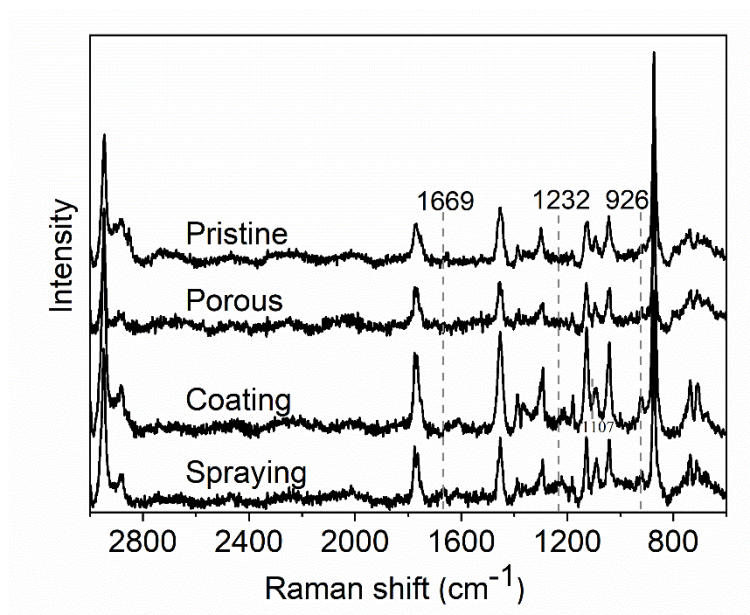


Fig. 5. 22 Raman spectra of pristine PLLA fibres, porous PLLA fibres, SF coating and spraying samples.

Regarding the discussions in Chapter 4 and the XRD-related analysis above, it can be confirmed that PLLA can only show a semicrystalline state after acetone post-treatment. According to the literature, semicrystalline and amorphous PLLA only show weak diffraction peak bands in the characterization of FT-IR. However, the cross-linking status of SF is always observed by infrared spectroscopy. Therefore, FT-IR characterization is mainly done to characterize silk I and Silk II structure of SF in Fig.

5.23. It can be seen that the characteristic peaks of PLLA are clearly displayed, while the characteristic peaks of SF are insignificant. This means most of content of membrane scaffolds are PLLA, which meets the PLLA/SF approximate mass ratio (12:1). From non-porous sample to porous one, we can only observe one change in 955 cm^{-1} . It shows with the acetone re-crystallization, the band characteristic of the helical backbone vibrations disappeared with the CH_3 rocking modes. At the same time, the characteristic peaks of silk fibroin can also be clearly observed in coating and spraying sample. However, the silk fibroin characteristic peak in coating in which a large amount of silk fibroin unevenly covers the surface of the film is more remarkable than that of spraying sample. For coating sample, characteristic peaks at 1621 cm^{-1} in the amide I region and 1529 cm^{-1} in the amide II were assigned to β -sheets [123]. The data collected by infrared spectra consists with the results from XPS and XRD analysis, allowing a conclusion that SF were successfully modified and demonstrates the difference between coating and spraying samples [122].

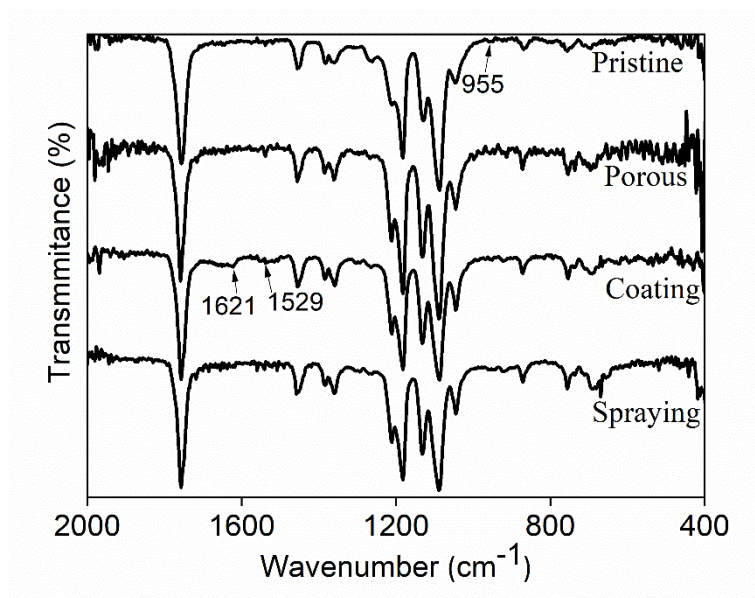


Fig. 5. 23 FT-IR spectra of pristine PLLA fibres, porous PLLA fibres, SF coating and spraying samples.

5.4.3 Multi-layer tunica media scaffolds

A native vascular wall from the lumen outward is generally comprised of tunica intima, tunica media and tunica adventitia. Tunica media is consisted by multi-layered smooth muscle fibres and few collagen intermixed SMCs [110] which give the blood vessels strength and exerting vascular tension [124]. To prepare an off-the-shelf vascular scaffold, SF/PLLA fibrous membrane was rolled to be a tube with a 40-layered wall. Then, the tube was carefully heated at 160°C for 5 sec to fix this structure. In Fig. 5.24a, the macroscale SEM of SF/PLLA tube showed its inner diameter (2.68 ± 0.08) mm and outer diameter (3.89 ± 0.04) mm. In Fig. 5.24b, the cross-section images of stacked multi-layer fibrous membrane was displayed. The average thickness of each layer was 18.13 ± 2.03 μm , which consisted with the native tunica media size.

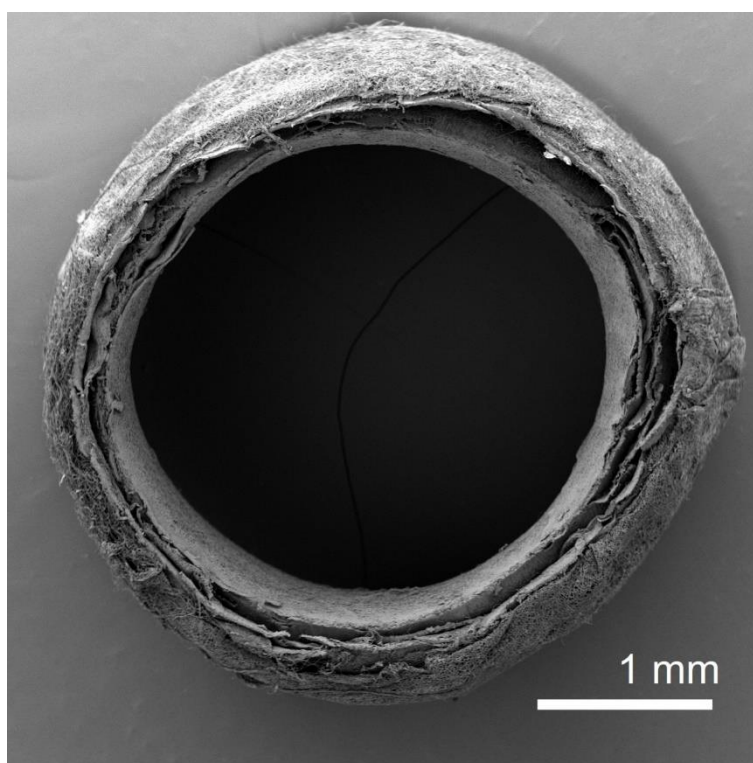


Fig. 5. 24 SEM images of rolled-up SF/PLLA tubular scaffold sample.

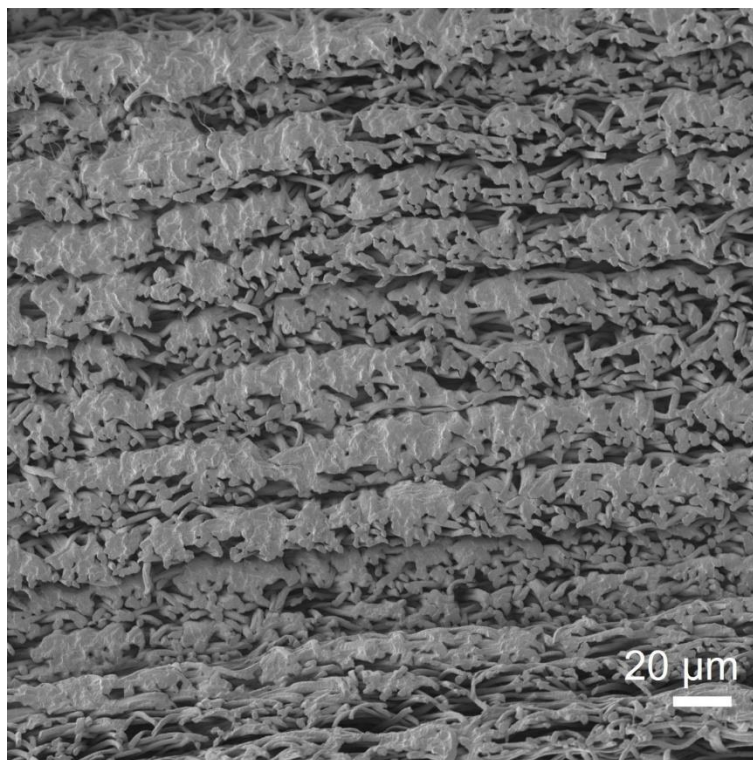


Fig. 5. 25 SEM images of cross-section of the multi-layer tube wall.

5.4.4 Mechanical evaluation of membrane samples

After the fibrous membrane was rolled up towards tubular scaffold, the mechanical property tests should be performed to determine whether tubular scaffold meets relevant standards for potential artificial vascular application. But the conventional tensile test machine is not suitable for test tubular materials. Two 3D-printed holders (Fig. 5.26 & 5.27) were adhesion on two sides of PLLA tubular scaffold for fixing the tube during tensile testing. The 3D-printed model was self-designed by Shapr3D (Budapest, Hungary) software, and fabricated by Photon Zero (Anycubic, China) stereo lithography appearance 3D-printer.

Due to the difficulty measurement of tube thickness, the stress-strain curve is not suitable to present the mechanical performance of tubular materials. So, here I present the strain and ultimate tensile strength (UTS) of three groups of tubular scaffolds in Table 5.1. It could be found in Table 5.1, the PLLA/SF tubular scaffold is more brittle but shows a significant higher UTS. The presented data consists with the pervious

review reported [113].

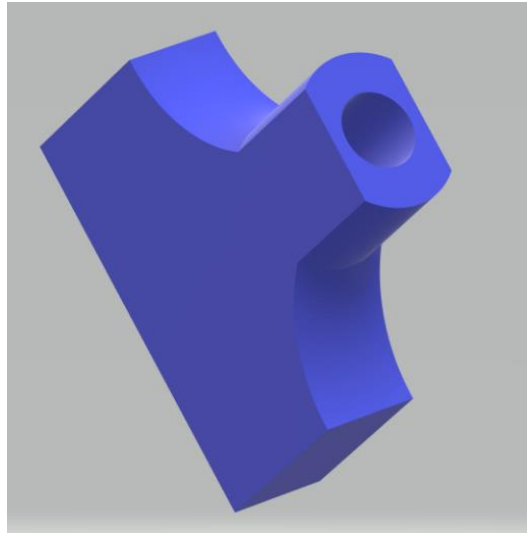


Fig. 5. 26 The 3D-printed holder for loading tubular scaffolds in mechanical evaluation.



Fig. 5. 27 The schematic of 3D-printed holder to load tubular scaffold for tensile tests.

Table 5. 1 The Strain and ultimate tensile strength of three groups of tubular scaffolds.

Groups	Strain	ultimate tensile strength (MPa)
Pristine	103.3% \pm 14.5%	0.11 \pm 0.06
Porous	38.3% \pm 11.5%	0.11 \pm 0.01
Coating	7.2% \pm 3.8%	0.38 \pm 0.04

5.4.4 Cell viability on fibrous membranes

To investigate the biocompatibility of 4 group samples in this research, cells should be seeded precisely on the surface of fibrous membrane. However, the relatively low density and hydrophilicity of PLLA fibrous membrane always wrinkled and floated on the culture medium. To solve this problem, a cell culture protocol was designed as the schematic in Fig. 5.28 demonstrated. The steel rings, that their size is a bit smaller than the wells of 12-well plates, was conglutinated with the upper surface of fibrous membrane by a bio-glue (732 multi-purpose sealant, Dow Corning, USA). A round-shape glass slide was conglutinated on the bottom of membrane by same glue. The stain-less rings played the role of a wall to keep the culture medium with cells on the upper surface of membrane. The glass slide was applied to avoid membrane wrinkling during incubation and provided convenience for further microscope observation after culture. The stainless-steel rings and glass slides were sterilized prior of contacting with fibrous membrane.

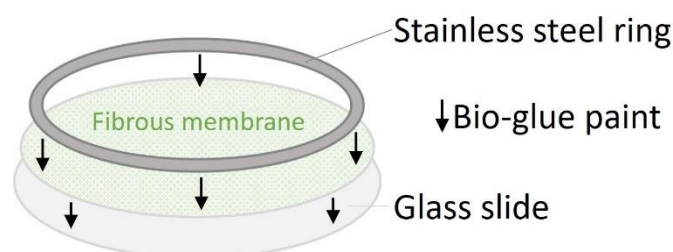


Fig. 5. 28 Cell cultural protocol for fibrous membrane in 12-well plates.

The results of cell count, Alamar Blue assay and DAPI/ Phalloidin staining are

presented in Fig. 5.29 & 5.30. The cell count test at day1 (4 hours after seeding) indicated the cell adhere rate (CAR) when A7R5 cells seeding onto the surface of each membrane scaffold. It could be found that all groups show positive CAR results, and porous (97%), coating (97%) and spraying (95.8%) are higher than non-porous (88.5%). Previous studies by Leong et al. and Yang et al. have demonstrated that nanopores in fibres can enhance cell attachment and proliferation in comparison to solid electrospun fibrous scaffolds [125,126]. It is believed that is due to the difference in the material morphology between non-porous and the other group. Non-porous fibre has a soft, flexible character ($\sim 90 \mu\text{m}$), and this means the cell more difficult to landing than other samples.

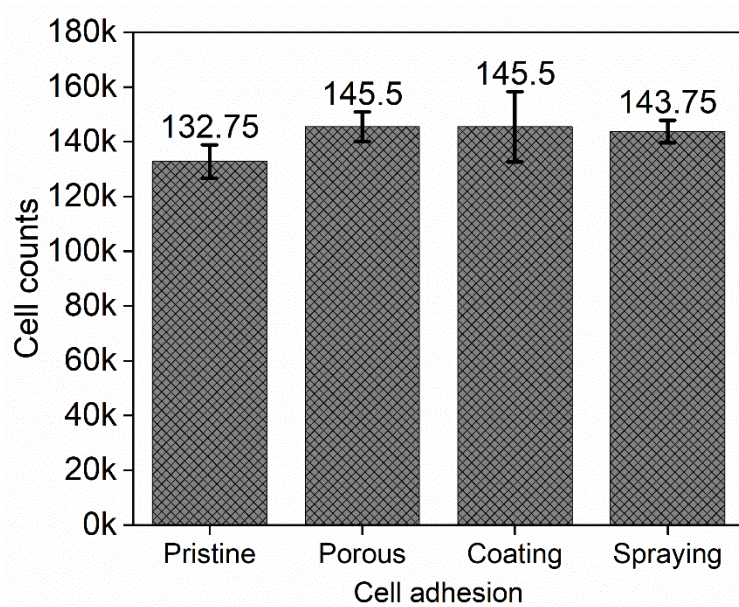


Fig. 5. 29 A7r5 cell number count for pristine PLLA fibres, porous PLLA fibres, SF coating and spraying samples on day 1 post seeding.

The Alamar Blue assay indicated the cell growth rate at each time point. The results of day 1, 4, 7, 10 and 14 are illustrated in Fig. 5.26. The statistical difference (significance shown in figure) of each sample happened at one week after seeding. Non-porous has the lowest cell metabolic activity of all, which demonstrates non-porous fibre is not suitable to be used as a stable scaffold [125,127]. In day 7, the coating sample had the best cell proliferation and statistically (64.41%) if compared with non-porous

(52.52%) and spraying (53.40%). Further, porous sample also had a significantly greater reduction of Alamar Blue measuring 60.81% at day 7. This was maintained until day 10. At day 10, the results of non-porous and spraying increased. However, porous and coating samples reduced while coating became statistically higher than porous. After day 10, it could be assumed that cells were under contact inhibition. It is a good result for a potential implanted biodegradable scaffold, especially in day 10. In general, cells on sample coating had the highest metabolic activity, spraying being similar to porous, but growing slower than the porous. Non-porous sample shows a minimum metabolic activity among all other groups.

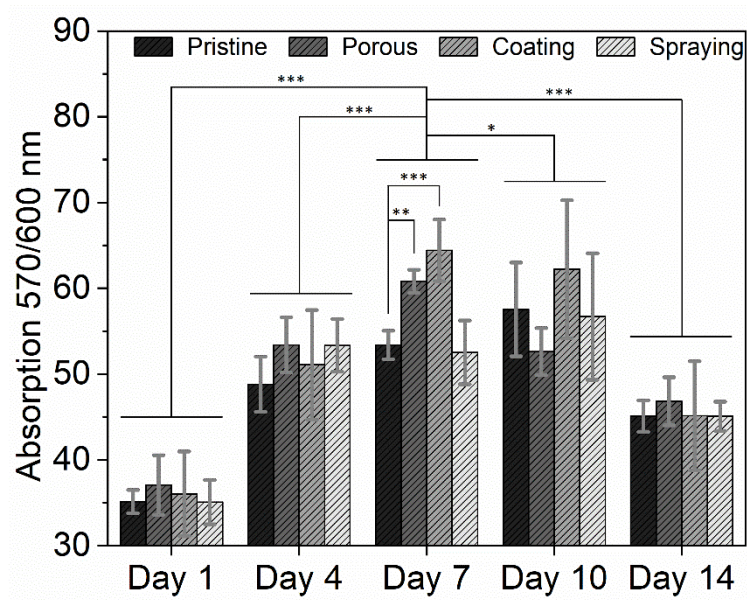


Fig. 5. 30 Alamar blue assay results during cell culture up to day 14 post seeding. Data are presented as mean \pm SD, $n = 4$, Student's t-test, * $p < 0.05$, ** $p < 0.01$, *** $p < 0.001$.

5.4.5 SMCs proliferation and morphology on membrane scaffolds

The DAPI/ Phalloidin staining gives a detailed view of the cell morphology. It has a general view of 3 time points of laser confocal and a zoom of signal cell morphology too. Cells in non-porous samples are of a small round shape, and tend to aggregate together and have less indication of F-actin [126]. Combining the foregoing Alamar

Blue results means cells divide quickly but there is less metabolically growth active on non-porous scaffolds. If cells are agglomerated on the surface of non-porous, the cells are obviously small and not stretch as in other groups. This indicates the non-porous fibre is not good for cell adhesion. In contrast, sample porous, coating and spraying consist of hierarchical porous nanofibre which is obviously good for cell adhesion. In particular, when fibres modified by SF, cells on both coating and spraying samples showed extended morphology. Porous sample's cell morphology was improved a lot when compared with non-porous. We can see some of cells are still trended to gather and keep small, which is a manifestation of low metabolic activity. However, other cells formed a poached-egg like structure after one-week of incubation. This is a morphology that shows the cells are in good metabolic status.

SF shows self-fluorescence when stained by DAPI. This means a clear view of not only cells but also fibres in coating and spraying sample. From the images, it can be confirmed that cross-linked SF show biodegradation stable in this work. Visually, it could be found that on coating sample, there are the highest quantity of cells among all 4 samples. This performance is also consistent with the result that coating maintained high metabolic activity for most of time points during the experiment.

With a mechanical structure in which hierarchical porous nano-fibres are more brittle, the morphology of spraying sample allows the cells to stretch. When covered by SF, the longer degradation time gives the cells sufficient mechanical strength support if compared with pure PLLA samples. Also, the unnecessary proliferation of cells on the scaffold surface can be controlled by adjusting the volume of SF on PLLA fibres, in the spraying method particularly. There is a clear morphology that the cell growth direction follows the fibre direction on both coating and spraying sample. The SF is well uniformed to cover the PLLA fibres in spraying sample, and cells will have a lack of mechanical support when SF is degraded faster than that in coating sample. This is the possible reasons for metabolic decrease in spraying sample after one-week of incubation [125]. Cells on coating and spraying sample disperse and stretch healthy. From the SEM images shown, cells are strongly attached and grown on the surface of fibrous membrane. With a further observation by 3D images with $40 \times$ magnification,

it can be found that cell stretch their feet to cover the fibres and even twisted fibres. So, the antennal growth of the cell follows the direction of the fibre for the regeneration of the arterial 40-layered tunica media. This membrane can be used to guide the cell growth direction.

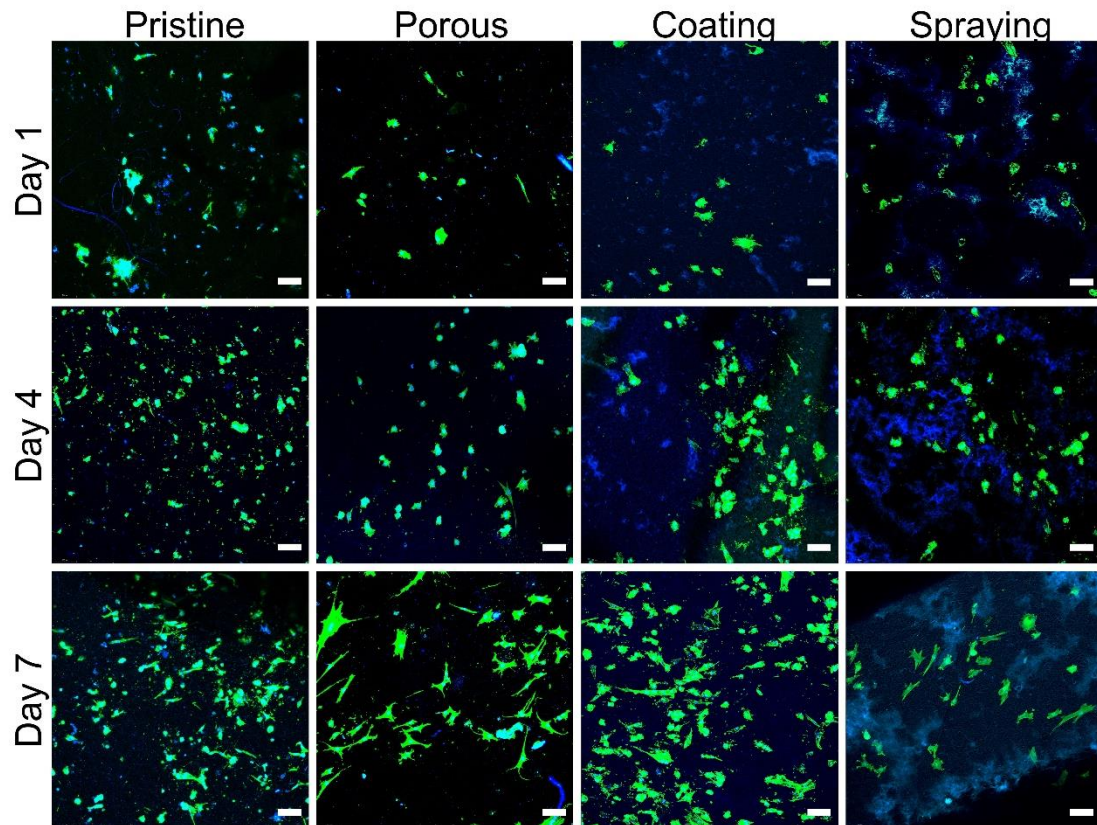


Fig. 5. 31 Laser confocal images for the morphology of A7r5 cells growing on the surface of four groups membrane samples at three time points post seeding.

Cells were stained by DAPI and Phalloidin to observe nucleuses and cytoskeletons, respectively. Scale bars = 100 μ m.

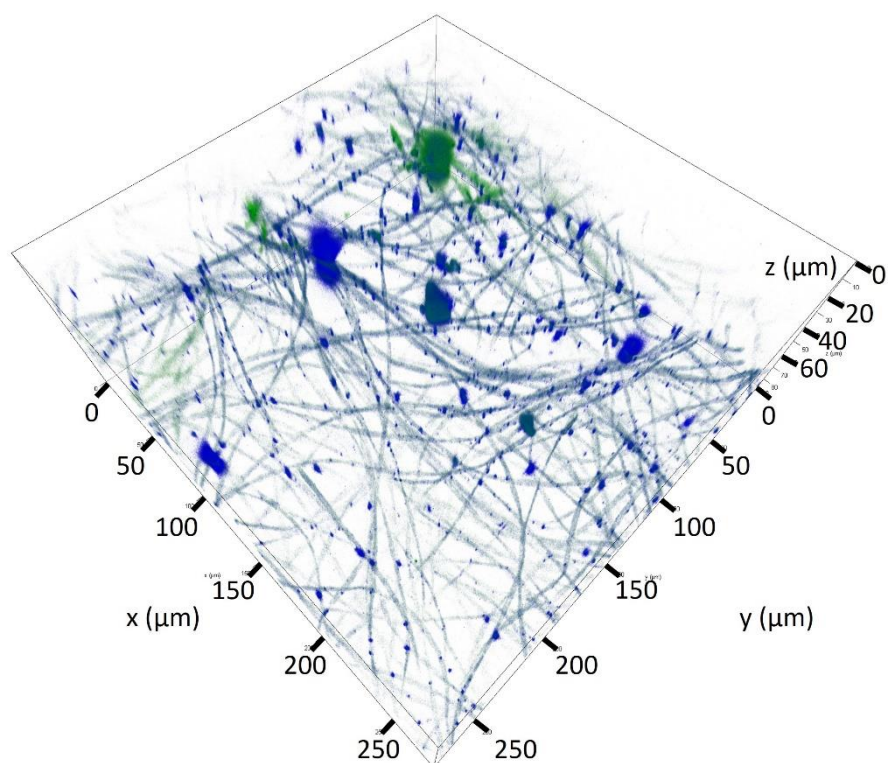


Fig. 5. 32 Laser confocal 3D images of pristine membrane after seeding.

With $40\times$ magnification. $x = y = 300\ \mu\text{m}$, $z_{\text{Pristine}} = 80\ \mu\text{m}$.

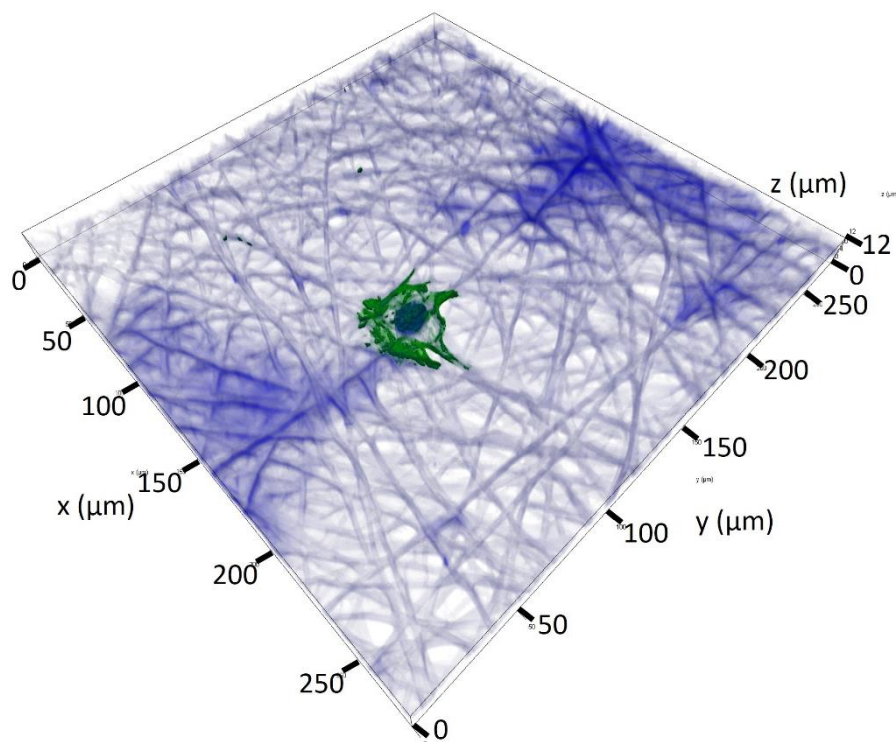


Fig. 5. 33 Laser confocal 3D images of porous membrane after seeding.

With $40\times$ magnification. $x = y = 300\ \mu\text{m}$, $z_{\text{Porous}} = 12\ \mu\text{m}$,

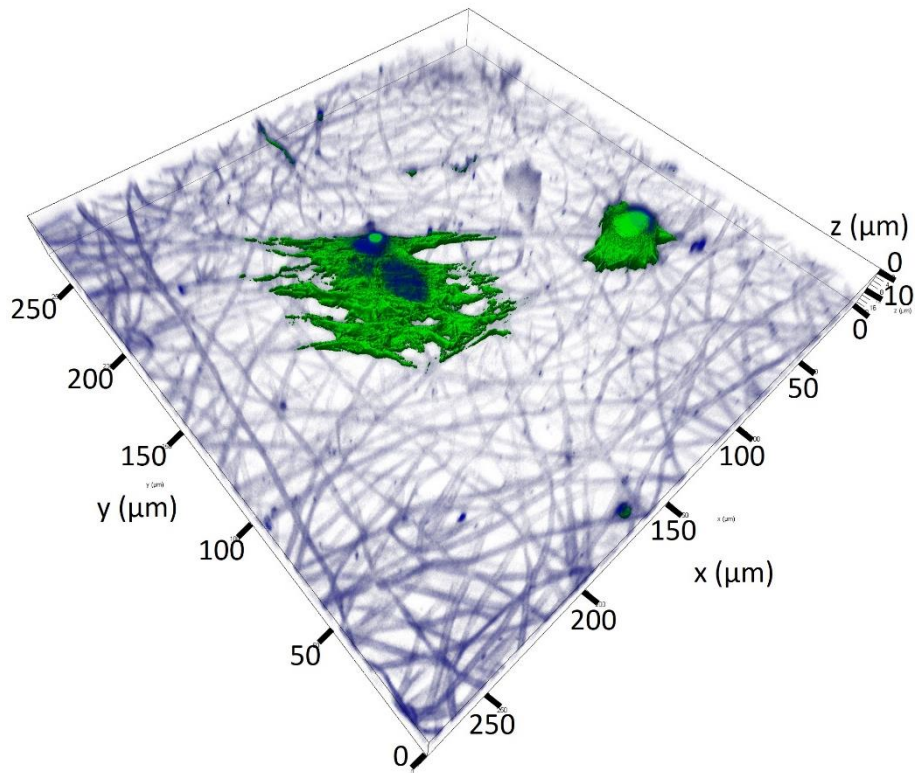


Fig. 5. 34 Laser confocal 3D images of porous membrane with SF coating after seeding.
With $40\times$ magnification. $x = y = 300\ \mu\text{m}$, $z_{\text{Coating}} = 16\ \mu\text{m}$

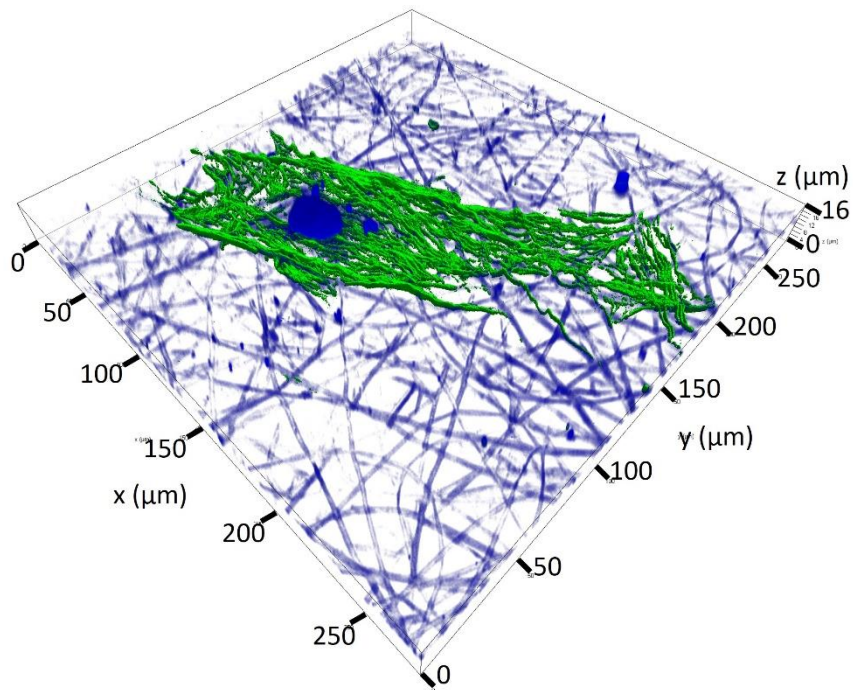


Fig. 5. 35 Laser confocal 3D images of porous membrane with SF spraying after seeding.
With $40\times$ magnification. $x = y = 300\ \mu\text{m}$, $z_{\text{Spraying}} = 20\ \mu\text{m}$.

5.5 Conclusions

Herein, a high roughness fibrous membrane graft composed of porous PLLA fibres and SF coating was designed and characterized. The coating uniformity and stability of SF/PLLA fibres could be optimized by adjusting the volume and concentration of SF solutions. The hydrophilicity and mechanical properties of SF/PLLA were improved significantly by the tight and uniform SF coating. SF/PLLA composite scaffold had similar strain and stress to the artery. A multi-layered tubular scaffold towards tunica media could be further prepared by a facile rolling method. The 14-day in vitro cell culture with smooth muscle cells revealed that the SF coating onto porous PLLA fibrous membranes led a significant enhancement to cell adhesion and proliferation. The slender cell shape and spread actin cytoskeleton of SMCs growing on the SF/PLLA membrane demonstrate that the SF/PLLA surface could better support the adhesion and growth of VSMCs. These results suggested that the highly rough and porous SF/PLLA fibrous membrane has a great potential to be used as vascular regeneration scaffolds. Moreover, this study demonstrates that an off-the-shelf vascular scaffold could be fabricated from SF/PLLA membrane by a facile method, thus enabling this scaffold as a potential clinical application.

Chapter 6: Conclusion and Outlook

6.1 General Conclusion

PLLA is a typical natural resourced biomaterial, which is in line with the overall strategy of global carbon neutralization and belongs to the next generation of chemical fibre. This project focused on the study of fabrication methods of hierarchical porous PLLA fibrous membrane with ultra-high specific surface area by an electrospinning and post-treatment two-step strategy. The potential environmental and biological applications were also systematically investigated in this thesis.

The first section of this thesis is a literature review in chapter 2, including the theory and mechanism of porous fibre fabricated by electrospinning technology, the essential properties of poly(L-lactic acid) (PLLA) and silk fibroin (SF) and the application of electrospinning materials, especially suitable for PLLA-based and/or SF-based, followed by the general research materials and methods as the second section.

The third part of thesis tried to optimize the electrospinning parameter to prepare NIPS porous PLLA fibres. Due to the relatively high molecular weight of PLLA (1.43 M), the concentration of electrospinning solution should be controlled around 2.0% w/w. Then, the acetone was used to improve the surface morphology of fibres. It is found that the pristine amorphous PLLA fibres was re-crystallised by acetone treatment. The porous PLLA films could filter out the aerosol particles (<100 nm) while the pressure drop was kept at a reasonable level. Because of enhanced aerosol particulate diffusion, this kind of a filter membrane showed higher QF with the decreasing of aerosol particle size. This finding demonstrates that the electrospun membrane with a hierarchical pore structure and high specific surface area hold great potential in applications as air-filtering materials.

The third part of this project involved in a natural macromolecule, silk fibroin, to modify PLLA fibres. SF was uniformly coated on the PLLA fibres. The mechanical property, biodegradability, biocompatibility, and the most important, hydrophilicity of fibrous membrane, was elevated after this surface modification, while the highly roughness surface morphology of fibres was kept. Further *in vitro* evaluation demonstrate that an off-the-shelf vascular scaffold could be fabricated from SF/PLLA membrane by a facile method, thus enabling this scaffold as a potential clinical application.

It is a pity that a proposed section, PLLA/SF fibrous membrane-based biosensors were not carried out due to the impact of COVID-19 pandemic.

To sum up, this thesis covers four major sections: 1) A literature review about electrospinning fabrication, porous fibre forming mechanism, PLLA, SF, and their electrospun materials. 2) A general research materials and methods for potential future experimental repetition. 3) To optimize a protocol to fabricate hierarchical porous PLLA electrospun fibres with high specific surface area, porosity, along with desired mechanical property. The application experiments also demonstrated this membrane is likely used as a next-generation filter. 4) To construct high roughness PLLA/SF fibrous membrane though SF coating modification on surface of porous PLLA fibres. The *in vitro* evaluation proved its potential application as a tissue engineered scaffold.

6.2 Outlook

The mechanism of porous PLLA fibres has been investigated and proposed. Especially for solvent induced post-treatment, the experiments and theory could be extended in other polymers such as polycaprolactone (PCL) and polyethylene terephthalate (PET).

For aerosol filtration application, the pure PLLA fibrous membranes are not strong enough to support bear the high-volume air flow. It is possible that PLLA fibres could be *in situ* electrospun onto a matrix or substrate, like electrospun fibres from other

polymers or non-woven fabric. As a more general air filtration application, the ability of hierarchical PLLA fibrous membrane to intercept larger particles including PM 2.5 & PM 10 could be investigated.

For further research about vascular scaffolds made by electrospun PLLA/SF tube, the mechanical properties of tube could be characterized as it is one of the most important factors for tissue engineered product. Also, it is possible that rolling up a PLLA/SF fibrous membrane with differentiated induced stem cell lines towards tube. With the development of implanted tissue engineering scaffold, it is essential to functionalize biomaterials. Loading growth factor or other drug during the SF surface modification process on PLLA fibres is another project worthy to be investigate.

References

- [1] J. Xue, T. Wu, Y. Dai, Y. Xia, Electrospinning and Electrospun Nanofibers: Methods, Materials, and Applications, *Chem. Rev.* 119 (2019) 5298–5415. <https://doi.org/10.1021/acs.chemrev.8b00593>.
- [2] C. Kemfert, ‘Climate neutral’ is a lie — abandon it as a goal, *Nature*. 591 (2021) 34–34. <https://doi.org/10.1038/d41586-021-00543-9>.
- [3] M. Bognitzki, W. Czado, T. Frese, A. Schaper, M. Hellwig, M. Steinhart, A. Greiner, J.H. Wendorff, Nanostructured Fibers via Electrospinning, *Adv. Mater.* 13 (2001) 70–72. [https://doi.org/10.1002/1521-4095\(200101\)13:1<70::AID-ADMA70>3.0.CO;2-H](https://doi.org/10.1002/1521-4095(200101)13:1<70::AID-ADMA70>3.0.CO;2-H).
- [4] F. Kayaci, C. Ozgit-Akgun, I. Donmez, N. Biyikli, T. Uyar, Polymer–Inorganic Core–Shell Nanofibers by Electrospinning and Atomic Layer Deposition: Flexible Nylon–ZnO Core–Shell Nanofiber Mats and Their Photocatalytic Activity, *ACS Appl. Mater. Interfaces*. 4 (2012) 6185–6194. <https://doi.org/10.1021/am3017976>.
- [5] L. Li, S. Peng, J.K.Y. Lee, D. Ji, M. Srinivasan, S. Ramakrishna, Electrospun hollow nanofibers for advanced secondary batteries, *Nano Energy*. 39 (2017) 111–139. <https://doi.org/10.1016/j.nanoen.2017.06.050>.
- [6] Z. Wang, Z. Pan, Preparation of hierarchical structured nano-sized/porous poly(lactic acid) composite fibrous membranes for air filtration, *Appl. Surf. Sci.* 356 (2015) 1168–1179. <https://doi.org/10.1016/j.apsusc.2015.08.211>.
- [7] Z. Wang, C. Zhao, Z. Pan, Porous bead-on-string poly(lactic acid) fibrous membranes for air filtration, *J. Colloid Interface Sci.* 441 (2015) 121–129. <https://doi.org/10.1016/j.jcis.2014.11.041>.
- [8] X. Zhao, L. Chen, Y. Guo, X. Ma, Z. Li, W. Ying, X. Peng, Porous cellulose nanofiber stringed HKUST-1 polyhedron membrane for air purification, *Appl.*

- Mater. Today. 14 (2019) 96–101. <https://doi.org/10.1016/j.apmt.2018.11.012>.
- [9] A. Koski, K. Yim, S. Shivkumar, Effect of molecular weight on fibrous PVA produced by electrospinning, Mater. Lett. 58 (2004) 493–497. [https://doi.org/10.1016/S0167-577X\(03\)00532-9](https://doi.org/10.1016/S0167-577X(03)00532-9).
- [10] J. Li, B. Zhu, Y. Shao, X. Liu, X. Yang, Q. Yu, Construction of anticoagulant poly (lactic acid) films via surface covalent graft of heparin-carrying microcapsules, Colloids Surf., B. 70 (2009) 15–19. <https://doi.org/10.1016/j.colsurfb.2008.12.001>.
- [11] L. Li, R. Hashaikh, H.A. Arafat, Development of eco-efficient micro-porous membranes via electrospinning and annealing of poly (lactic acid), J. Memb. Sci. 436 (2013) 57–67. <https://doi.org/10.1016/j.memsci.2013.02.037>.
- [12] O. Monticelli, S. Bocchini, L. Gardella, D. Cavallo, P. Cebe, G. Germelli, Impact of synthetic talc on PLLA electrospun fibers, Eur. Polym. J. 49 (2013) 2572–2583. <https://doi.org/10.1016/j.eurpolymj.2013.05.017>.
- [13] Z. Qi, H. Yu, Y. Chen, M. Zhu, Highly porous fibers prepared by electrospinning a ternary system of nonsolvent/solvent/poly(l-lactic acid), Mater. Lett. 63 (2009) 415–418. <https://doi.org/10.1016/j.matlet.2008.10.059>.
- [14] L. Natarajan, J. New, A. Dasari, S. Yu, M.A. Manan, Surface morphology of electrospun PLA fibers: mechanisms of pore formation, RSC Adv. 4 (2014) 44082–44088. <https://doi.org/10.1039/C4RA06215A>.
- [15] E. Rezabeigi, M. Sta, M. Swain, J. McDonald, N.R. Demarquette, R.A.L. Drew, P.M. Wood-Adams, Electrospinning of porous polylactic acid fibers during nonsolvent induced phase separation, J. Appl. Polym. Sci. 134 (2017). <https://doi.org/10.1002/app.44862>.
- [16] C. Huang, N.L. Thomas, Fabricating porous poly(lactic acid) fibres via electrospinning, Eur. Polym. J. 99 (2018) 464–476. <https://doi.org/10.1016/j.eurpolymj.2017.12.025>.
- [17] D. Zhang, N. Zhang, F. Ma, X. Qi, J. Yang, T. Huang, Y. Wang, One-step fabrication of functionalized poly(l-lactide) porous fibers by electrospinning and the adsorption/separation abilities, J. Hazard. Mater. 360 (2018) 150–162.

- <https://doi.org/10.1016/j.jhazmat.2018.07.090>.
- [18] R. Casasola, N.L. Thomas, A. Trybala, S. Georgiadou, Electrospun poly lactic acid (PLA) fibres: Effect of different solvent systems on fibre morphology and diameter, *Polymer*. 55 (2014) 4728–4737.
<https://doi.org/10.1016/J.POLYMER.2014.06.032>.
- [19] Q. Zia, M. Tabassum, Z. Lu, M.T. Khawar, J. Song, H. Gong, J. Meng, Z. Li, J. Li, Porous poly(L-lactic acid)/chitosan nanofibres for copper ion adsorption, *Carbohydr. Polym.* 227 (2020) 115343.
<https://doi.org/10.1016/j.carbpol.2019.115343>.
- [20] B. Zhu, H. Wang, W.R. Leow, Y. Cai, X.J. Loh, M.-Y. Han, X. Chen, Silk Fibroin for Flexible Electronic Devices, *Adv. Mater.* 28 (2016) 4250–4265.
<https://doi.org/10.1002/adma.201504276>.
- [21] W. ZAOMING, R. CODINA, E. FERNANDEZCALDAS, R. LOCKEY, S. BUKANZ, 109 Partial characterization of the silk allergens in mulberry silk extract, *J. Allergy Clin. Immunol.* 97 (1996) 210–210.
[https://doi.org/10.1016/S0091-6749\(96\)80327-7](https://doi.org/10.1016/S0091-6749(96)80327-7).
- [22] Y.-Q. Zhang, Applications of natural silk protein sericin in biomaterials, *Biotechnol. Adv.* 20 (2002) 91–100. [https://doi.org/10.1016/S0734-9750\(02\)00003-4](https://doi.org/10.1016/S0734-9750(02)00003-4).
- [23] L. Zhou, X. Chen, Z. Shao, Y. Huang, D.P. Knight, Effect of Metallic Ions on Silk Formation in the Mulberry Silkworm, *Bombyx mori*, *J. Phys. Chem. B*. 109 (2005) 16937–16945. <https://doi.org/10.1021/jp050883m>.
- [24] K. Tanaka, N. Kajiyama, K. Ishikura, S. Waga, A. Kikuchi, K. Ohtomo, T. Takagi, S. Mizuno, Determination of the site of disulfide linkage between heavy and light chains of silk fibroin produced by *Bombyx mori*, *Biochim. Biophys. Acta, Protein Struct. Mol. Enzymol.* 1432 (1999) 92–103.
[https://doi.org/10.1016/S0167-4838\(99\)00088-6](https://doi.org/10.1016/S0167-4838(99)00088-6).
- [25] S. Inoue, K. Tanaka, F. Arisaka, S. Kimura, K. Ohtomo, S. Mizuno, Silk Fibroin of *Bombyx mori* Is Secreted, Assembling a High Molecular Mass Elementary Unit Consisting of H-chain, L-chain, and P25, with a 6:6:1 Molar

- Ratio, *J. Biol. Chem.* 275 (2000) 40517–40528.
<https://doi.org/10.1074/jbc.M006897200>.
- [26] C. Vepari, D.L. Kaplan, Silk as a biomaterial, *Prog. Polym. Sci.* 32 (2007) 991–1007. <https://doi.org/10.1016/j.progpolymsci.2007.05.013>.
- [27] E. Wenk, H.P. Merkle, L. Meinel, Silk fibroin as a vehicle for drug delivery applications, *J. Control. Release.* 150 (2011) 128–141.
<https://doi.org/10.1016/j.jconrel.2010.11.007>.
- [28] I. Sillitoe, T.E. Lewis, A. Cuff, S. Das, P. Ashford, N.L. Dawson, N. Furnham, R.A. Laskowski, D. Lee, J.G. Lees, S. Lehtinen, R.A. Studer, J. Thornton, C.A. Orengo, CATH: comprehensive structural and functional annotations for genome sequences, *Nucleic Acids Res.* 43 (2014) D376–D381.
<https://doi.org/10.1093/nar/gku947>.
- [29] B. Lotz, F. Colonna Cesari, The chemical structure and the crystalline structures of *Bombyx mori* silk fibroin, *Biochimie.* 61 (1979) 205–214.
[https://doi.org/10.1016/S0300-9084\(79\)80067-X](https://doi.org/10.1016/S0300-9084(79)80067-X).
- [30] R.E. Marsh, R.B. Corey, L. Pauling, An investigation of the structure of silk fibroin, *Biochim. Biophys. Acta.* 16 (1955) 1–34. [https://doi.org/10.1016/0006-3002\(55\)90178-5](https://doi.org/10.1016/0006-3002(55)90178-5).
- [31] D.N. Rockwood, R.C. Preda, T. Yücel, X. Wang, M.L. Lovett, D.L. Kaplan, Materials fabrication from *Bombyx mori* silk fibroin, *Nat. Protoc.* 6 (2011) 1612–1631. <https://doi.org/10.1038/nprot.2011.379>.
- [32] G.W. Camille, Dreyfus, Miles, Method of making silk products, US1936753, 1933.
- [33] K.I. H. Ishizaka, Y. Watanabe, Regenerated silk prepared from ortho phosphoric acid solution of fibroin, *Nippon Sanshigaku Zasshi.* 58 (1989) 87–95.
https://www.jstage.jst.go.jp/article/kontyushigen1930/58/2/58_2_87/_article/-char/ja/.
- [34] Gustavus J Esselen, Production of silk fibers, US1934413A, 1931.
<https://patents.google.com/patent/US1934413A/en>.

- [35] Robert L. Lock, Process for making silk fibroin fibers, US5252285A, 1992.
<https://patents.google.com/patent/US5252285A/en>.
- [36] K. Matsumoto, H. Uejima, T. Iwasaki, Y. Sano, H. Sumino, Studies on regenerated protein fibers. III. Production of regenerated silk fibroin fiber by the self-dialyzing wet spinning method, *J. Appl. Polym. Sci.* 60 (1996) 503–511. [https://doi.org/10.1002/\(SICI\)1097-4628\(19960425\)60:4<503::AID-APP3>3.0.CO;2-S](https://doi.org/10.1002/(SICI)1097-4628(19960425)60:4<503::AID-APP3>3.0.CO;2-S).
- [37] S.-W. Ha, A.E. Tonelli, S.M. Hudson, Structural Studies of *Bombyx mori* Silk Fibroin during Regeneration from Solutions and Wet Fiber Spinning, *Biomacromolecules*. 6 (2005) 1722–1731. <https://doi.org/10.1021/bm050010y>.
- [38] I.C. Um, H. Kweon, Y.H. Park, S. Hudson, Structural characteristics and properties of the regenerated silk fibroin prepared from formic acid, *Int. J. Biol. Macromol.* 29 (2001) 91–97. [https://doi.org/10.1016/S0141-8130\(01\)00159-3](https://doi.org/10.1016/S0141-8130(01)00159-3).
- [39] S.S. Silva, E.G. Popa, M.E. Gomes, M.B. Oliveira, S. Nayak, B. Subia, J.F. Mano, S.C. Kundu, R.L. Reis, Silk hydrogels from non-mulberry and mulberry silkworm cocoons processed with ionic liquids, *Acta Biomater.* 9 (2013) 8972–8982. <https://doi.org/10.1016/j.actbio.2013.06.044>.
- [40] R.-L. Wu, X.-L. Wang, Y.-Z. Wang, X.-C. Bian, F. Li, Cellulose/Soy Protein Isolate Blend Films Prepared via Room-Temperature Ionic Liquid, *Ind. Eng. Chem. Res.* 48 (2009) 7132–7136. <https://doi.org/10.1021/ie9001052>.
- [41] F. Zhang, Q. Lu, J. Ming, H. Dou, Z. Liu, B. Zuo, M. Qin, F. Li, D.L. Kaplan, X. Zhang, Silk dissolution and regeneration at the nanofibril scale, *J. Mater. Chem. B*. 2 (2014) 3879. <https://doi.org/10.1039/c3tb21582b>.
- [42] J. Shao, J. Liu, J. Zheng, C. Carr, X-ray photoelectron spectroscopic study of silk fibroin surface, *Polym. Int.* 51 (2002) 1479–1483.
<https://doi.org/10.1002/pi.1092>.
- [43] A. Sinsawat, S. Putthanasarat, Y. Magoshi, R. Pachter, R.K. Eby, X-ray diffraction and computational studies of the modulus of silk (*Bombyx mori*), *Polymer (Guildf)*. 43 (2002) 1323–1330. [https://doi.org/10.1016/S0032-3861\(01\)00696-6](https://doi.org/10.1016/S0032-3861(01)00696-6).

- [44] N. Bhardwaj, S.C. Kundu, Chondrogenic differentiation of rat MSCs on porous scaffolds of silk fibroin/chitosan blends, *Biomaterials*. 33 (2012) 2848–2857.
<https://doi.org/10.1016/j.biomaterials.2011.12.028>.
- [45] Y. Yang, W. Gao, Wearable and flexible electronics for continuous molecular monitoring, *Chem. Soc. Rev.* 48 (2019) 1465–1491.
<https://doi.org/10.1039/C7CS00730B>.
- [46] R.J. Young, P.A. Lovell, *Introduction to Polymers*, CRC Press, 2011.
<https://doi.org/10.1201/9781439894156>.
- [47] A.F.M. Barton, *CRC Handbook of Solubility Parameters and Other Cohesion Parameters*, Routledge, 2017. <https://doi.org/10.1201/9781315140575>.
- [48] M. Tamizifar, G. Sun, Control of surface radical graft polymerization on polyester fibers by using Hansen solubility parameters as a measurement of the affinity of chemicals to materials, *RSC Adv.* 7 (2017) 13299–13303.
<https://doi.org/10.1039/C6RA27186C>.
- [49] Hiroshi Yamamoto, Hansen Solubility Parameters(HSP) Application Notes, (2010). <https://pirika.com/NewHP/PirikaE2/Hesperidine.html> (accessed July 10, 2021).
- [50] P.J. Flory, Thermodynamics of High Polymer Solutions, *J. Chem. Phys.* 9 (1941) 660–660. <https://doi.org/10.1063/1.1750971>.
- [51] M.L. Huggins, Solutions of Long Chain Compounds, *J. Chem. Phys.* 9 (1941) 440–440. <https://doi.org/10.1063/1.1750930>.
- [52] C. Huang, N.L. Thomas, Fabrication of porous fibers via electrospinning: strategies and applications, *Polym. Rev.* (2019) 1–53.
<https://doi.org/10.1080/15583724.2019.1688830>.
- [53] P.. Laity, P.. Glover, J.. Hay, Composition and phase changes observed by magnetic resonance imaging during non-solvent induced coagulation of cellulose, *Polymer*. 43 (2002) 5827–5837. [https://doi.org/10.1016/S0032-3861\(02\)00531-1](https://doi.org/10.1016/S0032-3861(02)00531-1).
- [54] J. Peng, Y. Han, Y. Yang, B. Li, The influencing factors on the macroporous formation in polymer films by water droplet templating, *Polymer*. 45 (2004)

- 447–452. <https://doi.org/10.1016/j.polymer.2003.11.019>.
- [55] Q. Xing, X. Dong, R. Li, H. Yang, C.C. Han, D. Wang, Morphology and performance control of PLLA-based porous membranes by phase separation, *Polymer*. 54 (2013) 5965–5973. <https://doi.org/10.1016/j.polymer.2013.08.007>.
- [56] J.T. McCann, M. Marquez, Y. Xia, Highly Porous Fibers by Electrospinning into a Cryogenic Liquid, *J. Am. Chem. Soc.* 128 (2006) 1436–1437. <https://doi.org/10.1021/ja056810y>.
- [57] I.N. Strain, Q. Wu, A.M. Pourrahimi, M.S. Hedenqvist, R.T. Olsson, R.L. Andersson, Electrospinning of recycled PET to generate tough mesomorphic fibre membranes for smoke filtration, *J. Mater. Chem. A*. 3 (2015) 1632–1640. <https://doi.org/10.1039/C4TA06191H>.
- [58] N. Naga, Y. Yoshida, M. Inui, K. Noguchi, S. Murase, Crystallization of amorphous poly(lactic acid) induced by organic solvents, *J. Appl. Polym. Sci.* 119 (2011) 2058–2064. <https://doi.org/10.1002/app.32890>.
- [59] N. Naga, Y. Yoshida, K. Noguchi, Crystallization of poly(L-lactic acid)/poly(D-lactic acid) blend induced by organic solvents, *Polym. Bull.* 76 (2019) 3677–3691. <https://doi.org/10.1007/s00289-018-2563-z>.
- [60] J. Gao, L. Duan, G. Yang, Q. Zhang, M. Yang, Q. Fu, Manipulating poly(lactic acid) surface morphology by solvent-induced crystallization, *Appl. Surf. Sci.* 261 (2012) 528–535. <https://doi.org/10.1016/j.apsusc.2012.08.050>.
- [61] Z. Lu, B. Zhang, H. Gong, J. Li, Fabrication of hierarchical porous poly (l-lactide) (PLLA) fibrous membrane by electrospinning, *Polymer*. 226 (2021) 123797. <https://doi.org/10.1016/j.polymer.2021.123797>.
- [62] F. Awaja, D. Pavel, Recycling of PET, *Eur. Polym. J.* 41 (2005) 1453–1477. <https://doi.org/10.1016/j.eurpolymj.2005.02.005>.
- [63] R. Zhang, C. Liu, P.-C. Hsu, C. Zhang, N. Liu, J. Zhang, H.R. Lee, Y. Lu, Y. Qiu, S. Chu, Y. Cui, Nanofiber Air Filters with High-Temperature Stability for Efficient PM 2.5 Removal from the Pollution Sources, *Nano Lett.* 16 (2016) 3642–3649. <https://doi.org/10.1021/acs.nanolett.6b00771>.
- [64] G.Q. Gu, C.B. Han, C.X. Lu, C. He, T. Jiang, Z.L. Gao, C.J. Li, Z.L. Wang,

- Triboelectric Nanogenerator Enhanced Nanofiber Air Filters for Efficient Particulate Matter Removal, *ACS Nano*. 11 (2017) 6211–6217.
<https://doi.org/10.1021/acsnano.7b02321>.
- [65] K. Min, S. Kim, S. Kim, Silk protein nanofibers for highly efficient, eco-friendly, optically translucent, and multifunctional air filters, *Sci. Rep.* 8 (2018) 9598. <https://doi.org/10.1038/s41598-018-27917-w>.
- [66] X. Huang, R. Wang, T. Jiao, G. Zou, F. Zhan, J. Yin, L. Zhang, J. Zhou, Q. Peng, Facile Preparation of Hierarchical AgNP-Loaded MXene/Fe₃O₄/Polymer Nanocomposites by Electrospinning with Enhanced Catalytic Performance for Wastewater Treatment, *ACS Omega*. 4 (2019) 1897–1906.
<https://doi.org/10.1021/acsomega.8b03615>.
- [67] A. Holzmeister, M. Rudisile, A. Greiner, J.H. Wendorff, Structurally and chemically heterogeneous nanofibrous nonwovens via electrospinning, *Eur. Polym. J.* 43 (2007) 4859–4867.
<https://doi.org/10.1016/j.eurpolymj.2007.09.014>.
- [68] D. Shou, L. Ye, J. Fan, Gas transport properties of electrospun polymer nanofibers, *Polymer*. 55 (2014) 3149–3155.
<https://doi.org/10.1016/j.polymer.2014.05.016>.
- [69] H. Wan, N. Wang, J. Yang, Y. Si, K. Chen, B. Ding, G. Sun, M. El-Newehy, S.S. Al-Deyab, J. Yu, Hierarchically structured polysulfone/titania fibrous membranes with enhanced air filtration performance, *J. Colloid Interface Sci.* 417 (2014) 18–26. <https://doi.org/10.1016/j.jcis.2013.11.009>.
- [70] A.C.. Neiva, L. Goldstein, A procedure for calculating pressure drop during the build-up of dust filter cakes, *Chem. Eng. Process. Process Intensif.* 42 (2003) 495–501. [https://doi.org/10.1016/S0255-2701\(02\)00066-1](https://doi.org/10.1016/S0255-2701(02)00066-1).
- [71] C. Kanaoka, H. Emi, Y. Otani, T. Iiyama, Effect of Charging State of Particles on Electret Filtration, *Aerosol Sci. Technol.* 7 (1987) 1–13.
<https://doi.org/10.1080/02786828708959142>.
- [72] D.C. Walsh, Recent advances in the understanding of fibrous filter behaviour under solid particle load, *Filtr. Sep.* 33 (1996) 501–506.

- [https://doi.org/10.1016/S0015-1882\(97\)84316-9](https://doi.org/10.1016/S0015-1882(97)84316-9).
- [73] G.E.R. Lamb, P.A. Costanza, Influences of Fiber Geometry on the Performance of Nonwoven Air Filters, *Text. Res. J.* 49 (1979) 79–87. <https://doi.org/10.1177/004051757904900205>.
- [74] C. Liu, P.-C. Hsu, H.-W. Lee, M. Ye, G. Zheng, N. Liu, W. Li, Y. Cui, Transparent air filter for high-efficiency PM_{2.5} capture, *Nat. Commun.* 6 (2015) 6205. <https://doi.org/10.1038/ncomms7205>.
- [75] Z.-B. He, S.-L. Guo, Applications of Nuclear Track Membranes to Filtration of Medical Injections and Various Transfusions to Remove Solid Particles, *Phys. Procedia.* 80 (2015) 131–134. <https://doi.org/10.1016/j.phpro.2015.11.081>.
- [76] K. Pan, Y. Fan, T. Leng, J. Li, Z. Xin, J. Zhang, L. Hao, J. Gallop, K.S. Novoselov, Z. Hu, Sustainable production of highly conductive multilayer graphene ink for wireless connectivity and IoT applications, *Nat. Commun.* 9 (2018) 5197. <https://doi.org/10.1038/s41467-018-07632-w>.
- [77] J. Song, Z. Chen, Z. Liu, Y. Yi, O. Tsigkou, J. Li, Y. Li, Controllable release of vascular endothelial growth factor (VEGF) by wheel spinning alginate/ silk fibroin fibers for wound healing, *Mater. Des.* (2021) 110231. <https://doi.org/10.1016/j.matdes.2021.110231>.
- [78] T.A. Carleton, S.M. Hsiang, Social and economic impacts of climate, *Science* (80-.). 353 (2016) aad9837–aad9837. <https://doi.org/10.1126/science.aad9837>.
- [79] J. Lelieveld, K. Klingmüller, A. Pozzer, U. Pöschl, M. Fnais, A. Daiber, T. Münzel, Cardiovascular disease burden from ambient air pollution in Europe reassessed using novel hazard ratio functions, *Eur. Heart J.* 40 (2019) 1590–1596. <https://doi.org/10.1093/eurheartj/ehz135>.
- [80] X. Huang, T. Jiao, Q. Liu, L. Zhang, J. Zhou, B. Li, Q. Peng, Hierarchical electrospun nanofibers treated by solvent vapor annealing as air filtration mat for high-efficiency PM_{2.5} capture, *Sci. China Mater.* 62 (2019) 423–436. <https://doi.org/10.1007/s40843-018-9320-4>.
- [81] C. Wang, S. Sun, L. Zhang, J. Yin, T. Jiao, L. Zhang, Y. Xu, J. Zhou, Q. Peng, Facile preparation and catalytic performance characterization of AuNPs-loaded

- hierarchical electrospun composite fibers by solvent vapor annealing treatment, *Colloids Surf., A*. 561 (2019) 283–291.
<https://doi.org/10.1016/j.colsurfa.2018.11.002>.
- [82] M.M. Maestas, R.D. Brook, R.A. Ziemba, F. Li, R.C. Crane, Z.M. Klaver, R.L. Bard, C.A. Spino, S.D. Adar, M. Morishita, Reduction of personal PM_{2.5} exposure via indoor air filtration systems in Detroit: an intervention study, *J. Expo. Sci. Environ. Epidemiol.* 29 (2019) 484–490.
<https://doi.org/10.1038/s41370-018-0085-2>.
- [83] T. Schroth, New HEPA/ULPA filters for clean-room technology, *Filtr. Sep.* 33 (1996) 245–244. [https://doi.org/10.1016/S0015-1882\(97\)84285-1](https://doi.org/10.1016/S0015-1882(97)84285-1).
- [84] N. Wang, Z. Zhu, J. Sheng, S.S. Al-Deyab, J. Yu, B. Ding, Superamphiphobic nanofibrous membranes for effective filtration of fine particles, *J. Colloid Interface Sci.* 428 (2014) 41–48. <https://doi.org/10.1016/j.jcis.2014.04.026>.
- [85] R. Sahay, Electrospun Filters for Defense and Protective Applications, in: *Filter. Media by Electrospinning*, Springer International Publishing, Cham, 2018: pp. 69–83. https://doi.org/10.1007/978-3-319-78163-1_4.
- [86] D.Y. Choi, S.-H. Jung, D.K. Song, E.J. An, D. Park, T.-O. Kim, J.H. Jung, H.M. Lee, Al-Coated Conductive Fibrous Filter with Low Pressure Drop for Efficient Electrostatic Capture of Ultrafine Particulate Pollutants, *ACS Appl. Mater. Interfaces.* 9 (2017) 16495–16504.
<https://doi.org/10.1021/acsami.7b03047>.
- [87] P. Pan, B. Zhu, W. Kai, T. Dong, Y. Inoue, Effect of crystallization temperature on crystal modifications and crystallization kinetics of poly(L-lactide), *J. Appl. Polym. Sci.* 107 (2008) 54–62.
<https://doi.org/10.1002/app.27102>.
- [88] K.C.K. Cheng, M.A. Bedolla-Pantoja, Y.-K. Kim, J. V. Gregory, F. Xie, A. de France, C. Hussal, K. Sun, N.L. Abbott, J. Lahann, Templated nanofiber synthesis via chemical vapor polymerization into liquid crystalline films, *Science* (80-.). 362 (2018) 804–808. <https://doi.org/10.1126/science.aar8449>.
- [89] K. Sing, The use of nitrogen adsorption for the characterisation of porous

- materials, *Colloids Surf., A.* 187–188 (2001) 3–9.
[https://doi.org/10.1016/S0927-7757\(01\)00612-4](https://doi.org/10.1016/S0927-7757(01)00612-4).
- [90] J. Lin, Y. Shang, B. Ding, J. Yang, J. Yu, S.S. Al-Deyab, Nanoporous polystyrene fibers for oil spill cleanup, *Mar. Pollut. Bull.* 64 (2012) 347–352.
<https://doi.org/10.1016/j.marpolbul.2011.11.002>.
- [91] A. S. de León, A. del Campo, M. Fernández-García, J. Rodríguez-Hernández, A. Muñoz-Bonilla, Fabrication of Structured Porous Films by Breath Figures and Phase Separation Processes: Tuning the Chemistry and Morphology Inside the Pores Using Click Chemistry, *ACS Appl. Mater. Interfaces.* 5 (2013) 3943–3951. <https://doi.org/10.1021/am400679r>.
- [92] J. Liu, X. Zhang, H. Zhang, L. Zheng, C. Huang, H. Wu, R. Wang, X. Jin, Low resistance bicomponent spunbond materials for fresh air filtration with ultra-high dust holding capacity, *RSC Adv.* 7 (2017) 43879–43887.
<https://doi.org/10.1039/C7RA07694K>.
- [93] J. Wang, Z. Bai, K. Xiao, X. Gao, P. Yi, C. Dong, J. Wu, D. Wei, Influence of atmospheric particulates on initial corrosion behavior of printed circuit board in pollution environments, *Appl. Surf. Sci.* 467–468 (2019) 889–901.
<https://doi.org/10.1016/j.apsusc.2018.10.244>.
- [94] W.W. Chen, R.L. Gao, L.S. Liu, M.L. Zhu, W. Wang, Y.J. Wang, Z.S. Wu, H.J. Li, D.F. Gu, Y.J. Yang, Z. Zheng, L.X. Jiang, S.S. Hu, China cardiovascular diseases report 2015: a summary, *J. Geriatr. Cardiol.* 14 (2017) 1–10. <https://doi.org/10.11909/j.issn.1671-5411.2017.01.012>.
- [95] H. Strongman, S. Gadd, A. Matthews, K.E. Mansfield, S. Stanway, A.R. Lyon, I. Dos-Santos-Silva, L. Smeeth, K. Bhaskaran, Medium and long-term risks of specific cardiovascular diseases in survivors of 20 adult cancers: a population-based cohort study using multiple linked UK electronic health records databases, *Lancet.* 394 (2019) 1041–1054. [https://doi.org/10.1016/S0140-6736\(19\)31674-5](https://doi.org/10.1016/S0140-6736(19)31674-5).
- [96] J.J. Green, J.H. Elisseeff, Mimicking biological functionality with polymers for biomedical applications, *Nature.* 540 (2016) 386–394.

- <https://doi.org/10.1038/nature21005>.
- [97] S.R. Jang, J.I. Kim, C.H. Park, C.S. Kim, Development of Y-shaped small diameter artificial blood vessel with controlled topography via a modified electrospinning method, *Mater. Lett.* 264 (2020) 127113.
<https://doi.org/10.1016/j.matlet.2019.127113>.
- [98] P. Wu, N. Nakamura, H. Morita, K. Nam, T. Fujisato, T. Kimura, A. Kishida, A hybrid small-diameter tube fabricated from decellularized aortic intima-media and electrospun fiber for artificial small-diameter blood vessel, *J. Biomed. Mater. Res. Part A.* 107 (2019) 1064–1070.
<https://doi.org/10.1002/jbm.a.36631>.
- [99] Q. Yao, J.G.L. Cosme, T. Xu, J.M. Miszuk, P.H.S. Picciani, H. Fong, H. Sun, Three dimensional electrospun PCL/PLA blend nanofibrous scaffolds with significantly improved stem cells osteogenic differentiation and cranial bone formation, *Biomaterials.* 115 (2017) 115–127.
<https://doi.org/10.1016/j.biomaterials.2016.11.018>.
- [100] L. Gui, B.C. Dash, J. Luo, L. Qin, L. Zhao, K. Yamamoto, T. Hashimoto, H. Wu, A. Dardik, G. Tellides, L.E. Niklason, Y. Qyang, Implantable tissue-engineered blood vessels from human induced pluripotent stem cells, *Biomaterials.* 102 (2016) 120–129.
<https://doi.org/10.1016/j.biomaterials.2016.06.010>.
- [101] N. Noor, A. Shapira, R. Edri, I. Gal, L. Wertheim, T. Dvir, 3D Printing of Personalized Thick and Perfusable Cardiac Patches and Hearts, *Adv. Sci.* 6 (2019) 1900344. <https://doi.org/10.1002/advs.201900344>.
- [102] H.H.G. Song, R.T. Rumma, C.K. Ozaki, E.R. Edelman, C.S. Chen, Vascular Tissue Engineering: Progress, Challenges, and Clinical Promise, *Cell Stem Cell.* 22 (2018) 340–354. <https://doi.org/10.1016/j.stem.2018.02.009>.
- [103] D.K. Patel, S.D. Dutta, J. Hexiu, K. Ganguly, K.-T. Lim, Bioactive electrospun nanocomposite scaffolds of poly(lactic acid)/cellulose nanocrystals for bone tissue engineering, *Int. J. Biol. Macromol.* 162 (2020) 1429–1441.
<https://doi.org/10.1016/j.ijbiomac.2020.07.246>.

- [104] L.E. Niklason, J.H. Lawson, Bioengineered human blood vessels, *Science* (80-.). 370 (2020) eaaw8682. <https://doi.org/10.1126/science.aaw8682>.
- [105] A. J. Melchiorri, N. Hibino, T. Yi, Y. U. Lee, T. Sugiura, S. Tara, T. Shinoka, C. Breuer, J. P. Fisher, Contrasting Biofunctionalization Strategies for the Enhanced Endothelialization of Biodegradable Vascular Grafts, *Biomacromolecules*. 16 (2015) 437–446. <https://doi.org/10.1021/bm501853s>.
- [106] G. Kulkarni, P. Guha Ray, P.K. Byram, M. Kaushal, S. Dhara, S. Das, Tailorable hydrogel of gelatin with silk fibroin and its activation/crosslinking for enhanced proliferation of fibroblast cells, *Int. J. Biol. Macromol.* 164 (2020) 4073–4083. <https://doi.org/10.1016/j.ijbiomac.2020.09.016>.
- [107] A.E. Thurber, F.G. Omenetto, D.L. Kaplan, In vivo bioresponses to silk proteins, *Biomaterials*. 71 (2015) 145–157. <https://doi.org/10.1016/j.biomaterials.2015.08.039>.
- [108] A. Alessandrino, A. Chiarini, M. Biagiotti, I. Dal Prà, G.A. Bassani, V. Vincoli, P. Settembrini, P. Pierimarchi, G. Freddi, U. Armato, Three-Layered Silk Fibroin Tubular Scaffold for the Repair and Regeneration of Small Caliber Blood Vessels: From Design to in vivo Pilot Tests, *Front. Bioeng. Biotechnol.* 7 (2019). <https://doi.org/10.3389/fbioe.2019.00356>.
- [109] Y. Guo, J. Guan, H. Peng, X. Shu, L. Chen, H. Guo, Tightly adhered silk fibroin coatings on Ti6Al4V biomaterials for improved wettability and compatible mechanical properties, *Mater. Des.* 175 (2019) 107825. <https://doi.org/10.1016/j.matdes.2019.107825>.
- [110] C. Marcolin, L. Draghi, M.C. Tanzi, S. Faré, Electrospun silk fibroin–gelatin composite tubular matrices as scaffolds for small diameter blood vessel regeneration, *J. Mater. Sci. Mater. Med.* 28 (2017). <https://doi.org/10.1007/s10856-017-5884-9>.
- [111] T. Wu, J. Zhang, Y. Wang, D. Li, B. Sun, H. El-Hamshary, M. Yin, X. Mo, Fabrication and preliminary study of a biomimetic tri-layer tubular graft based on fibers and fiber yarns for vascular tissue engineering, *Mater. Sci. Eng. C*. 82 (2018) 121–129. <https://doi.org/10.1016/j.msec.2017.08.072>.

- [112] E. Joseph, A. Patil, S. Hirlekar, A. Shete, N. Parekh, A. Prabhune, A. Nisal, Glycomonoterpene-Functionalized Crack-Resistant Biocompatible Silk Fibroin Coatings for Biomedical Implants, *ACS Appl. Bio Mater.* 2 (2019) 675–684. <https://doi.org/10.1021/acsabm.8b00515>.
- [113] N. Awad, H. Niu, U. Ali, Y. Morsi, T. Lin, Electrospun Fibrous Scaffolds for Small-Diameter Blood Vessels: A Review, *Membranes (Basel)*. 8 (2018) 15. <https://doi.org/10.3390/membranes8010015>.
- [114] J. Li, Y. Chen, A.F.T. Mak, R.S. Tuan, L. Li, Y. Li, A one-step method to fabricate PLLA scaffolds with deposition of bioactive hydroxyapatite and collagen using ice-based microporogens, *Acta Biomater.* 6 (2010) 2013–2019. <https://doi.org/10.1016/j.actbio.2009.12.008>.
- [115] C. Ru, F. Wang, M. Pang, L. Sun, R. Chen, Y. Sun, Suspended, Shrinkage-Free, Electrospun PLGA Nanofibrous Scaffold for Skin Tissue Engineering, *ACS Appl. Mater. Interfaces*. 7 (2015) 10872–10877. <https://doi.org/10.1021/acsami.5b01953>.
- [116] F. Qiao, J. Zhang, J. Wang, B. Du, X. Huang, L. Pang, Z. Zhou, Silk fibroin-coated PLGA dimpled microspheres for retarded release of simvastatin, *Colloids Surf., B*. 158 (2017) 112–118. <https://doi.org/10.1016/j.colsurfb.2017.06.038>.
- [117] A. Sadeghianmaryan, S. Naghie, H. Alizadeh Sardroud, Z. Yazdanpanah, Y. Afzal Soltani, J. Sernaglia, X. Chen, Extrusion-based printing of chitosan scaffolds and their in vitro characterization for cartilage tissue engineering, *Int. J. Biol. Macromol.* 164 (2020) 3179–3192. <https://doi.org/10.1016/j.ijbiomac.2020.08.180>.
- [118] Z. Lu, W. Wang, J. Zhang, P. Bártolo, H. Gong, J. Li, Electrospun highly porous poly(L-lactic acid)-dopamine-SiO₂ fibrous membrane for bone regeneration, *Mater. Sci. Eng. C*. 117 (2020) 111359. <https://doi.org/10.1016/j.msec.2020.111359>.
- [119] C.M.B. Gonçalves, J.A.P. Coutinho, I.M. Marrucho, Optical Properties, *Poly(Lactic Acid)*. (2010) 97–112.

- <https://doi.org/10.1002/9780470649848.ch8>.
- [120] P. Monti, P. Taddei, G. Freddi, T. Asakura, M. Tsukada, Raman spectroscopic characterization of Bombyx mori silk fibroin: Raman spectrum of Silk I, J. Raman Spectrosc. 32 (2001) 103–107. <https://doi.org/10.1002/jrs.675>.
 - [121] X. Jiang, Y. Luo, X. Tian, D. Huang, N. Reddy, Y. Yang, S. Abbott, L. Fambri, C. Migliaresi, G. Perego, G.D. Cella, Chemical Structure of Poly(Lactic Acid), Poly(Lactic Acid). (2010) 67–82. <https://doi.org/10.1002/9780470649848.ch6>.
 - [122] Z. Zhao, A. Chen, Y. Li, J. Hu, X. Liu, J. Li, Y. Zhang, G. Li, Z. Zheng, Fabrication of silk fibroin nanoparticles for controlled drug delivery, J. Nanoparticle Res. 14 (2012) 736. <https://doi.org/10.1007/s11051-012-0736-5>.
 - [123] F.M. Liao, X.T. Gao, X.S. Hu, S.L. Xie, J. Zhou, A general and efficient Lewis acid catalysed Mukaiyama-aldol reaction of difluoroenoxysilanes and ketones, Sci. Bull. 62 (2017) 1504–1509. <https://doi.org/10.1016/j.scib.2017.10.016>.
 - [124] S.K. Norouzi, A. Shamloo, Bilayered heparinized vascular graft fabricated by combining electrospinning and freeze drying methods, Mater. Sci. Eng. C. 94 (2019) 1067–1076. <https://doi.org/10.1016/j.msec.2018.10.016>.
 - [125] M.F. Leong, K.S. Chian, P.S. Mhaisalkar, W.F. Ong, B.D. Ratner, Effect of electrospun poly(D,L-lactide) fibrous scaffold with nanoporous surface on attachment of porcine esophageal epithelial cells and protein adsorption, J. Biomed. Mater. Res. Part A. 89A (2009) 1040–1048. <https://doi.org/10.1002/jbm.a.32061>.
 - [126] Y. Li, S. Wang, Y. Dong, P. Mu, Y. Yang, X. Liu, C. Lin, Q. Huang, Effect of size and crystalline phase of TiO₂ nanotubes on cell behaviors: A high throughput study using gradient TiO₂ nanotubes, Bioact. Mater. 5 (2020) 1062–1070. <https://doi.org/10.1016/j.bioactmat.2020.07.005>.
 - [127] F. Yang, C.Y. Xu, M. Kotaki, S. Wang, S. Ramakrishna, Characterization of neural stem cells on electrospun poly(L-lactic acid) nanofibrous scaffold, J. Biomater. Sci. Polym. Ed. 15 (2004) 1483–1497. <https://doi.org/10.1163/1568562042459733>.

List of Publications

First author publications

- 1) **Song, J.***, Zhang, B.*, Lu, Z., Xin, Z., Liu, T., Wei, W., Zia, Q., Pan, K., Gong, R.H., Bian, L. and Li, Y., 2019. Hierarchical porous poly (l-lactic acid) nanofibrous membrane for ultrafine particulate aerosol filtration. *ACS Applied Materials & Interfaces*, 11(49), pp.46261-46268.
- 2) **Song, J.**, Chen, Z., Murillo, L.L., Tang, D., Meng, C., Zhong, X., Wang, T. and Li, J., 2021. Hierarchical porous silk fibroin/poly (L-lactic acid) fibrous membranes towards vascular scaffolds. *International Journal of Biological Macromolecules*, 166, pp.1111-1120.
- 3) Chen, Z.*, **Song, J.***, Xia, Y., Jiang, Y., Murillo, L.L., Tsigkou, O., Wang, T. and Li, Y., 2021. High strength and strain alginate fibers by a novel wheel spinning technique for knitting stretchable and biocompatible wound-care materials. *Materials Science and Engineering: C*, 127, p.112204.
- 4) **Song, J.***, Chen, Z.*, Liu, Z., Yi, Y., Tsigkou, O., Li, J. and Li, Y., 2021. Controllable release of vascular endothelial growth factor (VEGF) by wheel spinning alginate/silk fibroin fibers for wound healing. *Materials & Design*, 212, p.110231.
- 5) **Song, J.**, Zhao, Q., Meng, C., Meng, J., Chen, Z. and Li, J., 2021. Hierarchical Porous Recycled PET Nanofibers for High-Efficiency Aerosols and Virus Capturing. *ACS Applied Materials & Interfaces*, 13(41), pp.49380-49389.
- 6) **Song, J.**, Wang, X.Q. and Li, J.S., 2018, July. Preparation of the silk fibroin 3D scaffolds with large pore sizes and high interconnectivity. In *11th Textile Bioengineering and Informatics Symposium*.

Co-author publications

- 1) Yang, X., Liu, X. and **Song, J.**, 2019. A study on technology competition of graphene biomedical technology based on patent analysis. *Applied sciences*, 9(13),

p.2613.

- 2) Lu, Z., **Song, J.**, Pan, K., Meng, J., Xin, Z., Liu, Y., Zhao, Z., Gong, R.H. and Li, J., 2019. EcoFlex sponge with ultrahigh oil absorption capacity. *ACS Applied Materials & Interfaces*, 11(22), pp.20037-20044.
- 3) Zhu, J., Tang, D., Lu, Z., Xin, Z., **Song, J.**, Meng, J., Lu, J.R., Li, Z. and Li, J., 2020. Ultrafast bone-like apatite formation on highly porous poly (l-lactic acid)-hydroxyapatite fibres. *Materials Science and Engineering: C*, 116, p.111168.
- 4) Zia, Q., Tabassum, M., Lu, Z., Khawar, M.T., **Song, J.**, Gong, H., Meng, J., Li, Z. and Li, J., 2020. Porous poly (L-lactic acid)/chitosan nanofibres for copper ion adsorption. *Carbohydrate polymers*, 227, p.115343.
- 5) Lu, Z., Zia, Q., Meng, J., Liu, T., **Song, J.** and Li, J., 2020. Hierarchical porous poly (l-lactic acid)/SiO₂ nanoparticles fibrous membranes for oil/water separation. *Journal of Materials Science*, 55(34), pp.16096-16110.
- 6) Pan, K., Leng, T., **Song, J.**, Ji, C., Zhang, J., Li, J., Novoselov, K.S. and Hu, Z., 2020. Controlled reduction of graphene oxide laminate and its applications for ultra-wideband microwave absorption. *Carbon*, 160, pp.307-316.

ORCID: <https://orcid.org/0000-0002-7689-1722>

The supporting information for deepen understanding and experimental repetition is available at https://1drv.ms/u/s!ArwcS-4UL1D_5EERIO2ITcuNbXng?e=s098cL, (passcode: EGCC).